MECHANICAL SIGNALS FOR COMPENSATORY LUNG GROWTH ASSESSED

BY HIGH RESOLUTION COMPUTED TOMOGRAPHY

APPROVED BY SUPERVISORY COMMITTEE

Connie Hsia, M.D.

Herbert Hagler, Ph.D.

Robert Johnson Jr., M.D.

Lynn Peterson, Ph.D.

Karel Zuzak, Ph.D.

ACKNOWLEDGMENTS

"The successful completion of any task would be incomplete without mentioning the people who made it possible and whose constant guidance and encouragement secured me this success"

First and foremost, I would like to express my sincere appreciation and gratitude to my mentor, Dr. Connie C.W. Hsia for her constant help and support since the first day I joined as a student research assistant. She is, in my opinion, a successful physician, clinical leader, and research scientist, and will always be a great source of inspiration. This dissertation work could not have been possible without her guidance, patience and motivation.

I would like to thank Dr. Robert L Johnson, Jr for his kind assistance and helpful discussions. I would like to thank Dr. Peter Antich, chair of the Bioengineering program at UT Southwestern for giving me an opportunity to pursue my dream of becoming a scientist at such a great institution. He has continuously provided support and made my experience at UT Southwestern memorable.

I would like to thank Dr. Lynn Peterson, Dr. Karel Zuzak and Dr. Herbert K Hagler for serving on my dissertation committee and giving me guidance, support and valuable suggestions to improve my work. Apart from the committee members, I would like to thank Dr. Cuneyt Yilmaz for his help, advice and guidance throughout this whole work. I would like to thank D.Merrill Dane for his invaluable help in answering my questions on CT principles and assistance with the CT scans.

I would like to thank Dennis Bellotto. He helped me significantly in the early days by showing me how to use the microscope and in helping me understand the basic principles of microscopy and histology. I will enjoy his friendship for the rest of my life. I would also like to thank the administrative personnel Ms. Jeanne-Marie Quevedo (Pulmonary Research) and Mrs. Kay Emerson (Bioengineering program). It was a privilege to have met people who took interest in my well being.

I would like to thank Daryn Clyburn, Richard Hogg, Deborah Hogg, Myresa Hurst, Jennifer Fehmel, Corie Thorson and Miguel Ortiz for technical assistance with the animals and the staff of the Animal Resources Center for veterinary assistance. I would like to extend my sincerest gratitude to Cynthia Proper, Melanie Bishop, Derek Lowe, Tom Ridgeway and Greg Horton for their technical assistance with CT scan at the Aston center. I would like to thank Dr. Roderick McColl for his assistance with data transfer and Dr. Gary Arbique for his help with CT scanner calibration.

I would also like to thank all the laboratory members both past and present, David Foster, Daniel Zhang, William Chance, Delories Reaves, Mustafa Shinta, Anagha Phansalkar, Prasanna Murugesan, and Paul McDonough who helped me solve problems and keep up my spirits.

Above all, I would like to express my heartfelt gratitude to **GOD**, the **ALMIGHTY** and my father who have guided me in every step of my way and brought me thus far. Most importantly, I would like to thank my dear husband, Ilan Balasubramanian for his endless love and encouragement. I could never have finished

this work without his consistent support and sacrifices in the previous five years. To him I dedicate this dissertation.

MECHANICAL SIGNALS FOR COMPENSATORY LUNG GROWTH ASSESSED BY HIGH RESOLUTION COMPUTED TOMOGRAPHY

by

PRIYA RAVIKUMAR

DISSERTATION

Presented to the Faculty of the Graduate School of Biomedical Sciences

The University of Texas Southwestern Medical Center at Dallas

In Partial Fulfillment of the Requirements

For the Degree of

DOCTOR OF PHILOSOPHY

The University of Texas Southwestern Medical Center at Dallas

Dallas, Texas

July, 2008

MECHANICAL SIGNALS FOR COMPENSATORY LUNG GROWTH ASSESSED BY HIGH RESOLUTION COMPUTED TOMOGRAPHY

Publication No._____

Priya Ravikumar, Ph.D.

The University of Texas Southwestern Medical Center at Dallas 2008

Supervising Professor: Connie C.W. Hsia, M.D.

This dissertation involves the use of high resolution computed tomography (HRCT) to understand the role of intra-thoracic mechanical force and its distribution in regenerative growth in dogs i.e. to quantify lobar lung volumes and density gradients in normal and post-pneumonectomy (following lung resection) lungs. HRCT was used to quantitatively assess regional distribution of lung volume and density gradients among lobes of the lung in order to follow the expansion of remaining lobes following lung resection with a high degree of anatomical precision, and to determine the relationships between lung expansion and alveolar tissue growth.

I also extended this work by relating regional lung expansion and growth assessed by radiology to regional alveolar tissue growth assessed by detailed quantitative histology under light and electron microscopy. This study illustrates for the first time a powerful and novel use of *in vivo* imaging to quantify regional lung distortion and changes in local volume, lung compliance as well as soft tissue density. These changes can be followed non-invasively and serially in a wide range of clinical and investigational applications, such as a) assessing the extent and progression of regional heterogeneity in lung disease or injury; b) assessing local response to treatment or surgical intervention; or c) assessing normal or abnormal patterns of lung growth.

TABLE OF CONTENTS

Signature Page i

Acknowledgements ii

Title Page …..... v

Copyright vi

Abstract vii

Table of Contents ix

Prior Publications xiii

List of Figures xvi

List of Tables xviii

List of Abbreviations xix

Chapter 1 Overview 1

1.1 Introduction 1

1.1.1 Mechanical Signals of Postnatal and Compensatory Lung Growth 1

1.1.2 Canine Model 2

1.1.3 Lung Imaging Using High Resolution Computed Tomography 2

1.1.4 Significance of Research 3

1.1.5 Hypothesis and Specific Aims 4

1.2 Organization 6

Chapter 2 Background and Significance 7

2.1 Anatomy 7

2.1.1 Anatomy of thoracic cavity 9

2.2 Pulmonary Imaging Modalities 10

2.2.1 Use of HRCT to Study Pulmonary Anatomy and Physiology 12
2.3 Mechanical Signals and Mechanisms of Lung Growth 13
2.3.1 Recruitment of Microvascular Reserves 17
2.3.2 Growth of New Alveolar Capillary Tissue 17
2.3.3 Remodeling of the Remaining Alveolar-Capillary Network 18
Chapter 3 Methods and Materials 20
3.1 Introduction 20
3.2 Animals 20
3.3 Pnemonectomy 21
3.4 CT Scanner Calibration 21
3.4.1 CTP401 – Slice Geometry and Sensitometry Module 23
3.4.1.1 Scan Slice Geometry (Slice width) 24
3.4.1.2 Scan Incrementation 24
3.4.1.3 Spatial Linearity of Pixel Size Verification 26
3.4.1.4 Sensitometry (CT Number Linearity) 26
3.4.2 CTP486 – Uniformity Module 28
3.5 High Resolution CT Image Acquisition 30
3.6 Analysis of CT Images 31
3.7 Terminal Procedure 34
3.8 Lung Volume Measurement 35
3.9 Morphometric Analysis 35
Chapter 4 Regional Lung Growth Following Left and Right Pnemonectomy 42
4.1 Introduction 42
4.2 Methods and Materials 43
4.2.1 Experimental Groups 43
4.2.2 Statistical Analysis 43

4.3 Results 44
4.3.1 Lobar Geometry After Right or Left PNX 44
4.3.2 Lobar Volumes After Right PNX 47
4.3.3 Lobar Volumes After Left PNX 50
4.3.4 Changes in Overall Lung Volumes 53
4.4 Discussion 53
4.4.1 Summary of Findings 53
4.4.2 Regional Post-PNX Compensatory Response 54
4.5 Conclusion 56
Chapter 5 Effect of Non-Uniform Post-PNX Signals on Postnatal Lung Growth 57
5.1 Introduction 57
5.2 Methods and Materials 59
5.2.1 Experimental Groups 59
5.2.2 Statistical Analysis 59
5.3 Results 60
5.4 Discussion 70
5.4.1 Normal Lung Development 70
5.4.2 Post-PNX Compensatory Response 71
5.4.3 Conclusion 73
Chapter 6 Correlation of lung growth assessed by computed tomography to that of Morphometry 75
6.1 Introduction 75
6.2 Results 76
6.3 Discussion 82
6.3.1 Summary of Findings 82
6.3.2 Critique of the Methods 82

6.3.3 Limitations of Morphometric Analysis 88
6.3.4 Conclusion 89
Chapter 7 Summary and Future Directions 90
7.1 Summary 90
7.2 Future Directions 91
REFERENCES 93
VITAE 102

PRIOR PUBLICATIONS

THESES

- **Ravikumar P.,** "Lung diffusing capacity measured by a rebreathing technique in guinea pigs raised at high altitude", Master of Science Thesis, Department of Biomedical Engineering, The University of Texas at Arlington, TX, August 2003.
- **Ravikumar P.,** "The design and implementation of the pulse rate monitor", Bachelor of Engineering Thesis, Department of Electronics and Instrumentation Engineering, The University of Madras, India, July 2001.

JOURNAL ARTICLES

- **Ravikumar P.**, Yilmaz C., Dane D.M., Johnson. R.L. Jr., Estrera A.S., and Hsia C.C.W., "Regional lung growth following pneumonectomy assessed by computerized tomography", *J. Appl. Physiol.* 97:1567-1574; 2004.
- Yilmaz C., Hogg D.C., **Ravikumar P.,** and Hsia C.C.W., "Ventilatory acclimatization in awake guinea pigs raised at high altitude", *J. Respiratory Physiology & Neurobiology.* 145:235-242; 2005
- **Ravikumar P.**, Yilmaz C., Dane D.M., Johnson R.L. Jr., Estrera A.S. and Hsia C.C.W., "Developmental signals do not further accentuate nonuniform postpneumonectomy compensatory lung growth", *J. Appl. Physiol.* 102(3):1170-7; 2007.
- Zhang Q., Bellotto D.J.**, Ravikumar P.**, Moe O.W., Hogg R.T., Hogg D.C., Estrera A.S., Johnson R.L. Jr., Hsia C.C.W., "Postpneumonectomy lung

expansion elicits hypoxia-inducible factor-1alpha signaling**",** *Am. J. Physiol. Lung Cell Mol. Physiol.* 293(2):L497-504; 2007.

PEER-REVIEWED CONFERENCE ABSTRACTS

- **Ravikumar P.**, Bellotto D.J., Johnson, R.L. Jr. and Hsia C.C.W., "Non-uniform compensatory alveolar growth following extensive lung resection", *Am. J. Resp. Crit. Care Med.,* 177:A316, 2008.
- **Ravikumar P.**, Bellotto D.J., Foster D.J. and Hsia C.C.W., "Adaptation of lung structure to high altitude residence is partially reversed following return to low altitude", *Am. J. Resp. Crit. Care Med.,* 177:A545, 2008.
- **Ravikumar P.,** Bellotto D.J., Johnson R.L. Jr. and Hsia C.C.W., "Permanent alveolar remodeling induced by high altitude residence during maturation", *FASEB J.,* 21(6):A949, 2007
- **Ravikumar P.,** Yilmaz C., Dane D.M., Hsia C.C.W., Hurst M.D., Fehmel J.L., Thorson C.L. and Johnson R.L. Jr., "Delayed Imposition of Mechanical Lung Strain Improves Adaptive Response Following Pneumonectomy", *Proc. Am. Thorac. Soc.,* 3:A873, 2006.
- **Ravikumar P.,** Yilmaz C., Dane D.M., and Hsia C.C.W., "Non-Uniform Lobar Expansion Following Extensive Lung Resection", *Proc. Am. Thorac. Soc.,* 2:A835, 2005.
- **Ravikumar P.,** Yilmaz C., Dane D.M., and Hsia C.C.W., "Non- Uniform Lobar expansion following left pneumonectomy", *Am. J. Resp. Crit. Care Med.,* 169(7):A496, 2004.

- Yilmaz C., **Ravikumar P.,** and Hsia C.C.W., "Lung diffusing capacity in high altitude raised guinea pigs following acclimatization to low altitude", *Am. J. Resp. Crit. Care Med.,* 169(7):A199, 2004
- **Ravikumar P.**, Yilmaz C., Dane D.M., Hogg R.T., Hogg D.C., and Hsia C.C.W., "Lobar lung growth following pneumonectomy assessed by CT Scan", *Am. J. Resp. Crit. Care Med.,* 167(7):A847, 2003.
- Yilmaz C., **Ravikumar P.,** Hogg D.C., and Hsia C.C.W., "Increased Lung Diffusing Capacity Measured by Rebreathing Technique in Guinea Pigs Raised at High Altitude", *Am. J. Resp. Crit. Care Med.,* 167(7):A706, 2003.
- Yilmaz C., **Ravikumar P.,** and Hsia C.C.W., "Ventilatory response to hypoxia in guinea pigs after chronic exposure to high altitude", *Am. J. Resp. Crit. Care Med.,* 165(8):A133, 2002.

LIST OF FIGURES

Figure		Page
2.1	Structure of the human airway tree	8
2.2	Terminal portion of the respiratory tree	9
2.3	Lobar anatomy of dog lung	10
2.4	A thin slice spiral CT image on a transverse view	13
2.5	Mechanical interaction between the thorax and lung	14
2.6	Thoracic CT scan of a foxhound after right pneumonectomy	15
3.1	Catphan 500 model phantom	22
3.2	Scan image from the CTP 401 module.	23
3.3	Measurement of slice width with the 23° wire ramps.	25
3.4	Relationship between the nominal CT number of the sensitometric targets and the absolute difference between actual and measured values.	28
3.5	Scan image from the CTP 486 module	29
3.6	CT image from a dog after right pneumonectomy	34
3.7	Schematic representation of the sampling protocol	37
3.8	Stratified quantification of lung structure	40
4.1	Thoracic CT scan after left and right pneumonectomy	45
4.2	Three dimensional lobar reconstruction from Sham groups and after left and right pneumonectomy in four anatomic views	46
4.3	Relative change in air and tissue volume after right pneumonectomy	49
4.4	Relative change in air and tissue volume after left pneumonectomy	52
5.1	Three dimensional lobar reconstruction from pneumonectomy and Sham groups at 4 and 10 mo after surgery	61
5.2	Air and tissue volumes 4 and 10 mo after right pneumonectomy	65
5.3	Lobar tissue density 4 and 10 mo after right pneumonectomy	66

5.4 Relative change in air and tissue volumes 4 and 10 mo after right pneumonectomy 67

6.1 Correlation of lung volumes measured by CT scan and morphometry 76

6.2. Relative change in air and tissue volume after left pneumonectomy assessed by HRCT and morphometry 80

6.3 Relative change in air and tissue volume after right pneumonectomy assessed by HRCT and morphometry 82

LIST OF TABLES

Table		Page
3-1	Slice width measurements	25
3-2	Distance accuracy measurements	26
3-3	CT number linearity measurements	27
3-4	Uniformity and noise measurements	30
4-1	Lobar volumes in the normal left lung and following right pneumonectomy	48
4-2	Lobar volumes in the normal right lung and following left pneumonectomy	51
5-1	Lobar tissue and air volume in the normal left lung and after right Pneumonectomy before and after reaching somatic maturity	64
5-2	Relative post-pneumonectomy compensation assessed by HRCT before or after somatic maturity	69
6-1	Comparison of compensation after left pneumonectomy by HRCT and morphometry	79
6-2	Relative compensation after right pneumonectomy assessed by HRCT and morphometry	81

LIST OF ABBREVIATIONS

ANOVA	Analysis of Variance
CT	Computed Tomography
FRC	Functional Residual Capacity
HRCT	High Resolution Computed Tomography
HU	Hounsfield number
LLL	Left Lower (caudal) Lobe
LML	Left Middle Lobe
L-PNX	Left Pneumonectomy
LUL	Left Upper (cranial) Lobe
PNX	Pneumonectomy
RA	Retinoic acid
RCL	Right Cardiac Lobe
RLL	Right Lower (caudal) Lobe
RML	Right Middle Lobe
R-PNX	Right Pneumonectomy
RUL	Right Upper (cranial) lobe
TLC	Total Lung Capacity

Chapter 1 Overview

1.1 Introduction

The lung's internal structures were once considered non-malleable following the completion of alveolar development, and treatment for chronic parenchymal disease has focused primarily on preventing further tissue destruction. This approach is being revised in light of recent findings that illustrate the possibility of accelerating the rate of lung growth during and beyond the period of postnatal maturation. Extensive published data suggest that mechanical forces play a major role in the regulation of different aspects of lung growth and maturation.

1.1.1 Mechanical Signals of Postnatal and Compensatory Lung Growth

Mechanical forces imposed on lung tissue from a growing rib cage constitutes a major stimulus for postnatal lung growth and maturation (34). During maturation, recoil generated by an enlarging thorax exerts a negative intra-thoracic pressure that opposes lung elastic recoil. The resulting mechanical stress and strain trigger cell proliferation and lung tissue growth that continues until somatic maturity, when the bony epiphyses close and the ribcage and the lungs become fixed in size and shape. A highly robust model of lung growth induced by mechanical forces is that which occurs following surgical resection of one lung (pneumonectomy, PNX), a procedure that mimics the loss of functional lung units in chronic parenchymal disease, and a reproducible model for studying the extent and mechanisms of the adaptive response in the remaining lung. PNX

has been shown to initiate rapid compensatory growth of the remaining lung in mice, rats, rabbits, ferrets, and dogs (2, 5, 11, 28, 56, 59, 74, 75, and 90).

1.1.2 Canine Model

In small rodents the rib cage and lungs continue to grow throughout life. In contrast, in large mammals the bony epiphyses close upon reaching somatic maturity, thereby setting an upper limit to the dimensions of both the rib cage and the lungs at adulthood. Lung architecture and growth pattern are similar between dogs and humans (33); hence the dog is an appropriate animal model for mimicking the human response. The canine lungs are divided into seven distinct anatomic compartments called lobes. Though they are physically separated by the lobar fissures, the lung lobes are inter-dependent with regard to respiratory function. Therefore, it is important to consider inter-lobar differences as well as left vs. right asymmetry when studying the distribution of regional lung volumes, ventilation and expansion (10, 46, 47, 48, and 53), analyzing regional changes in lung strain (69 and 82), and measuring the variability of parenchymal expansion and deformation (52 and 80).

1.1.3 Lung Imaging Using High Resolution Computed Tomography

High-resolution computed tomography (HRCT) imaging, which can acquire high spatial and temporal resolution volumetric pulmonary images within a short breath hold period and provide detailed information regarding the pulmonary structures (79), has been widely used both for routine clinical applications as well as basic investigation of pulmonary structure-function relationships (30). Unlike the techniques that study aggregate structures or global functions, CT imaging can be used to study pulmonary

anatomy and physiology on a regional level, thereby providing the possibility to detect early pathologies, to follow disease development, and to monitor the response to treatment. However, despite its proven clinical importance, HRCT is plagued by certain shortcomings. For instance, HRCT uses a mathematical equation to partition total lung volume into air and tissue volume (since the CT attenuation value of the lung is directly proportional to the ratio of tissue and air). Though this equation has been widely used by other investigators (13, 29, 49) and by us (50, 87, 88 and 100), it still needs to be validated against the existing gold standard of lung tissue volume measurement i.e. quantitative histology to ensure that the CT derived measurements are physiologically relevant.

1.1.4 Significance of Research

My dissertation project will demonstrate the novel use of HRCT for the non-invasive assessment of normal and compensatory lung growth at the regional level. The significance of this research is two-fold. Firstly, this research will establish the feasibility of quantitative HRCT image analysis for studying the gas exchange region of the lung. Most evaluation of lung parenchyma by HRCT is qualitative. Lung volume and anatomical reference points can shift due to local tissue distortion, making it difficult to match the same areas on serial scans. My dissertation will identify the lung lobes via their natural boundaries, thereby permitting unambiguous quantitative comparison of the same lung regions over repeated scans and under different conditions. Lobar partition has not been done before, and this technique will substantially broaden the potential applications of HRCT to the lung.

Secondly, these studies will establish the practical application of HRCT as a non-invasive investigative tool for following the magnitude and distribution of lung growth. Conventional assessment of lung growth requires invasive or terminal procedures to obtain tissue for analysis. To define temporal evolution of growth requires comparison of different experimental cohorts at different ages. Using HRCT, *in vivo* lung growth can be tracked in the same subject, thereby facilitating longitudinal correlation of anatomy to function. This will be an important application to lung biology as well as pulmonary medicine.

1.1.5 Hypothesis and Specific Aims

In adult dogs the initiation of compensatory lung growth following PNX correlates with the expansion, and presumably the level of mechanical strain, experienced by the remaining lung, i.e., growth is initiated after resection of ~58% of total lung mass by right PNX but not after ~42% resection by left PNX (37 and 38); minimization of lung expansion blunts compensatory cellular and physiological responses (42, 44, and 100). At postmortem, we routinely observed uneven shape changes among the lobes that remain after PNX. Based on our preliminary findings that post-PNX compensatory responses are determined by the magnitude and distribution of mechanical strain, ***this dissertation aims to quantify in vivo changes in regional lung distortion, volume, and density of gas exchange tissue using high resolution computed tomography, and to correlate the results to detailed quantitative histology.***

Our hypotheses are:

1) Compensatory growth in the remaining lobes following PNX is non-uniform, owing to the relative rigidity and asymmetry of the heart and major mediastinal vessels and ligaments. Non-uniformity limits the overall adaptive response.

2) In actively growing animals, mechanical signals during normal lung development interact with those following PNX to exaggerate the non-uniformity of regional lung growth.

3) X-ray attenuation gradients obtained from HRCT may be used to follow regional lung growth *in vivo*.

We will characterize the magnitude and distribution of compensatory growth among lobes using HRCT in adult dogs after 42% and 58% lung resection. In separate animals, we will also access regional distribution of lung volume before and after somatic maturity. Lobar air and tissue volumes will be assessed from CT attenuation gradients. We will relate lobar growth and expansion to parenchymal growth measured by quantitative histology. These studies define mechanical signal-response relationships in an established model of strain-induced compensatory lung growth and this understanding should facilitate the design of strategies to enhance lung growth not just after PNX but also in other restrictive lung diseases.

1.2 Organization

Chapter 2 introduces some basic concepts of respiratory anatomy; pulmonary imaging modalities and the role of mechanical signals in normal and compensatory lung growth are discussed in detail.

Chapter 3 provides a detailed description of the methodology including those pertaining to lung resection surgeries, construction and implantation of prosthesis, CT scanner calibration, image acquisition and analysis, terminal procedures and morphometric analysis.

Chapter 4 describes how regional lung volume is assessed after left and right PNX using HRCT.

Chapter 5 delves into the assessment of regional distribution of lung volume before and after somatic maturity to determine the impact of superimposing developmental signals on post-PNX signals.

Chapter 6 probes to validate the regional lung volume measures by HRCT against quantitative histology to determine the utility of HRCT in following parenchyma growth in vivo.

Chapter 7 summarizes the work presented in the previous chapters with recommendations for future directions. References and vitae are included at the end of this document.

Chapter 2 Background and Significance

2.1 Anatomy

The respiratory system is comprised of the nose, nasal cavity, pharynx, larynx, trachea, bronchi and smaller passageways and respiratory muscles to bring air to the alveoli, the sites of gas exchange. The nasal cavity warms and moistens air and also removes foreign material. The pharynx serves as a passageway for both the respiratory and the digestive systems. The larynx guards the entrance to the trachea, vocalizes, and regulates the inflow and outflow of air. The trachea is a flexible, cartilaginous and membranous tube, extending from the cricoid cartilage of the larynx to its bifurcation dorsal to the cranial part of the base of the heart. The crest of the partition at the side where the trachea divides into the two principal bronchi is called the carina.

The bronchial tree begins at the bifurcation of the trachea with the formation of a right and a left main stem bronchus. Each main stem bronchus divides into secondary (lobar) bronchi. Within each lobe the lobar bronchi further divide into tertiary (segmental) bronchi. The segmental bronchi branch dichotomously into smaller bronchi through successive generation until the respiratory bronchioles are formed. On average the first 16 generations of human airways are conducting airways that do not participate in gas exchange. The last generation of conducting airway is termed a terminal bronchiole, which supplies an acinus. The human acinus consists of on average 3 generations of partially alveolated respiratory bronchioles followed by 2 to 3 generations of alveolar ducts that end in alveolar sacs where diffusive gas exchange takes place. As the front of inspired air moves distally down the airways, the pattern of oxygen transport

and mixing within this front changes from a combination of turbulent and laminar convection in the conducting airways to predominantly diffusive mixing as it moves into the acini and finally into the alveoli where alveolar capillary gas exchange occurs. Anatomy of the airway tree is shown in figures 2.1 and 2.2 below.

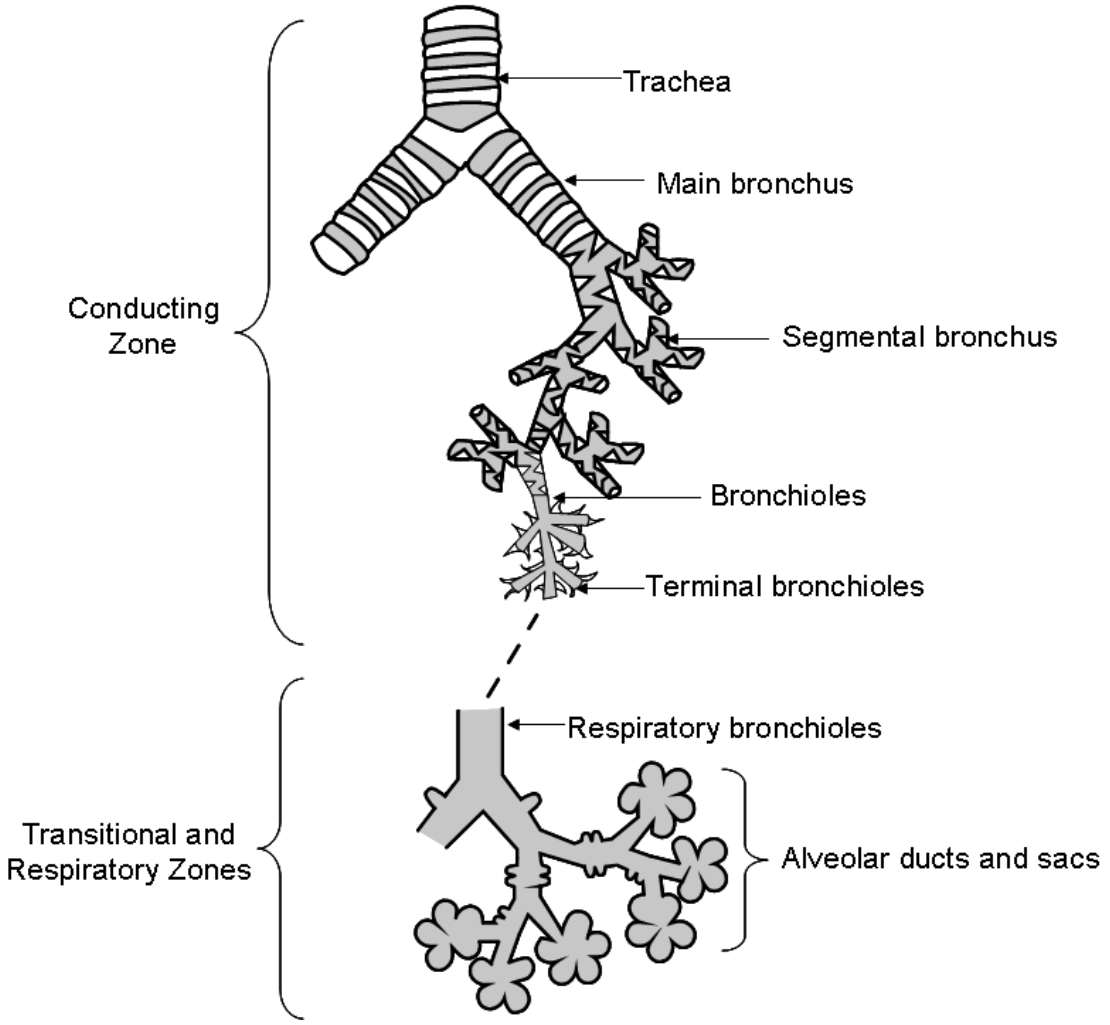

Figure 2.1 Structure of the human airway tree. On average the first 16 generations are conducting airways that do not participate in gas exchange. The last conducting airway is called a terminal bronchiole, which supplies an acinus. In the acinus there are 3 generations of partially alveolated respiratory bronchioles followed by alveolar ducts that end in alveolar sacs. [Adapted from (6)]

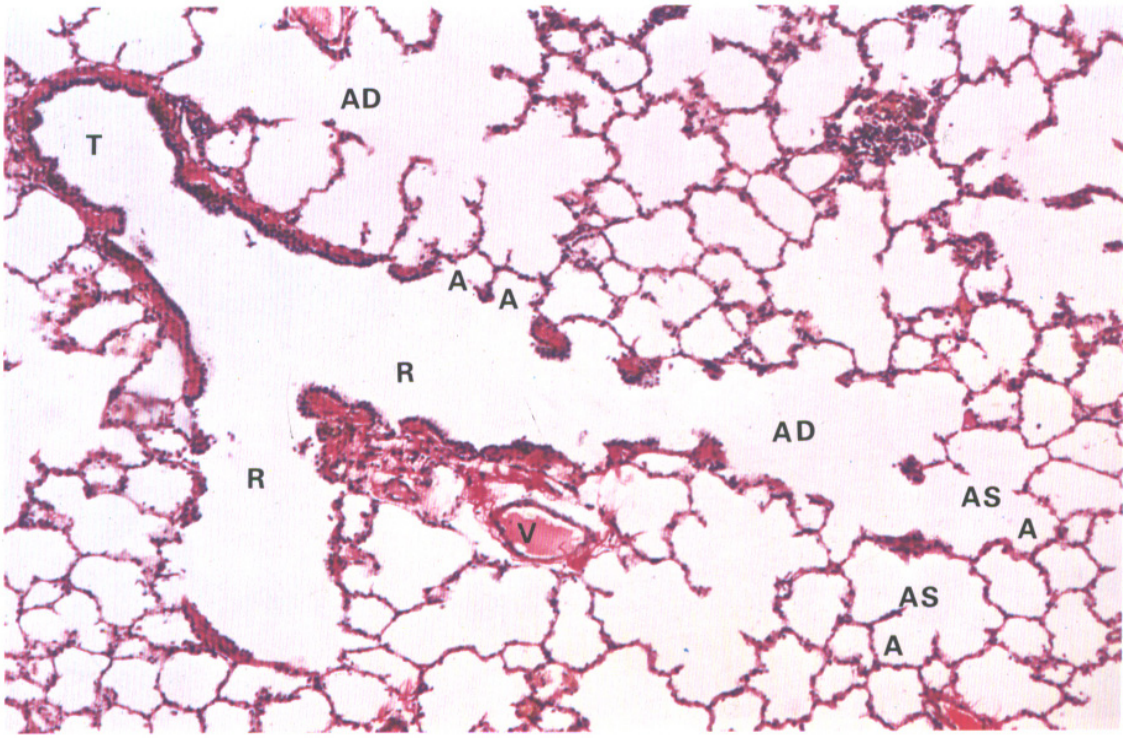

Figure 2.2 Terminal portion of the respiratory tree. *Terminal bronchioles* T are the smallest diameter passages of the conducting portion of the respiratory tree. Each terminal bronchiole divides to form short, thinner-walled branches called respiratory bronchioles R. Each respiratory bronchiole divides further into long, winding passages called *alveolar ducts* AD which open along their length into numerous *alveolar sacs* AS and *alveol*i A. Surrounding each alveolus is a rich network of pulmonary capillaries supplied by pulmonary *vessels* V. [Adapted from (6)]

2.1.1 Anatomy of the thoracic cavity

The thoracic cavity is bounded by the muscles and bones of the ribcage and diaphragm. The thoracic cavity contains the lungs, heart, great vessels, thymus gland, and lymph nodes. The mediastinum is the space between the right and left pleural sacs that is occupied by the thymus, heart, aorta, trachea, esophagus, the vagus nerves, and other nerves and vessels.

The lung takes up oxygen from the atmosphere and eliminates carbon dioxide from the blood. The dog lung is composed of 7 lobes. The left lung has three distinct

lobes, namely, the cranial (upper), middle and caudal (lower) lobes. The oblique fissure divides the left lung into two nearly equal parts, namely, the upper and middle and the lower lobe. The left upper lobe is separated from the middle lobe by the minor fissure. The right lung is divided into four lobes cranial (upper), middle, caudal (lower) and accessory (infra-cardiac) lobes. The right oblique fissure separates the upper and middle lobes from the cardiac and lower lobes. The upper lobe of the right lung is separated from the middle lobe by the curved horizontal fissure. The lower and cardiac lobes are separated by the deep fissure, illustrated in figure 2.3 (19 and 20).

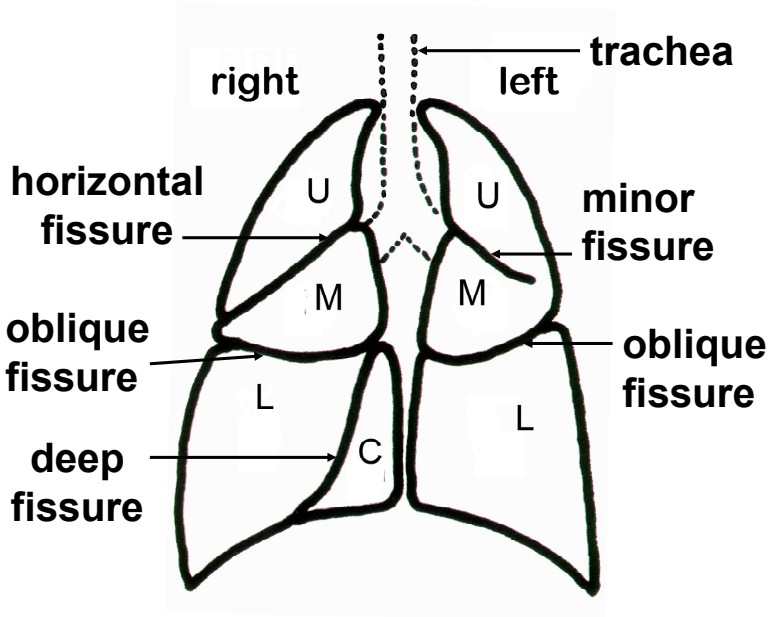

Figure 2.3 Lobar anatomy of dog lung. Position of inter lobar fissures are indicated.

2.2 Pulmonary Imaging Modalities

In a chest radiograph, an X-ray beam is directed through the thorax onto an X-ray detector to form a 2D projection image of 3D anatomy. As a beam of X-ray is incident upon a block of material, the X-ray intensity decreases because of the interaction of the

photons and the material. Assume that an X-ray beam has incident intensity I_0. When the beam passes through a homogenous material of thickness X, the intensity of the X-ray beam becomes

$$I = I_0 \exp(-\mu X) \qquad \text{Equation 2.1}$$

where μ is the linear attenuation coefficient. The value of μ depends on the density, atomic number, electron density of the material, and the energy of the applied X-ray photons. Thus, the attenuation coefficients can be used to characterize different materials. In the thorax, bone absorbs more X-ray energy than lung tissue, and lung tissue absorbs more X-rays than air. HRCT, introduced in the early 1970s, overcomes the overlapping and geometric ambiguity problems in chest radiography, and provides better contrast resolution for soft tissues. Projection images, in the case of the conventional radiograph, render the sum of all signal contributions along a ray from the X-ray tube to each picture element. In such a superposition image, only structures which exhibit very high differences in attenuation with respect to their surroundings can be recognized. On the other hand, HRCT images display the attenuation resulting from each volume element directly assigned to the respective single picture element. Contrast is determined locally by the composition of the tissues, while neighboring or superimposed structures have no or only very little influence and hence, small differences in the density or composition of tissues can therefore be rendered with sufficient contrast. In addition, HRCT provides a calibrated estimate of x-ray attenuation, which can be used for image-based quantification. By generating a series of 2D cross-sectional slices, HRCT can show the internal structure of a 3D object and provide the basis for quantitative image analysis. For each 2D cross-section in the CT data, multiple projections at different angles are

collected by the detectors and sent to a computer for image reconstruction. The multiple projections are mathematically reconstructed to give the attenuation distribution. Then, different tissue types on the cross-section can be characterized by the different attenuation coefficients. However, the attenuation coefficient μ is not very descriptive and is strongly dependent on the spectral energy used. A display of μ would make quantitative statements cumbersome; a direct comparison of images obtained on scanners with different voltages and filtration would be limited. Therefore the computed attenuation coefficient is displayed as a CT value relative to the attenuation of pure water (51). CT attenuation values are often referred to as CT numbers, specified in Hounsfield units (HU). For an arbitrary tissue T with attenuation coefficient μ_T *the* CT value is defined as

$$\text{CT value} = \frac{\mu_{\text{T}} - \mu_w}{\mu_{\text{w}}} \times 1000 HU \qquad \text{Equation 2.2}$$

where μ_w is the attenuation coefficient of pure water. The CT value is arbitrarily set at zero HU for water, and −1000 HU for air.

2.2.1 Using HRCT to Study Pulmonary Anatomy and Physiology

HRCT can yield detailed images of pulmonary anatomy with a high data acquisition speed. Figure 2.4 illustrates a thin-slice CT image of normal dog lungs. The lungs, lobar fissures, airways, and vessels can be clearly distinguished.

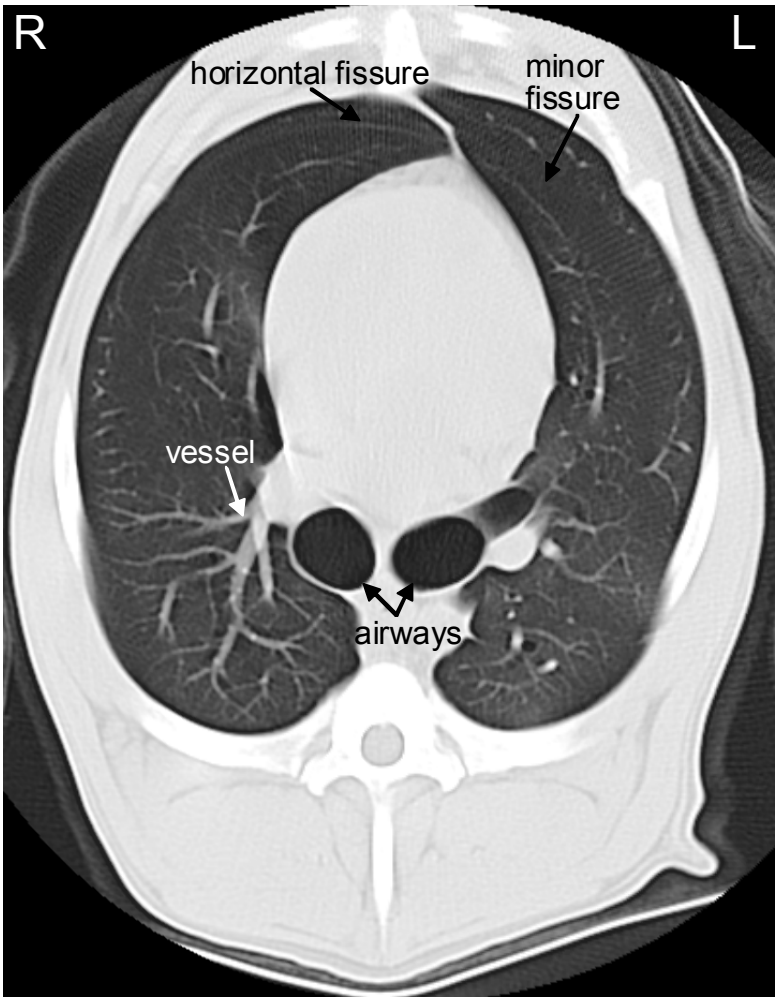

Figure 2.4 A thin slice spiral CT image on a transverse view

2.3 Mechanical Signals and Mechanisms of Lung Growth

Mechanical forces play an important role in modulating the growth and function of tissues and organs (92). Clinical and experimental observations suggest that mechanical forces are necessary for the growth and maturation of fetal and postnatal lung. For instance, *in vitro* studies have demonstrated that the proliferation and metabolic activity of fetal lung cells are stimulated by mechanical strain (103).

Mechanical stress imposed on lung tissue from a growing rib cage constitutes a major stimulus for postnatal lung growth and maturation (34). During somatic maturation, recoil generated by an enlarging thorax exerts a negative intra-thoracic pressure that opposes lung elastic recoil. The resulting mechanical stress and strain trigger cell proliferation and lung tissue growth which in turn alleviates the septal stress and strain, creating a negative feedback loop that continues until somatic maturity, when the bony epiphyses close and the ribcage attains its adult size and shape. From then on, mechanical signals diminish; tissue growth ceases and the lungs become fixed in size and shape (Figure 2.5)

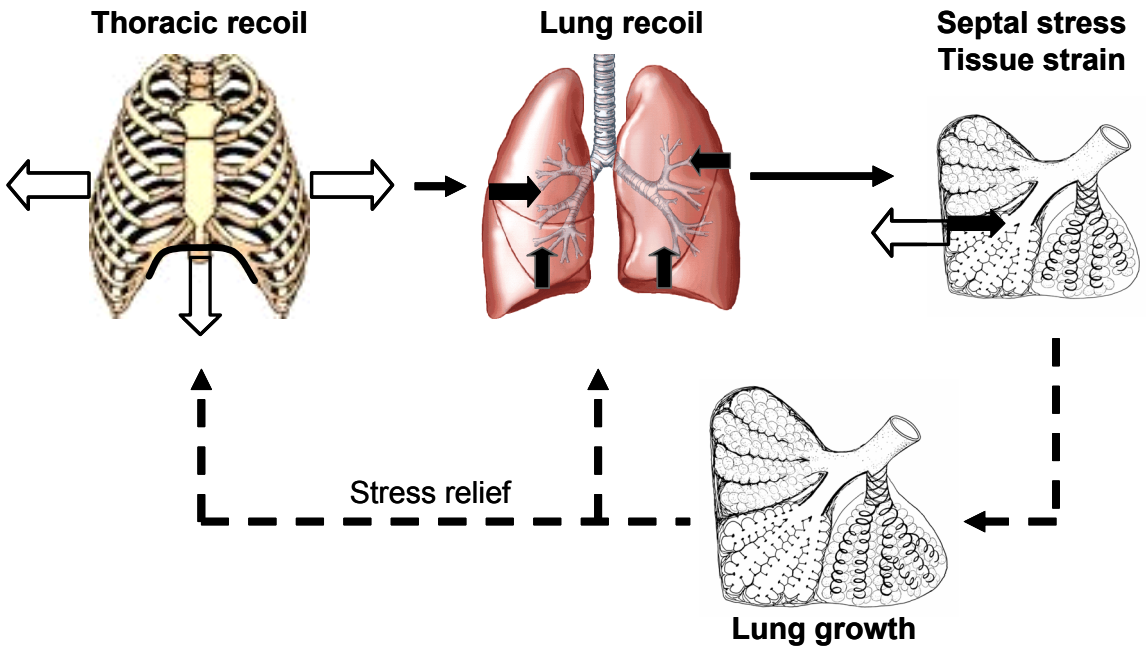

Figure 2.5 Mechanical interaction between the thorax and lung.
[Adapted by permission from Hsia et al. (34)]

When mechanical stress imposed on the growing lung tissue is compromised as in the case of congenital diaphragmatic hernia, pulmonary growth is severely impaired due to prolonged under-expansion of the lungs during fetal development (89). Diaphragmatic

hernia is often associated with lung hypoplasia (89), reduced alveolar surface area and reduced alveolar number as well as impaired development of pulmonary vascular bed (54) and deficiency of pulmonary surfactant production (91). Experimental tracheal ligation has been shown to accelerate fetal lung growth in response to an increase in intratracheal pressure caused by retention of fetal lung fluid, reversing some aspects of alveolar cellular and vascular hypoplasia associated with diaphragmatic hernia (1, 26, 32, and 63). When mechanical strain is accentuated during development, alveolar cellular growth is accelerated, as seen with sustained lung distension during perflurocarbon liquid ventilation in lambs (64).

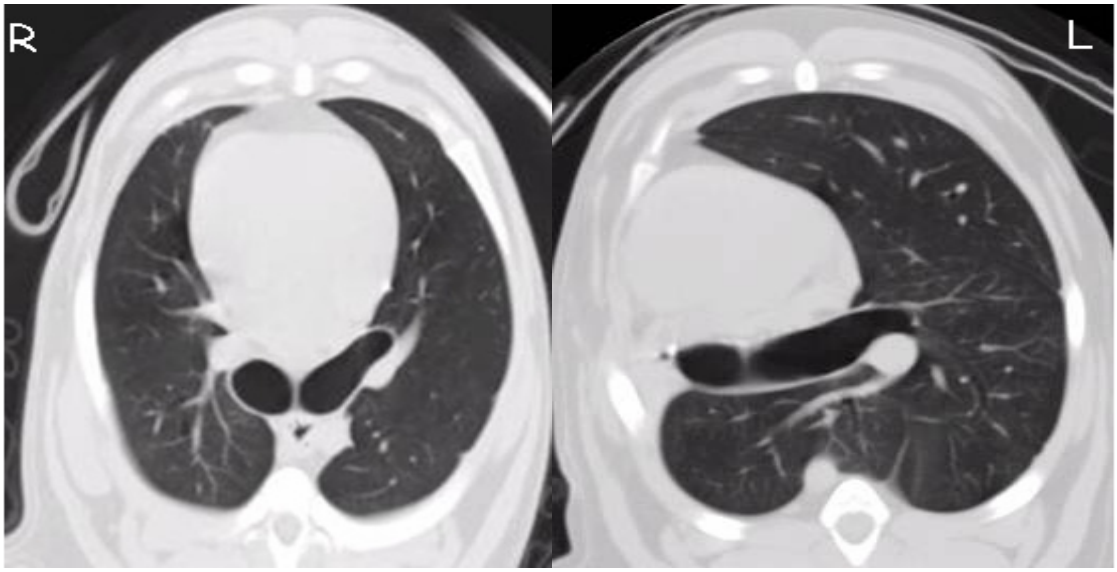

Figure 2.6 Thoracic CT scan of a foxhound showing mediastinal shift and enlargement of the remaining lung after right pneumonectomy (right) compared with controls (left).

After experimental resection of one lung or PNX, the chest wall closed and residual air absorbed, a negative intrathoracic pressure causes the remaining lung to expand, i.e. imparting three-dimensional strain. It has been shown that mechanical strain is a primary stimulus for post-PNX lung growth and remodeling (11, 76). PNX elicits a

number of anatomical changes within the thoracic cavity as illustrated in figure 2.6. Following PNX the remaining lung doubles its original volume and expands across the midline into the empty hemithorax. The entire cardiac output is directed into the remaining lung tissue and the mediastinal structures are shifted towards the vacated thoracic compartment. The ipsilateral rib cage and hemi-diaphragm are distorted.

The immediate increase in lung distension following PNX can be prevented by pleural plombage (replacement of the resected lung with a space occupying material). In our previous studies (42, 44 and 100), we demonstrated that minimizing lung strain after right PNX by a space-occupying inflatable silicone prosthesis is associated with blunted compensatory lung growth estimated by CT and morphometry as well as a lower diffusing capacity for CO and O_2 at rest and during exercise. Though unable to expand across the midline due to the presence of inflated prosthesis, the remaining left lower lobe still enlarged ~20%. The inflated prosthesis preferentially limited the expansion and growth of the remaining upper and middle lobes; but the lower lobe continued to expand by the caudal and outward displacement, respectively, of the ipsilateral hemidiaphragm and lower rib cage (100 and 77). These studies reinforce the fact the mechanical lung strain is a major signal for post-pneumonectomy compensation *in vivo* but minimizing lung strain diminishes but does not completely abolish post-PNX growth and expansion of the remaining lung. Other signals such as increased endothelial shear (stemming from increased perfusion), hypoxia, and non-specific responses to surgical stress, inflammation and wound healing might also play a role.

Post-pneumonectomy lung distention and increase in blood flow provide mechanical signals for compensation in the remaining lung through several mechanisms discussed below:

2.3.1 Recruitment of Microvascular Reserves

Normally a significant fraction of alveolar capillary surfaces and capillaries are not utilized at rest but they could be recruited with increased blood flow and ventilation as seen during peak exercise or with loss of lung units. At rest, only half the total numbers of alveoli and capillaries participate in gas exchange, and capillary erythrocytes are unevenly distributed; many capillaries particularly at the apex are perfused only with plasma but not erythrocyte (55). After PNX, if ventilation and cardiac output remain the same, airflow and perfusion through the remaining lung increase by a factor of one divided by the fraction of lung remaining, leading to recruitment of existing alveolar-capillary reserves in the remaining lung via unfolding of epithelial surfaces, opening and distension of alveolar microvessels, and redistribution of capillary erythrocyte flow (67), all of which increase the effective surfaces for gas exchange without any intrinsic change in alveolar structure.

2.3.2 Growth of New Alveolar Capillary Tissue

Several mammalian species are known to exhibit the capacity for regenerative growth of the lung. This ability appears to correlate with the growth characteristics of the species. In rodents where body growth continues throughout life, the ability to completely replace the mass of lung removed by partial PNX is retained (4, 5, 7, 21, 75, and 82). In larger mammals such as the dog, the rib cage reaches maximum dimensions at maturity

and hence the lung also stops growing. In adult animals where the regenerative potential is limited, the sources of post-PNX compensation vary depending upon the magnitude and uniformity of mechanical strain imposed on the remaining lung units (86). Compensatory lung growth is stimulated only following right PNX (58% resection) but not left PNX (42% resection) suggesting that strain of the remaining lung must exceed a threshold before cellular growth is re-initiated (37 and 38). In contrast, growing young dogs show vigorous compensatory growth of acinar tissue following PNX that completely normalizes alveolar tissue volume, gas exchange and aerobic capacity (85). These findings suggest a possible additive effect of independent stimuli arising from different sources: maturation and PNX.

2.3.3 Remodeling of the Remaining Alveolar-Capillary Network

The resection of lung tissue triggers adaptive reactions in the remaining pulmonary parenchyma. Burri and colleagues (8) showed that in rats after pneumonectomy, initially the airspaces widen affecting the alveolar ducts and shifting later to the alveolar level followed by the rearrangement of the inter-alveolar septa which in turn restores the original volume proportions between alveolar ducts and alveoli. In our previous studies, we also demonstrated that in adult dogs after left PNX (42% resection), compensation in the remaining lung occurs without growth of new alveolar septal tissue (35 and 37). However there were marked changes in the existing structures of the remaining lung including capillary distention, which increases alveolar capillary volume as well as surface area leading to an enhanced diffusing capacity; alveolar septal epithelial cell morphology shifts towards a higher volume fraction of type 2 epithelial cells, with a slight increase in total epithelial cell volume but no net increase in septal

tissue volume (35). The selective epithelial cell response to left PNX represents an early sign of re-initiated cellular growth; as more lung units are resected other septal components are also activated leading to an overt gain in septal tissue volume as seen after right PNX (55% resection) (38).

Chapter 3 Methods and Materials

3.1 Introduction

Methodology including those pertaining to lung resection surgeries, CT scanner calibration, image acquisition and analysis, terminal procedures and morphometric analysis are described in detail in this chapter. All procedures described below were approved by the Institutional Animal Care and Use Committee at the University of Texas Southwestern Medical Center at Dallas. The description of number of animals used, statistical analysis and procedures specific to a particular group are outlined in the relevant chapters.

3.2. Animals

Foxhounds were chosen because regional heterogeneity in lung growth is more pronounced and hence easier to characterize in larger mammals compared to smaller animals. Lobar fissures are also more easily identified by HRCT in dogs than in smaller animals. The lung architecture, growth pattern and time course of response in dogs are similar to those in humans (33). Unlike small rodents that continue to grow throughout their life span, in dogs and large mammals normal lung growth stops upon reaching somatic maturity when the bony epiphyses close, enabling us to examine the mechanisms that re-initiate growth and compensation in the fully mature lung.

3.3 Pneumonectomy

The animals were fasted overnight and premedicated with acepromazine, glycopyrrolate and buprenorphine; anesthetized with isoflurane and intubated with a cuffed endotracheal tube. In a sterile manner the right or left lung was exposed via a lateral thoracotomy in the 5th intercostal space. Blood vessels of each lobe were dissected free and double ligated. The main-stem bronchus was stapled and cut. The lung was then removed and the bronchial stump was oversewn with loose mediastinal tissue for added protection and then immersed under saline to check for leaks. After hemostasis was ensured, the chest wall was closed in five layers. After thorax closure, residual air in the hemithorax was aspirated. Analgesics and antibiotics were given to prevent infection. Sutures were removed in 10 to 14 days (85). Sham animals underwent thoracotomy without lung resection.

3.4 CT scanner calibration

In order to assess the technical performance of the GE high speed CTI scanner at the Aston ambulatory center at UT Southwestern, two kinds of phantoms were used namely, a CATPHAN 500 model (The Phantom Laboratory, Salem NY) and also an American College of Radiology CT Accreditation Phantom. Historically, the CATPHAN had been used for our in house quality assurance program even before UT Southwestern received its accreditation from the American College of Radiology and continues to be in use to this day.

In the following paragraphs I will briefly describe how image quality was assessed using a CATPHAN 500 model phantom (figure 3.1). I chose to describe the

results stemming from the CATPHAN because only CATPHAN had been available a few years ago when some of our data were analyzed. The Catphan phantoms are constructed from modules that fit snugly into a durable 20cm housing. Catphan modules are made from solid-cast materials, eliminating material absorption of water and leaks associated with water bath phantoms, as well as problems related to varied water sources. The Catphan modular design allows test modules to be interchanged based on needs with one of the following modules 1. CTP 401 module used in the assessment of slice width, pixel size and sensitometry (CT number accuracy) 2. CTP 486 image uniformity module.

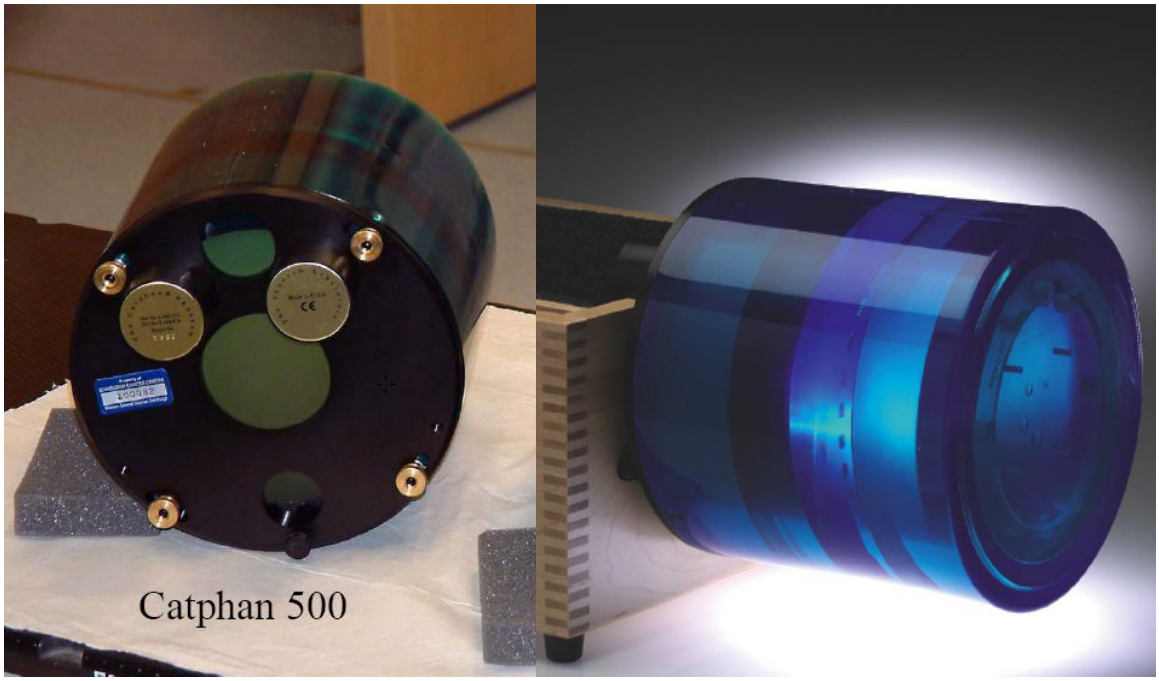

Figure 3.1 Catphan 500 model phantom
(photographs provided generously by Dr. G. Arbique)

The Catphan 500 performs several measurements and tests for scan slice geometry (slice width and sensitivity profile), high resolution (up to 21 line pairs per cm),phantom position verification, subject alignment system verification, supra-slice low contrast sensitivity, subslice low contrast sensitivity, spatial uniformity, scan incrementation,

noise (precision) of CT systems, circular symmetry, sensitometry (linearity), pixel (matrix) size, point spread function and modulation transfer function (MTF) for the x, y, and z axes.

3.4.1 CTP401- Slice Geometry and Sensitometry Module

The CTP 401 module has a diameter of 15cm and is 2.5cm thick. Two sets of opposing wire ramps aligned with the x and y axes are cast into this module. These ramps are used to measure scan slice geometry, verify phantom position, and check the subject alignment system and the scanner table incrementation. The CTP401 module (shown in figure 3.2) uses a 23° ramp angle instead of the 45° angle commonly used in phantoms.

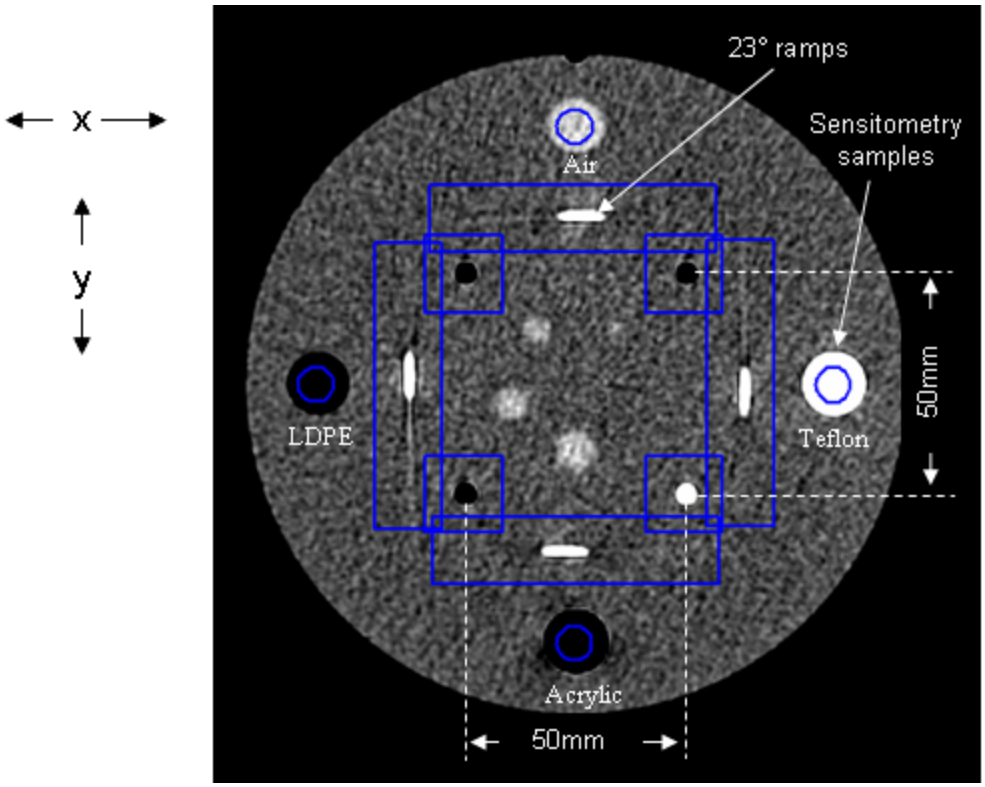

Figure 3.2 Scan image from the CTP 401 (sensitometry module) illustrating the measurement of spatial linearity in x and y axes and CT number assessment by drawing a circular region of interest in center of each material.

As a result, its ramp images are about 2.4 times longer than the images produced with a 45° ramp. This amplified ramp image reduces the effects of imprecise image measurements. The two opposing pairs of ramps allow operators to easily verify whether the phantom is correctly aligned with the scanner axis. By measuring the ratio between opposed ramps, gantry angles up to 10° can be verified, avoiding erroneous measurements.

3.4.1.1 Scan Slice Geometry (Slice width)

To evaluate the slice width (Z mm), the Full Width at Half Maximum (FWHM) length of any of the four wire ramps is measured. The length is then multiplied by a correction factor of 0.42. Figure 3.3 below illustrates the measurement of FWHM for assessing slice width. Table 3-1 shows the slice width measured over a period of 7 years. The difference between the nominal and the measured values of slice width is within ±5%.

3.4.1.2 Scan Incrementation

The wire ramps can be used to test for proper scanner incrementation between slices, and for table movement. A scan is done at a given slice width and then a second scan is completed after incrementing the table by one slice width. The x and y coordinates for the center of each ramp image is established. The distance between these points multiplied by the correction factor of 0.42 measures the scan incrementation.

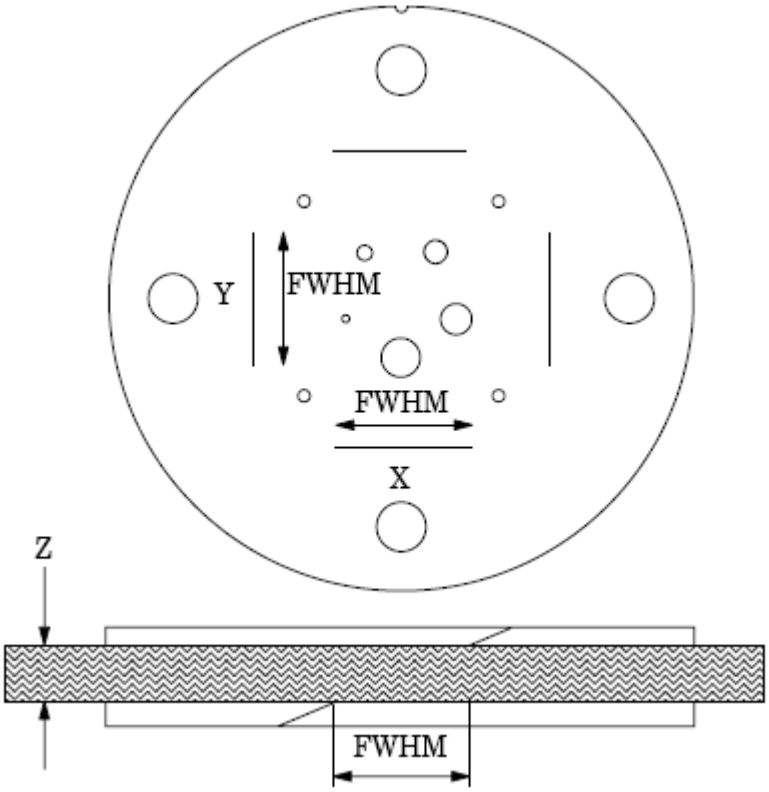

Figure 3.3 Measurement of slice width with the 23° wire ramps. The ramp angle is chosen to offer trigonometric enlargement in the x-y image plane. [Image adapted from Catphan Manual (45)]

Table 3-1 Slice width measurements

Year	2001	2002	2003	2004	2005	2006	2007
Nominal width (mm)	3	3	3	3	3	3	3
Average Width (mm)	3.07	3.14	3.14	3.09	3.07	3.02	3.07
Delta (%)	-2.15%	-4.34%	-4.34%	-2.82%	-2.15%	-0.79%	-2.15%

3.4.1.3 Spatial Linearity of Pixel Size Verification

Four cylindrical test objects (each 3mm in diameter) are positioned to form a 50 mm square at the center of the module. By measuring from center to center the spatial linearity of the CT scanner can be verified (figure 3.2). Pixel size can be calculated by counting the number of pixels between the cylinders in the x and y directions. Table 3-2 below illustrates the accuracy of the distance measured from the year 2001 through 2007. The difference between the nominal and the measured values of distance is within ±1%.

Table 3-2 Distance accuracy measurements

Year	2001	2002	2003	2004	2005	2006	2007
Nominal distance (mm)	50	50	50	50	50	50	50
Measured distance(mm)	49.80	49.90	49.80	50.13	49.93	49.98	49.95
Delta (%)	-0.40%	-0.20%	-0.40%	0.25%	-0.15%	-0.05%	-0.10%

3.4.1.4 Sensitometry (CT Number Linearity)

Four high contrast sensitometric targets surround the wire slice thickness ramps. These targets include materials of differing attenuation namely: **air** (75% Nitrogen, 23.2% Oxygen, and 1.3% Argon), **Low-density polyethylene** (**LDPE;** C_2H_4), **Teflon** (CF_2) and **acrylic** ($C_5H_8O_2$), each 1.2cm in diameter and positioned symmetrically at 1.8cm from edge of the phantom. These targets range from approximately +1000 HU to -1000 HU. Axial images were generated and analyzed. A circular region of interest was drawn in centre of each material (Figure 3.2) and the area, mean pixel value and standard deviation (in pixel value) for region of interest were generated. The CT number of each

material was taken to be the mean pixel value. The final result was obtained by averaging the data over seven years from 2001 to 2007 (Table3-3). A plot illustrating the relationship between the nominal CT numbers of the sensitometric targets and the absolute difference between the actual and measured values is shown below (figure 3.4).

Table 3-3 CT number linearity measurements

Material	Air	LDPE	Water	Acrylic	Teflon
Nominal values (In HU units)	-1000	-90	0	120	1000
2001	-957	-97	7.01	112	899
2002	-958.1	-94.4	6.09	114.6	901.4
2003	-948.4	-94.3	9.32	113.2	854.1
2004	-962.4	-95.8	5.59	112.8	904.2
2005	-962.4	-96.9	4.81	113.5	902.4
2006	-963	-97.2	5.83	114	902.5
2007	-960.3	-95.9	4.81	114.5	903
Mean ±SD (In HU units)	-958.8 ±5.1	-95.9±1.2	6.2±1.6	113.5±0.9	895.2±18.2
Absolute difference between actual and nominal values (In HU units)	-41.2	5.9	-6.4	6.5	104.8

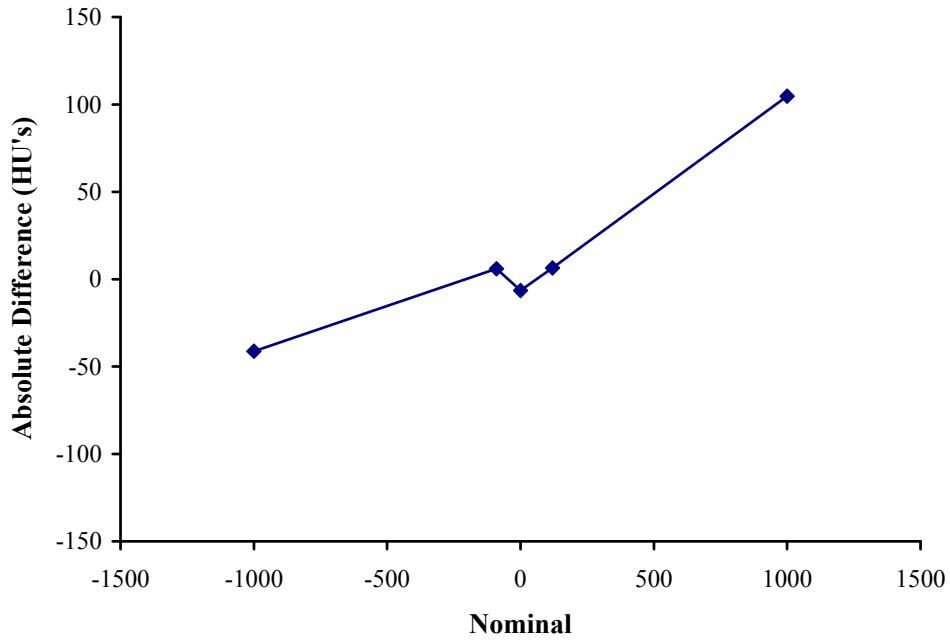

Figure 3.4 Relationship between the nominal CT number of the sensitometric targets and the absolute difference between the actual and measured values.

3.4.2 CTP486 - Uniformity Module

Image noise, spatial uniformity and CT number of water were determined from images of the CATPHAN CTP 486 module. While water is generally considered the ultimate calibration material, many physicists prefer using the CTP 486 solid image uniformity module, because it provides consistent results and is more convenient to use than water. The image uniformity module is cast from a uniform material. The material's CT number is designed to be within 2% (0-20HU) of water's density at standard scanning protocols. The typically recorded CT numbers range from 5H to 18H. This solid material's high radial and axial uniformity makes it an ideal substitute for water as it eliminates variations due to different water sources. The precision of a CT system is evaluated by the measurement of the mean value and the corresponding standard deviations in CT numbers within a region of interest (ROI, Figure 3.5). The mean CT

number and standard deviation of a large number of points in a given ROI of the scan, is determined for central and peripheral locations within the scan image for each type of scanning protocol. Data is inspected for changes from previous scans and for correlation between neighboring slices. CT number measured over a period of six years is within 2% (0-20HU) of water's density (Table 3-4).

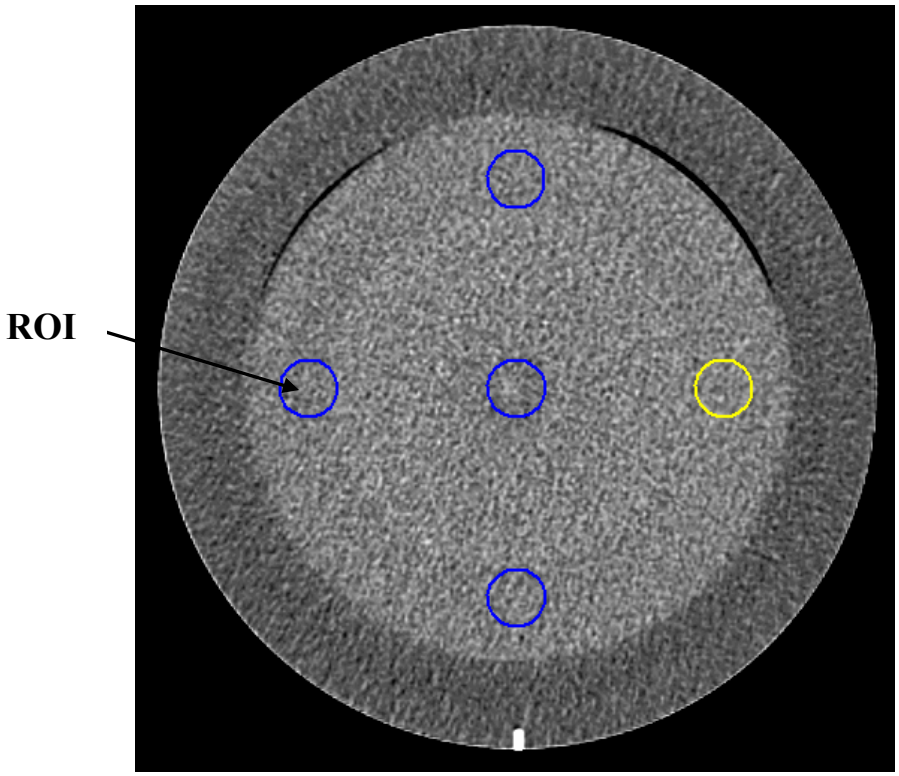

Figure 3.5 Scan image from the CTP486 (image uniformity) module depicting the region of interest in the central and peripheral locations.

Table 3-4 Uniformity and noise measurements

ROI \ YEAR		2001	2002	2003	2004	2005	2006
TOP	*Mean*	7.01	6.09	9.32	5.59	4.81	5.83
	SD	7.01	5.75	3.87	3.93	3.93	4.02
LEFT	*Mean*	6.21	6.43	9.15	5.23	4.91	5.6
	SD	6.07	6.01	3.4	3.49	3.7	3.7
BOTTOM	*Mean*	7.54	6.81	9.7	5.54	4.7	5.35
	SD	5.98	5.38	3.64	3.63	4.42	3.29
RIGHT	*Mean*	7.52	6.03	9.46	5.43	4.59	5.7
	SD	5.92	5.51	3.73	3.45	3.77	4.16
CENTER	*Mean*	7.33	6.51	9.92	5.67	4.69	5.8
	SD	7.01	5.86	3.51	4.32	3.67	3.8
Average		7.12	6.37	9.51	5.49	4.74	5.66
Average SD		6.40	5.70	3.63	3.76	3.90	3.79

3.5 High Resolution CT Image Acquisition

Animals were fasted overnight, sedated with acepromazine (0.15 mg/kg subcutaneously) and atropine (0.023 ml/kg subcutaneously), anesthetized with propofol (4-8 mg/kg intravenous bolus for induction followed by infusion at 0.4mg/[min/kg]), intubated with a cuffed endotracheal tube, placed in the supine position on the CT table and mechanically ventilated (model 607, Harvard Apparatus, Holliston , MA) at a tidal volume (12-15 ml/kg) and respiratory rate sufficient to eliminate spontaneous breathing effort. Spiral CT scan was performed (GE high speed CTI scanner) at 3x3 mm collimation, 120 kV, 250 mA, a pitch of 1.0 and a rotation time of 0.8 seconds. A scout image was first obtained to ensure the field of scan included the entire lung from the apex to the costophrenic angle. Prior to each imaging sequence, the lungs were hyper - inflated

with 3 tidal breaths, followed by passive expiration to functional residual capacity (FRC). Then the endotracheal tube was connected to a calibrated syringe set to deliver a volume of air previously determined to inflate the lungs of each animal to a transpulmonary pressure of 20cmH_20, equivalent to an inflation volume of ~45 ml/kg above FRC. All animals had their static transpulmonary pressure -lung volume relationship measured in duplicate on at least one, sometimes multiple occasions prior to CT scan. Pleural pressure was measured with a balloon tipped catheter inserted into the distal 1/3 of the esophagus; mouth pressure was simultaneously measured to obtain transpulmonary pressure. This pressure was sufficient to prevent atelectasis and permit easy identification of interfaces among lung, rib cage, mediastinal structures and the interlobar fissures; at the same time it is not too high to risk air leak around the endotracheal tube during scanning since the dog has a very wide trachea that becomes further dilated after PNX (15). The breath was held for about 40s while CT images were obtained, after which the animal was reconnected to the respirator. The images were reconstructed at consecutive 1 mm intervals using a 512×512 “standard” kernel resulting in approximately 300 images per animal.

3.6 Analysis of CT images

Images were analyzed using the public domain software Object-Image v.1.6.2 (a public-domain program based on NIH Image by Norbert Vischer, University of Amsterdam, Netherlands) with customized modification developed by us (78). The area occupied by lung tissue was outlined on each image using density thresholding, which excluded conducting structures larger than 1-2 mm diameter. Density thresholding was achieved by selecting a threshold value (average of -317 HU, range -292 to -357 HU) that best

separates the lung from rest of the thoracic components. These threshold values were independently verified by another trained observer in five animals and found to be in agreement with my values (average of -279 HU, range -253 to -310 HU). In our experience, the average CT value of intra-thoracic air is -971 HU (range -961 to -997 HU). The CT value of air-free lung tissue and blood averages 56 HU (range 52 to 59 HU). The HRCT data was examined by two other trained observers in four animals and their air and tissue volume estimates were within 5% of my measurements. Because the air-tissue interface is clearly separated on HRCT, both the inter-observer and intra-observer variability for this method of thresholding was low. The trachea and next 3 generations of large conducting airways were excluded manually by marking them with the background color in each CT image in which they appear. Lung volume of each image is equal to the product of its area and thickness (1 mm); total lung volume was calculated from the sum of the volume of all images. Lobar fissures were identified by following serial images and used to partition the lobes of each lung (figure 3.6).

The CT attenuation value (in Hounsfield Units) of tracheal air and the muscle tissue was measured and the measurement used to partition the total lung volume into volume of air and tissue, since the average CT value of the lung is directly proportional to the ratio of tissue and air. Owing to beam-hardening artifacts and the dynamic range of the scanner, the CT attenuation value for air sampled inside the thorax is slightly lower than that sampled outside the thorax, therefore, the best index of CT value for air (CT_{air}) is at the center of the tracheal air column within the chest. We averaged 3 regions (5mm above the carina, 5mm below the end of the endotracheal tube and half way between the two points) to obtain a mean CT_{air} in each animal. The so-called “tissue volume” (V_{tissue}

in ml) of a region estimated by HRCT includes the volume of alveolar septa as well as extra-septal tissue of structures (airways and vessels) less than 1-2 mm in diameter as well as the blood within these small vessels. We assumed the average CT value for air-free lung tissue and blood (CT_{tissue}) to equal that of muscle and averaged 3 muscles in each animal (infraspinatus, supraspinatus and pectoralis at the level just above the carina).

Using the approach described by others (12, 13, 29, 49, and 93) as well as by us (50, 78, 88 and 100), the total volume of each lobe (V_{lobe} in ml) was partitioned into tissue+blood volume (V_{tissue}) and air volume (V_{air}) as follows:

$$V_{tissue} = \frac{CT_{lobe} - CT_{air}}{CT_{tissue} - CT_{air}} \times V_{lobe} \qquad \text{Equation 3.1}$$

$$V_{air} = V_{lobe} - V_{tissue} \qquad \text{Equation 3.2}$$

where CT_{lobe} = average CT number (in HU) within a lobe.

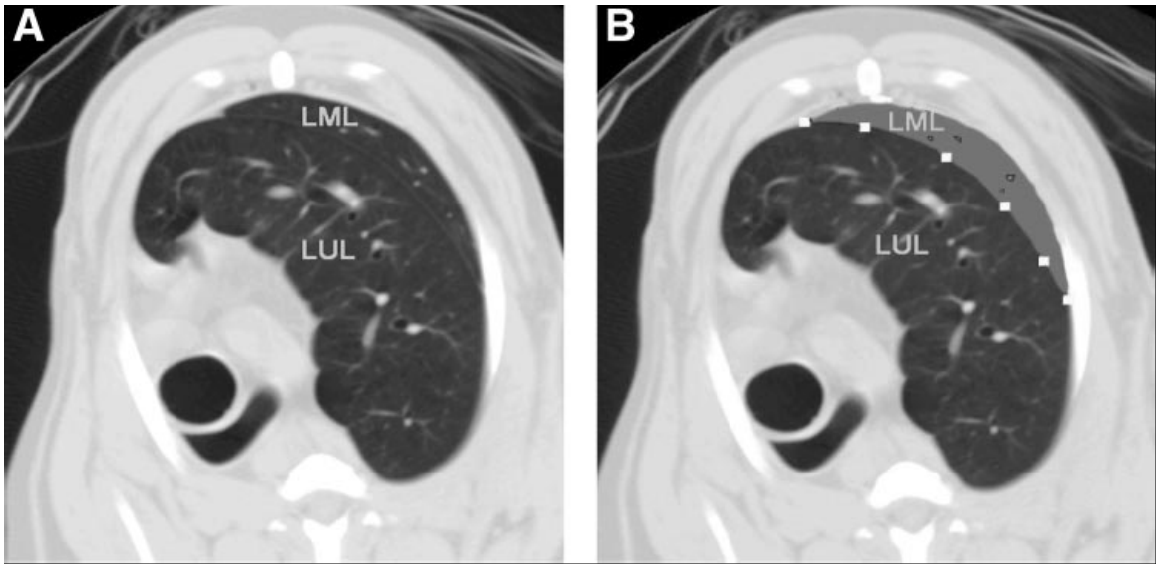

Figure 3.6 CT image from a dog after right pneumonectomy (PNX) (*A*) showing identification of the minor fissure between left upper (LUL) and middle (LML) lobes by cubic spline (*B*; indicated by □) and separation of the areas occupied by LML from that of LUL.

3.7 Terminal Procedure

Animals were fasted overnight and premedicated with atropine; anesthetized with pentobarbital sodium and intubated via a tracheostomy with a cuffed endotracheal tube tied securely to the trachea with umbilical tape. The animal was mechanically ventilated at a tidal volume of 15 ml/kg and a rate of 12 breaths/min. The abdomen was opened via a midline incision. The ventilator was disconnected, and a rent was made through the contra lateral hemidiaphragm to allow collapse of lung on that side. Then the lung was re-inflated within the thorax by tracheal instillation of 2.5% buffered glutaraldehyde at 25 cmH_2O above the highest point of the sternum. An overdose of Euthasol was administered simultaneously. After the flow of fixatives was stopped, the endotracheal tube was clamped, and after 30 minutes the lungs and heart were removed en bloc, immersed in 2.5% buffered glutaraldehyde in a plastic bag, floated on a water bath, and stored at 4°C for over a month before further processing.

3.8 Lung Volume Measurement

The fixed lung was divided into upper and lower strata. The upper stratum consisted of the upper and middle lobes, which were often incompletely separated. The lower stratum consisted of the lower and cardiac lobes in the right lung or just the lower lobe in the left lung. Volume of each intact stratum was measured by the immersion method (95) with the clamps in place to maintain airway pressure. Each stratum was then sliced serially at 2-cm intervals with an electric knife, with the first cut placed at a random orientation. The face of each section was photographed by a 35-mm Nikon camera using Kodak tungsten color film or with a Nikon Coolpix digital camera more recently. A volume estimate of the sectioned lung was obtained from the photographs by point counting using the Cavalieri principle (60), i.e., measuring the slice area by point counting, multiplying by slice thickness, and summing over all slices. Only lung volume estimated by the Cavalieri principle, when the tissue was free from tension, was used in subsequent morphometric calculations.

3.9 Morphometric Analysis

Stereology characterizes physical properties of irregular three -dimensional objects based on measurements made on two -dimensional sections. Sterological methods do not require any assumption on shape or size of the objects under study but use geometric probes to sample the structure and derive three –dimensional measurements in a framework of unbiased sampling, thus relating estimates of structural parameters to the entire organ. The principle of measuring with respect to a reference space is the basis of all stereological methods: each parameter is obtained as the ratio of two measurements,

one estimating the size of the objects under investigation, the other the size of the space in which they are contained, i.e. the reference space. The sampling problem with lung is that the structures of interest with respect to gas exchange are concentrated in the alveolar walls whose dimensions are such as to require fairly high magnifications (~ 19,000 X) for adequate resolution. This limits the sample available to microscopic analysis to a very small size: since the spacing of the alveolar septa is larger than the size of the microscope field the chance that a random field would fall into an empty space (or into a larger vessel or airway) is rather high. Furthermore, the composition of the lung is rather inhomogeneous since about 10-20 % of the lung space is made up of larger structures, such as conducting airways or vessels. Thus, a multi-level or cascade sampling design at different magnifications, wherein the reference space of one level becomes the space of interest (object space) at the next lower level was adopted (96 and 61).

As illustrated in Figure 3.7, the lung is divided into stratum or lobes and each strata or lobe are cut into slices of equal thickness (2 cm), using a random start. The slices are subsequently laid on a flat area without overlapping and 4 blocks of tissue (1 cm^3 in size) are selected from these slices by systematic sampling with a random start, ensuring that all regions are sampled in proportion to their volume. From each block a slice is cut into small dices about 2 mm in diameter (allowing for unbiased orientation), of which 8 dices are picked and processed for embedding in Spurr for high power light microscopy and electron microscopy analysis . Additional blocks are obtained by the same procedure for low power microscopy and embedded in glycol methacrylate.

An established four-level stratified analytical scheme as illustrated in Figure 3.8 was employed for further microscopic analysis: gross (*level 1*, about $\times 2$), low-power

light microscopy (*level 2*, ×275), high-power light microscopy (*level 3*, ×550), and electron microscopy (EM; *level 4*, × 19,000) (96). For *level 1*, photographs of the 2-cm serial sections were analyzed by point counting using standard test grids to exclude structures larger than 1 mm in diameter, to estimate the volume density of coarse parenchyma per unit lung volume. For *level 2*, four blocks per stratum were sampled as described above, embedded in glycol methacrylate for thick sections (5 μm) stained with toluidine blue. One section per block was overlaid with a test grid. From a random start, at least 10 non-overlapping microscopic fields were systematically sampled at ×275 magnification. By using point counting, structures between 20 μm and 1 mm in diameter were excluded to estimate the volume density of fine parenchyma per unit volume of coarse parenchyma.

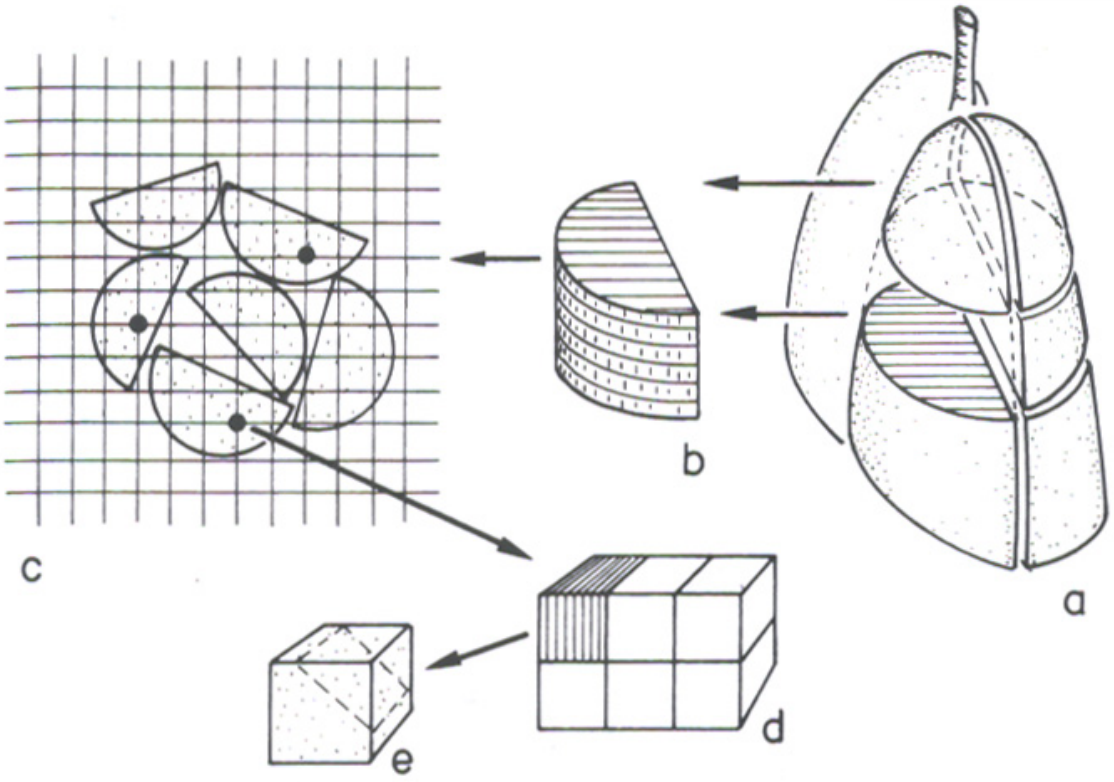

Fig. 3.7 Schematic representation of the sampling protocol. (a) Lung divided into strata or lobe. (b) Stratum or lobe cut into slices, which are subsequently laid on a flat area without overlapping

(see (c)). (c) Sampling of uniform random blocks of tissue by independent uniform random points hitting the slices. (d) Block of tissue diced into smaller blocks. (e) Tissue samples embedded in Spurr or glycol methacrylate for further analysis .Adapted from (61).

For *levels 3* and *4*, four blocks were sampled by a systematic random scheme as described above, postfixed with 1% osmium tetroxide in 0.1 M cacodylate buffer, treated with 2% uranyl acetate, dehydrated through graded alcohol, and then embedded in Spurr. Each block was sectioned at 1μm thickness and stained with toluidine blue. One section per block was overlaid with a test grid at ×550 magnification. From a random start, at least 20 non-overlapping microscopic fields per block were systematically imaged (80 images per stratum) to estimate the volume density of alveolar septa per unit volume of fine parenchyma by excluding all structures exceeding 20 μm in diameter (*level 3*). The fine parenchyma comprised the gas exchange region and served as reference space for EM analysis (65). For *level 4* analysis, two blocks per stratum were sectioned at 80-nm thickness and mounted on copper grids. Each grid was examined with a JEOL EXII transmission electron microscope at approximately ×19,000 magnifications. Thirty non-overlapping EM fields per grid (60 images per stratum) were sampled systematically from a random start, captured with a charge-coupled device camera (Gatan, model C73-0200) and projected onto a Sony high-resolution monitor overlaid with a test grid. Images were also digitized by computer. Septal cells were identified by conventional criteria of typical morphological characteristics (22). The volume densities of epithelium (types I and II), interstitium, and endothelium were estimated by point counting. The alveolar epithelial and capillary surface densities were estimated by intersection counting. At least 300 points or intersections were counted per grid, yielding a coefficient of variation below 10%. The length of test lines (l) that transect the barrier from the epithelial surface

to the nearest red cell membrane were measured to calculate harmonic mean thickness of the tissue-plasma barrier (τhb). The level 4 analysis were performed by Mr. Dennis J. Bellotto of our department.

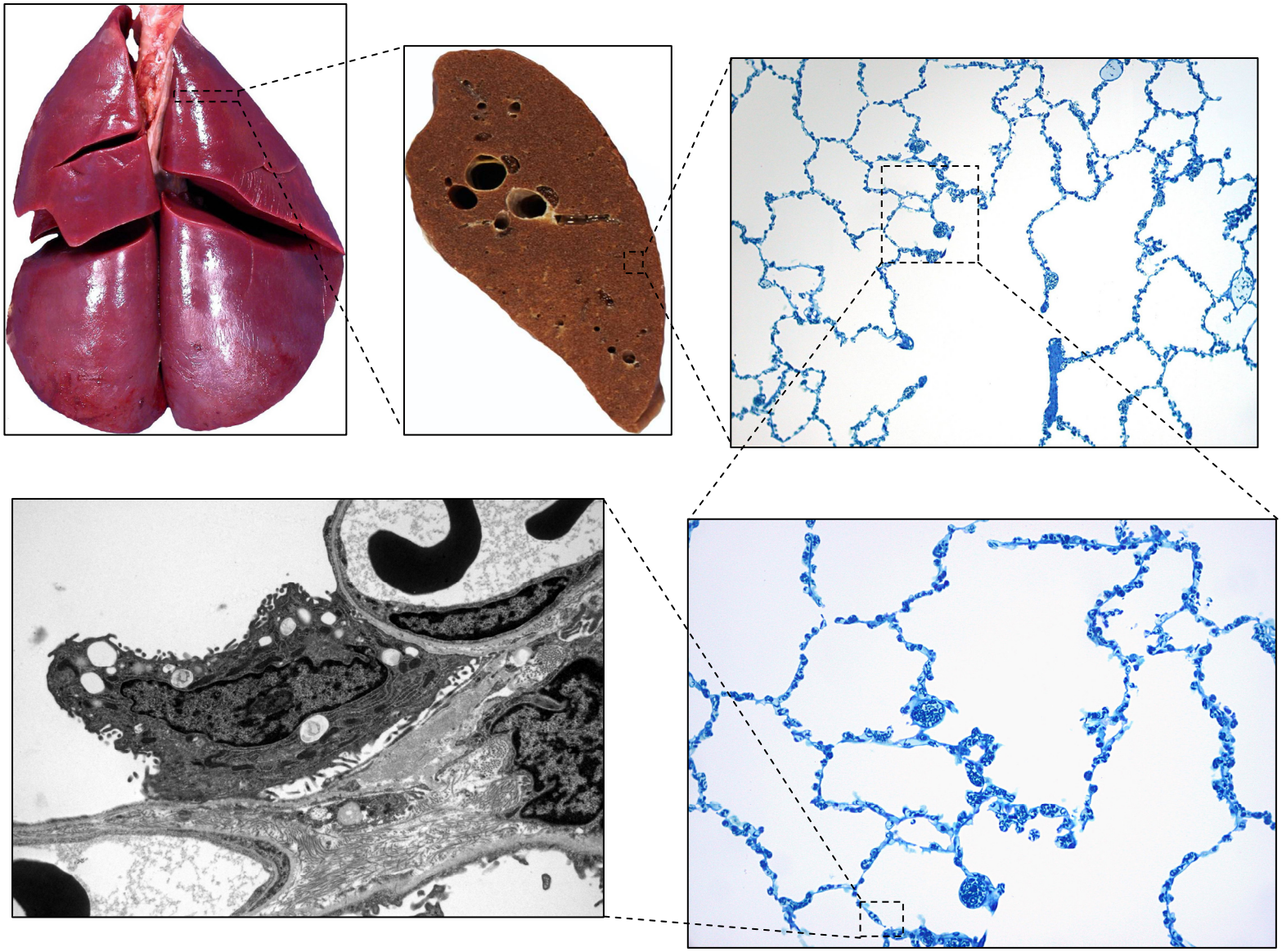

Figure 3.8 Stratified quantification of lung structure Lung structure is analyzed using a stratified morphometric technique; measurements at each level serve as the reference space for the next level of higher magnification. Level I (2x): Serial sections through the whole lobe are photographed to determine absolute lung volume and the volume fraction of large airways and blood vessels. Level II (275x): The volume fractions of arterioles, venules, bronchioles, and the gas exchange regions are determined. Level III (550x): The volume fractions of alveolar walls and alveolar air are determined. Level IV (19,000x): The volume fractions of cells and matrix components (epithelium, interstitium, endothelium), the surface-to-volume ratio of epithelial and endothelial gas exchange surfaces, and the harmonic mean thickness of the diffusion barrier are separately measured under electron microscopy.

Chapter 4 Regional lung growth following left and right pneumonectomy

4.1 Introduction

Experimental lung resection (pneumonectomy, PNX) mimics the loss of functional lung units in chronic parenchymal disease and is a reproducible model for studying the extent and mechanisms of the adaptive response in the remaining normal lung. After PNX, increased mechanical strain imposed on the remaining lung is a potent stimulus for compensatory tissue responses, leading to lung expansion, recruitment of physiological reserves, and partial to complete normalization of gas-exchange capacity (36, 41, and 85). Initiation of compensatory lung growth in adult dogs depends on exceeding a threshold of mechanical strain, as occurs after resection of ~58% of total lung mass by right PNX but not after ~42% resection by left PNX (18 and 19); minimization of lung strain blunts compensatory lung expansion as well as cellular and physiological responses (42, 44, and 100). At postmortem, we routinely observed uneven shape changes among the lobes that remain after PNX. We theorized that regional distribution of post-PNX mechanical strain is heterogeneous, depending on the amount and location of lung tissue removed and on the relative rigidity and asymmetry of mediastinal structures, such as heart, major vessels, and ligaments, that could restrict the direction and extent of regional expansion. Heterogeneous strain distribution could, in turn, influence regional compensatory cellular growth (76 and 103).

To assess the in vivo heterogeneity of regional lung volume after PNX, we performed HRCT scans at a constant transpulmonary pressure in adult foxhounds that

had undergone either left or right PNX and reconstructed each remaining lobe to examine anatomic patterns of lobar expansion. We compared air and tissue volumes of each remaining lobe with that in the corresponding lobe of Sham control animals to determine the in vivo distribution of air and tissue among lobes.

4.2 METHODS AND MATERIALS

4.2.1 Experimental Groups

The Institutional Animal Care and Use Committee at the University of Texas Southwestern Medical Center approved all procedures. Male adult foxhounds (1 yr old) underwent either right PNX (~58% resection, n =12) or left PNX (~42% resection, n = 11) under general anesthesia by previously described procedures (85). Of the animals undergoing right PNX, six animals were scanned during the fourth postoperative month and six additional animals were scanned ~1 yr after surgery. For animals undergoing left PNX, CT scan was performed during the fourth postoperative month. Separate adult control animals underwent thoracotomy without PNX (Sham group, n =7), and were scanned ~10 mo after surgery.

4.2.2 Statistical Analysis

Measurements were normalized by body weight and expressed as means ± SD. Volumes of each lobe were expressed as a fraction of the total volume of each lung. In addition, measurements from PNX animals were expressed as a fraction of the corresponding lobar values in Sham controls. We performed comparisons between

groups by one-way ANOVA and Fisher's multiple comparisons test (StatView version 5.0; SAS Institute, Cary, NC). A *P* value of 0.05 or less was considered significant.

4.3 RESULTS

4.3.1 Lobar Geometry after Right or Left PNX

Figure 4.1 illustrates representative images of the thorax after right and left PNX compared with Sham controls, showing mediastinal shift and enlargement of the remaining lung. Figure 4.2 illustrates the three-dimensional reconstruction of each lobe in different anatomic views. The normal dog has three lobes in the left lung [upper (cranial), middle, and lower (caudal)] and four lobes in the right lung [upper (cranial), middle, lower (caudal), and cardiac]. After right PNX, the left upper and middle lobes expanded across the midline anterior to the heart, whereas the left lower lobe expanded across the midline posterior to the heart. After left PNX, the remaining right upper and cardiac lobes expanded above and below the heart, respectively, whereas the remaining right middle and lower lobes showed relatively little expansion.

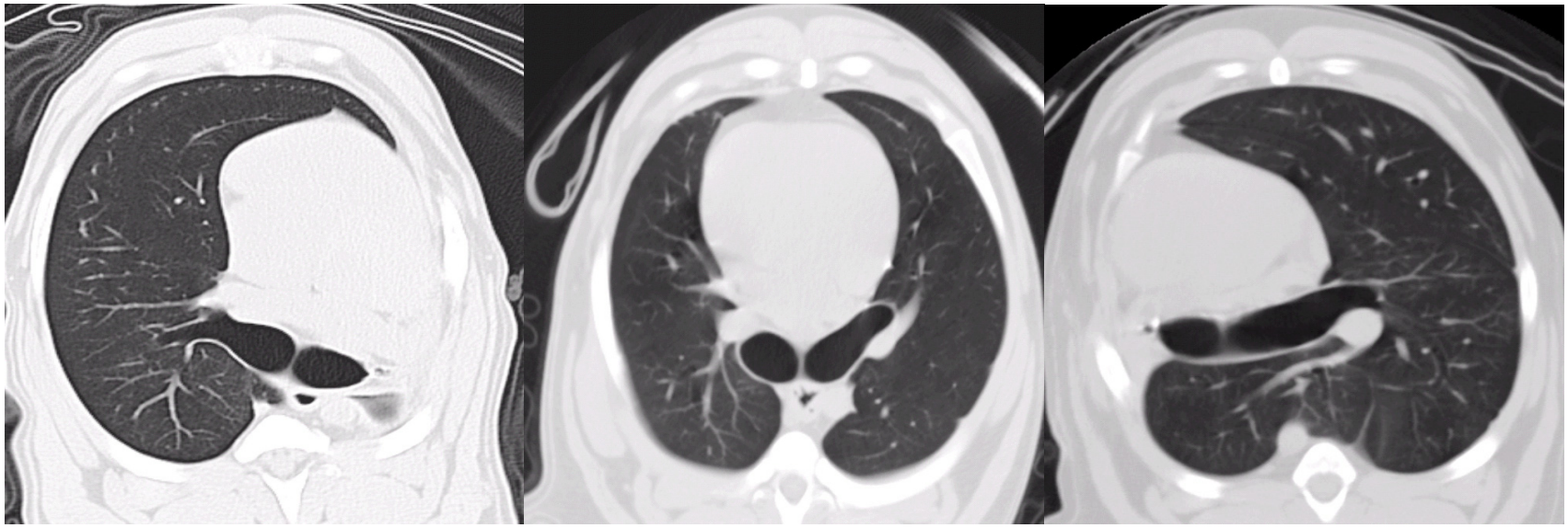

Fig. 4.1 Representative CT images at the level of the carina showing mediastinal shift and enlargement of the remaining lung after left PNX (*left*) or right PNX (*right*) compared with Sham controls (*middle*).

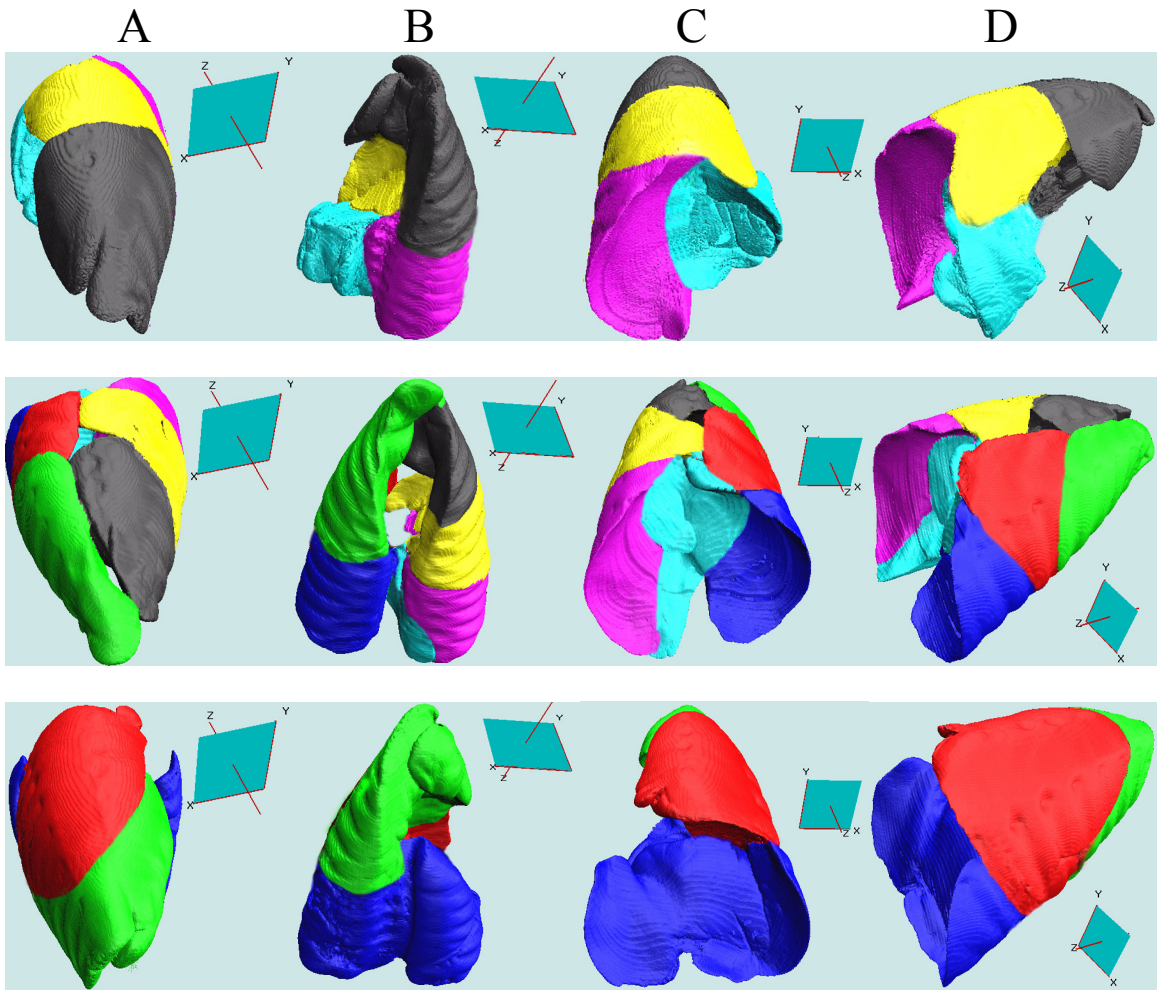

Fig. 4.2 Three-dimensional reconstruction of both lungs in Sham animals, the right lung in animals after left PNX, and the left lung in animals after right PNX, shown in 4 views oriented by their coordinate axes. *A*: anterior view. *B*: posterior view. *C*: caudal view. *D*: anterior-oblique view. Green: LUL or cranial lobe. Red: LML. Blue: left lower or caudal lobe (LLL). Gray: right upper or cranial lobe (RUL). Yellow: right middle lobe (RML). Magenta: right lower or caudal lobe (RLL). Aqua: right cardiac lobe (RCL).

4.3.2 Lobar Volumes after Right PNX

Table 4-1 shows partition of air and tissue volumes among different lobes in the normal left lung (Sham) and in the remaining left lung of animals following right PNX. Volumes of the left upper, middle, and lower lobes comprised 27, 18, and 55% of the total volume of the left lung, respectively; these relative volumes were unchanged after right PNX (29, 22, and 49%, respectively; $P > 0.05$ vs. Sham). After right PNX, lobar volumes of the left lung expressed as a ratio relative to corresponding values from Sham animals were 2.2-fold (upper lobe), 2.6-fold (middle lobe), and 1.9-fold (lower lobe); volume increase was significantly greater for the middle lobe compared with the lower lobe ($P < 0.05$). Lobar air and tissue volumes showed similar patterns of change as total lobar volume (Figure 4.3).

Volume density of lung tissue (ratio of tissue volume to total volume) estimated by CT scan was significantly (19–29%) higher in the left lower lobe than in the upper or middle lobes in all groups (Table 4-1). There was no significant difference in tissue volume density between PNX and Sham groups.

Table 4-1 Lobar volumes in the normal left lung and following right PNX

Group	SHAM	R-PNX
n	7	12
Body wt (kg)	25.2 ± 1.4	25.2 ± 1.1
Tissue volume (ml/kg)		
Left upper lobe	1.0 ± 0.2 †‡	2.4 ± 0.2 *†‡
Left middle lobe	0.6 ± 0.1 §‡	1.6 ± 0.5 *§‡
Left lower lobe	2.3 ± 0.3 §†	4.5 ± 0.7 *§†
Total left lung	3.9 ± 0.5	8.5 ± 1.4 *
Air volume (ml/kg)		
Left upper lobe	9.9 ± 1.8 †‡	23.0 ± 1.8 *†‡
Left middle lobe	6.5 ± 1.0 §‡	17.3 ± 3.8 *§‡
Left lower lobe	19.4 ± 3.3 §†	36.3 ± 3.3 *§†
Total left lung	35.8 ± 4.7	76.6 ± 6.4 *
Tissue volume/total volume		
Left upper lobe	0.088 ± 0.011 ‡	0.095 ± 0.012
Left middle lobe	0.082 ± 0.010 ‡	0.087 ± 0.014 ‡
Left lower lobe	0.105 ± 0.009 §†	0.113 ± 0.016 †
Total left lung	0.096 ± 0.008	0.101 ± 0.020

Values are means ± SD. *n* = no. of animals. PNX, pneumonectomy. $p<0.05$ * vs. Sham group; § $p<0.05$ vs. left upper lobe; † $p<0.05$ vs. left middle lobe; ‡ $p<0.05$ vs. left lower lobe (all by ANOVA).

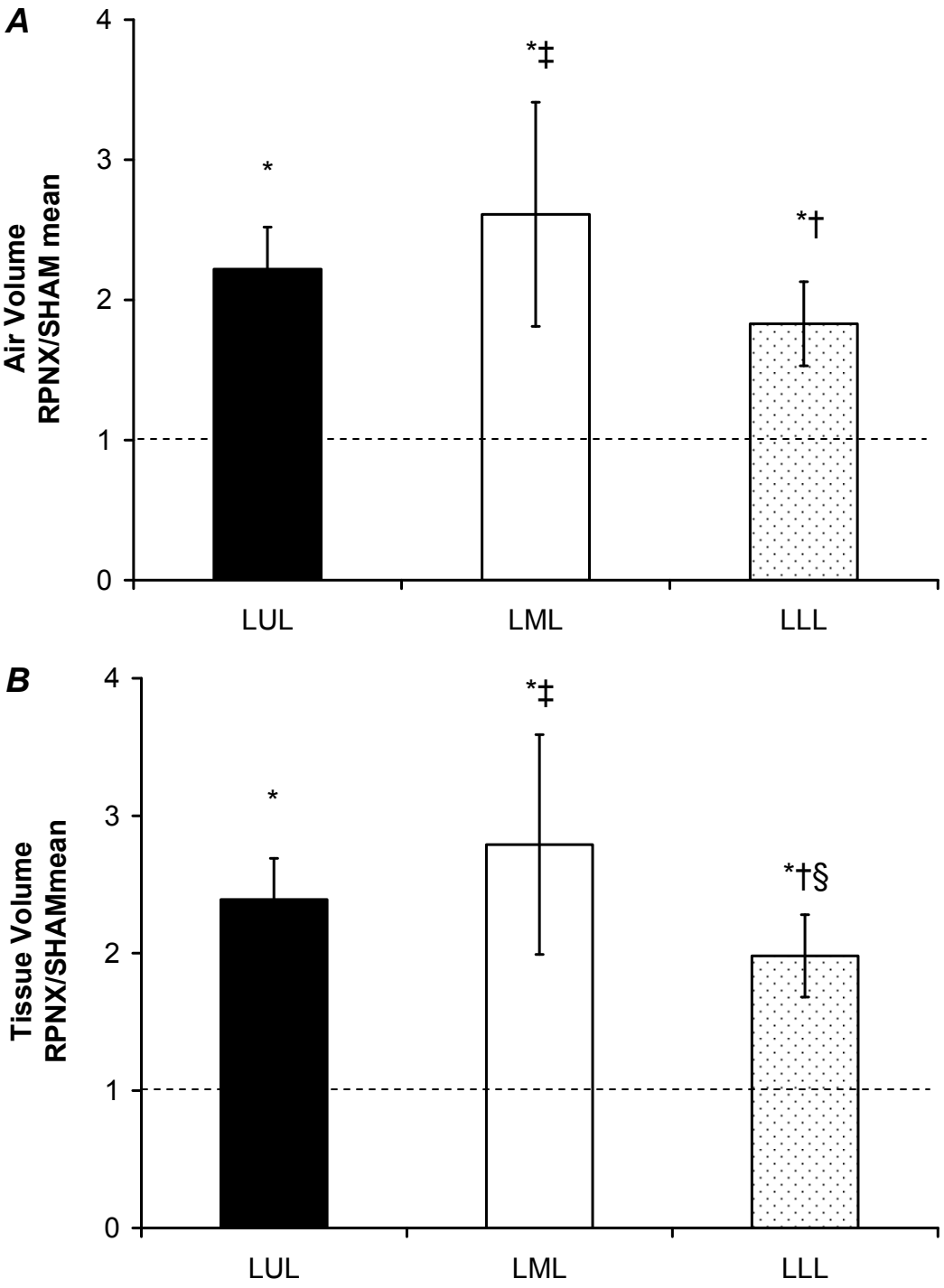

Fig. 4.3 Relative change in lobar air volume (*A*) and tissue volume (*B*) in the remaining left lung following right PNX (RPNX, n =12) expressed as a fraction of the mean value in corresponding lobes of Sham animals (n =7). Values are means ± SD. $P \leq 0.05$ * vs. 1.0 (dashed line; corresponding lobe in Sham controls); § vs. LUL; † vs. LML; ‡ vs. LLL by ANOVA. All remaining lobes expanded significantly but not uniformly after right PNX.

4.3.3 Lobar Volumes after Left PNX

Table 4-2 shows partition of air and tissue volumes among different lobes in the normal right lung (Sham group) and in the remaining right lung of animals after left PNX (Fig. 4.4). In Sham animals, volume of the right upper, middle, lower, and cardiac lobes comprised 20, 25, 40, and 15% of the total volume of the right lung, respectively; corresponding values were not significantly different after left PNX (29, 15, 35, and 20%, respectively; $P > 0.05$ left PNX vs. Sham group). After left PNX, lobar air and tissue volumes of the right lung expressed as a ratio relative to corresponding Sham values (Fig. 4.4) were 2.2 (upper lobe), 0.9 (middle lobe), 1.3 (lower lobe), and 2.1 (cardiac lobe); volume increased significantly in the upper and cardiac lobes ($P < 0.05$) but not in the middle or lower lobes.

In all groups, volume density of tissue estimated by CT scan was significantly (14–29%) higher in the right lower and cardiac lobes than in the right upper or middle lobes (Table 4-2). In Sham animals, tissue volume densities in corresponding lobes of the right and left lung are similar (Tables 4-1 and 4-2). However, tissue volume densities were systematically lower in animals after left PNX than in corresponding lobes of Sham animals, reaching statistical significance for the right middle, lower, and cardiac lobes (~15–25% lower) but not for right upper lobe (~10–12% lower).

Table 4-2 Lobar volumes in the normal right lung and following left PNX

Group	SHAM	L-PNX
n	7	11
Body wt (kg)	25.2 ± 1.4	25.4 ± 4.2
Tissue volume (ml/kg)		
Right upper lobe	0.9 ± 0.3 ‡	1.8 ± 0.2 *†‡
Right middle lobe	1.2 ± 0.5 ‡ψ	0.9 ± 0.2 §‡ψ
Right lower lobe	2.3 ± 0.3 §†ψ	2.5 ± 0.2 §†ψ
Right cardiac lobe	0.8 ± 0.1 †‡	1.4 ± 0.3 *†‡
Total right lung	5.2 ± 0.8	6.6 ± 0.7 *
Air volume (ml/kg)		
Right upper lobe	10.2 ± 3.8 ‡	23.2 ± 2.1*†‡ψ
Right middle lobe	12.5 ± 4.1 ‡ψ	12.8 ± 3.5 §‡
Right lower lobe	19.9 ± 3.7 §†ψ	27.8 ± 0.9 §†ψ
Right cardiac lobe	7.2 ± 1.2 †‡	16.0 ± 2.5 *§‡
Total right lung	49.8 ± 7.5	79.8 ± 5.4 *
Tissue volume/total volume		
Right upper lobe	0.080 ± 0.008 ‡ψ	0.072 ± 0.007 ‡ψ
Right middle lobe	0.087 ± 0.011 ‡ψ	0.067 ± 0.005 *‡ψ
Right lower lobe	0.103 ± 0.007 §†	0.083 ± 0.005 *§†
Right cardiac lobe	0.099 ± 0.006 §†	0.083 ± 0.006 *§†
Total right lung	0.094 ± 0.005	0.077 ± 0.005 *

Values are means ± SD; n = no. of animals. $P \leq 0.05$ * vs. Sham group; † vs. right middle lobe; ‡ vs. right lower lobe; § vs. right upper lobe; ψ vs. right cardiac lobe (all by ANOVA). There were no significant differences between retinoic acid and placebo groups.

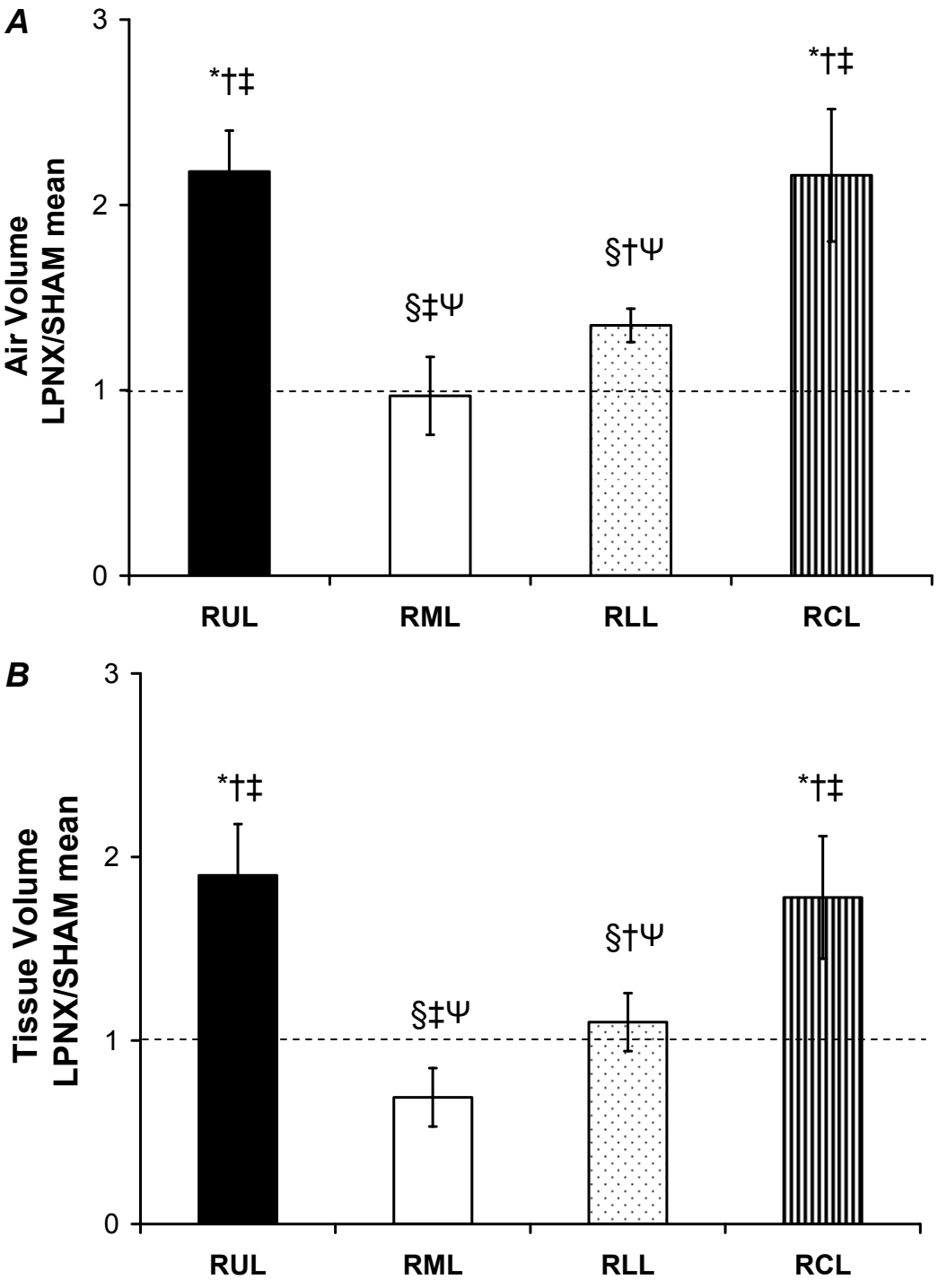

Fig. 4.4 Relative change in lobar air volume (*A*) and tissue volume (*B*) in the remaining right lung after left PNX (LPNX, $n = 11$) expressed as a fraction of the mean value in corresponding lobes of Sham animals ($n = 7$). Values are means ± SD. $P \leq 0.05$ * vs. 1.0 (dashed line, corresponding lobe in Sham controls); § vs. right upper lobe (RUL); † vs. RML; ‡ vs. RLL; ψ vs. right cardiac lobe (RCL) by ANOVA. Volume of RUL and RCL doubled after LPNX, whereas that of RML and RLL did not expand significantly.

4.3.4 Changes in Overall Lung Volumes

In Sham animals, average tissue and air volumes of the right lung constituted 57% of the total respective volume of both lungs. After right PNX, average air and tissue volumes of the remaining left lung increased proportionally (108 and 115%, respectively, above Sham left lung); thus the overall volume density of tissue remained unchanged (Table 4-1). After left PNX, the average air volume of the remaining right lung was 54% higher than in the right lung of Sham animals, and tissue volume was only 21% higher; therefore, the overall volume density of tissue was significantly (18%) lower (Table 4-2).

4.4 DISCUSSION

4.4.1 Summary of Findings

Divergent patterns of regional lung expansion were observed in adult dogs in response to different forms of lung resection. After right PNX, mediastinal shift is prominent and all remaining lobes expanded significantly (1.9- to 2.6- fold of that in corresponding Sham lobes), with the greatest expansion occurring in the left upper and middle lobes. In contrast, after left PNX, the remaining right upper and cardiac lobes enlarged approximately twofold across the midline above and below the heart to reconstitute a compliant cardiac fossa, whereas the remaining right middle and lower lobes did not expand significantly. These anatomic changes reflect non-uniform in vivo distribution of intrathoracic mechanical strain after PNX. Lobar expansion is greater in magnitude and uniformity after right PNX than after left PNX, related to differential anatomic restrictions imposed by the asymmetry and relative rigidity of the heart, mediastinal great vessels, and cardiophrenic ligaments. Density gradients were analyzed

to quantify regional volume density of tissue. After right PNX, lobar tissue volume increased in proportion to air volume; hence, volume density of tissue was unchanged, consistent with morphometric evidence of compensatory growth of acinar tissue (38). After left PNX, lobar tissue volume either did not increase or the increase lagged behind that in air volume, consistent with previous morphometric reports showing a lack of compensatory growth of alveolar tissue (37 and 44).

4.4.2 Regional Post - PNX Compensatory Response

Sekhon and Thurlbeck (84) found in growing rats after left PNX that volume expansion was greatest in the postcaval (cardiac) lobe followed by the middle lobe of the remaining right lung. In post-PNX dogs, we routinely observed at postmortem irregular shape changes in the remaining lung, particularly in the upper and cardiac lobes after left PNX and in the upper and lower lobes after right PNX. These lobes show odd-looking projections of tissue that herniate across the apical midline (upper lobe) or wrap around the caudal esophagus (lower or cardiac lobe), where the lack of rigid ligaments allow lung expansion in response to chronic mechanical stress. In our previous morphometric analysis, we did not separately analyze each lobe. We routinely fixed the lung by tracheal instillation of fixatives at a constant hydrostatic pressure (37 and 38). Each lung was then divided into upper and lower strata while the airway pressure was maintained. The upper stratum consisted of the upper and middle lobes. The lower stratum consisted of either the lower lobe alone (left lung) or lower and cardiac lobes (right lung). This division was employed because the upper and middle lobes are often incompletely separated; forced separation causes loss of airway pressure and hence variability in lung volume measurement by the saline immersion method (95). Using this sampling method, we

reported that, in adult dogs after left PNX, volume of septal tissue measured by morphometry was not different from that in the same lung of normal animals and average volume density of alveolar septum per unit lung volume was significantly reduced (~0.12 in normal dogs and ~0.09 after left PNX) (37). Because blood volume in the remaining lung increases post-PNX and CT derived tissue volume includes volume of blood in small vessels, the 27% higher absolute tissue volume in the remaining lung after left PNX is not surprising; however, average volume density of tissue remains 18% lower than that in normal animals (~0.094 in Sham dogs and ~0.077 after left PNX) (Table 2), consistent with morphometric results. Post- PNX reduction in tissue volume density was greater in the middle and lower lobes (~20–25%) than in the upper and cardiac lobes (~10–15%) (Fig. 4.3). Because the upper and lower stratum each contained one lobe that expanded significantly and one that did not, grouping two lobes into one stratum may obscure interlobar differences in structural adaptation even though no overall compensatory alveolar growth was evident by either CT scan or morphometry. We now use a modified postmortem sampling method to measure volume of each lobe separately by point counting (101).

In adult dogs after right PNX, the remaining lobes expanded more uniformly and to a greater extent than after left PNX; hence, grouping left upper and middle lobes into the upper stratum would not bias morphometric analysis. The more vigorous lobar expansion after right PNX is associated with proportional increases in alveolar septal cell volumes in the remaining lobes, such that volume density of alveolar septa per unit lung volume remained unchanged (average 0.11–0.12), leading to a 61% increase in lung diffusing capacity estimated by both morphometric as well as physiological methods (38

and 39). In parallel with these prior findings, CT-derived tissue volume density after right PNX is also not different from that in Sham controls (average ~0.10) (Table 4-1). The pattern of volume expansion to structural growth after different types of lung resection suggests that compensatory tissue response is influenced not only by the magnitude of regional mechanical strain but also by its distribution.

4.5 Conclusion

In conclusion, we report distinct patterns of lobar expansion after left and right PNX, which reflect nonuniform regional distribution of mechanical lung strain stemming from constraints imposed by rigid mediastinal structures such as the heart, great vessels, and ligaments. The increase in mechanical lung strain is greater in magnitude and more uniformly distributed after right than after left PNX. Heterogeneity in regional strain distribution may influence local histological response and compensatory alveolar growth after lung resection. Direct verification of regional pressures would require implantation of multiple pleural and/or parenchymal markers that have not yet been done.

Chapter 5 Effect of Non-uniform Post-Pneumonectomy Signals on Postnatal Lung Growth

5.1 Introduction

During development, mechanical force imposed on lung tissue by an enlarging rib cage is a major stimulus for postnatal lung growth and maturation (34); this stimulus ceases upon somatic maturity when the bony epiphyses close and both the rib cage and lungs reach their final dimensions. Following resection of one lung by pneumonectomy (PNX), the negative intrathoracic pressure causes the remaining lung to expand, deform and eventually fill the empty hemithorax, creating a potent stimulus for triggering the pathways of compensatory alveolar growth and airway remodeling.

Compensatory lung growth is more vigorous and functional restoration more complete in dogs undergoing PNX as puppies than as adults (85 and 86). In adult dogs compensatory lung growth is initiated only when more than ~50% of the lung is removed, suggesting the existence of a threshold of mechanical signals that must be exceeded before cellular growth is re-initiated (37 and 38) as well as the possibility of additive effects of independent mechanical signals arising from different sources, i.e., maturation and PNX, on alveolar growth.

Mechanical signals from maturation and PNX are known to exert additive effects on airway compensation. Normal growth and remodeling of airways lags behind that of parenchyma (so called *dysanaptic lung growth*) and the lag is further exaggerated by PNX. In growing puppies pneumonectomized at 2.5 mo of age, we observed lengthening

of the remaining airways without dilatation 4 mo post-PNX; dilatation became evident subsequently and significantly reduced airways resistance by 10 mo post-PNX (15).

Dysnaptic growth offsets some of the benefit expected from alveolar growth; long-term compensatory increases in alveolar dimensions and diffusing capacity of the remaining lung were greater in animals pneumonectomized as puppies than as adults while the long-term compensatory reduction in work of breathing was similar in puppies and adults (15 and 86).

In adult dogs after right or left PNX where lung resection imposed the only stimulus for compensatory lung growth or remodeling, lobar expansion and parenchymal growth of the remaining lung was non-uniform (78), likely reflecting the anatomical asymmetry of mediastinal structures and ligaments that differentially restrained expansion and growth of the remaining lobes. No previous study has longitudinally followed the pattern or time course of post-PNX regional lung growth during somatic maturation. We hypothesized that the additive effects from two sources of mechanical signals, maturation and PNX, further exaggerates non-uniformity of compensatory growth above and beyond that in post-PNX adult animals where there was only one source of signals. We performed high-resolution computed tomography (HRCT) at a constant transpulmonary pressure in growing foxhounds that had undergone right PNX at 2.5 mo of age in comparison with litter-matched control (SHAM) animals. Scans were performed at two time points (4 and 10 mo after surgery corresponding to 6.5 and 12.5 mo of age, i.e., before and after somatic maturity). By identifying the lobar fissures we reconstructed each lobe and compared lobar air and tissue volumes between experimental groups and at the two ages. The main findings were as follows: a) Regional

compensatory growth of lung parenchyma was uniform at 4mo but became non-uniform by 10mo post-PNX; growth of the remaining left lower (caudal) lobe gradually lagged behind the other lobes. b) At maturity the pattern of regional non-uniformity was similar whether animals underwent PNX as puppies or as adults. We conclude that while superimposing post-PNX signals on developmental signals alters some aspects of compensatory lung growth it does not alter the non-uniform pattern of growth.

5.2 Methods and Materials

5.2.1 Experimental Groups

Foxhounds (2.5 mo of age) underwent either right PNX (55-58% lung removed, n=9) or right thoracotomy without lung resection (SHAM, n=7) under general anesthesia by procedures previously described in chapter 3. The CT scan was performed during the 4^{th} month following surgery (6.5 mo of age, n=5 PNX, n=6 SHAM) and repeated 10 mo after surgery (~1 year of age, n=9 PNX, n=7 SHAM).

5.2.2 Statistical Analysis

Measurements were normalized by body weight and expressed as mean±SD. Measurements from PNX animals were expressed as a fraction of the corresponding lobar values in SHAM controls. Comparison between groups was by analysis of variance with post-hoc Fisher's multiple comparisons test. Longitudinal data between 4 and 10 mo following surgery were compared by repeated measures ANOVA. We used a commercial statistical package (STATVIEW v.5.0, SAS Institute, Cary, NC). A p value of 0.05 or less was considered significant.

5.3 Results

Representative images of three-dimensional lobar reconstruction from PNX and Sham groups at 4 and 10 mo after surgery are shown in Fig. 5.1. Following right PNX, mediastinal shift was prominent and all the remaining lobes expanded significantly but nonuniformly. The left cranial or upper lobe (LUL) and the left middle lobe (LML) expanded anteriorly across the midline; the left caudal or lower lobe (LLL) assumed a highly irregular shape as it expanded posteriorly across the midline behind the heart, esophagus, and great vessels. Within the grossly distorted LLL, the average CT attenuation value of the portion that herniated across the midline posterior to the esophagus (-810 ± 17 HU, ± SD) was slightly more positive but not significantly different from the CT values of the rest of the lobe (-839 ± 11 HU, $P > 0.05$).

A

Sham Both Lungs

4 mo

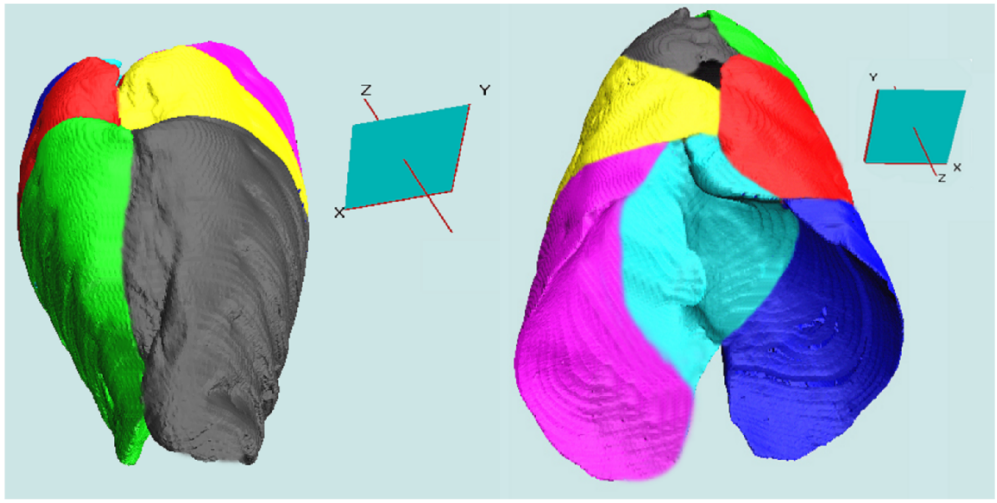

10 mo

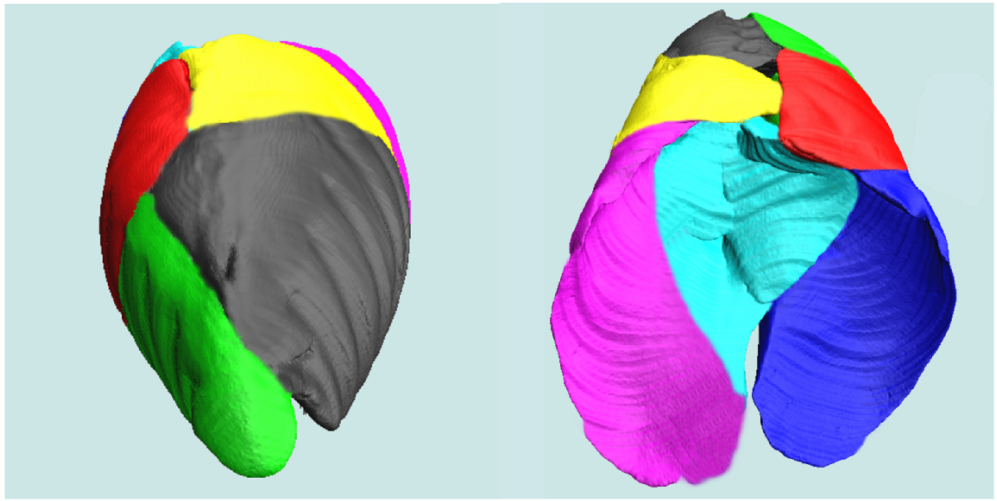

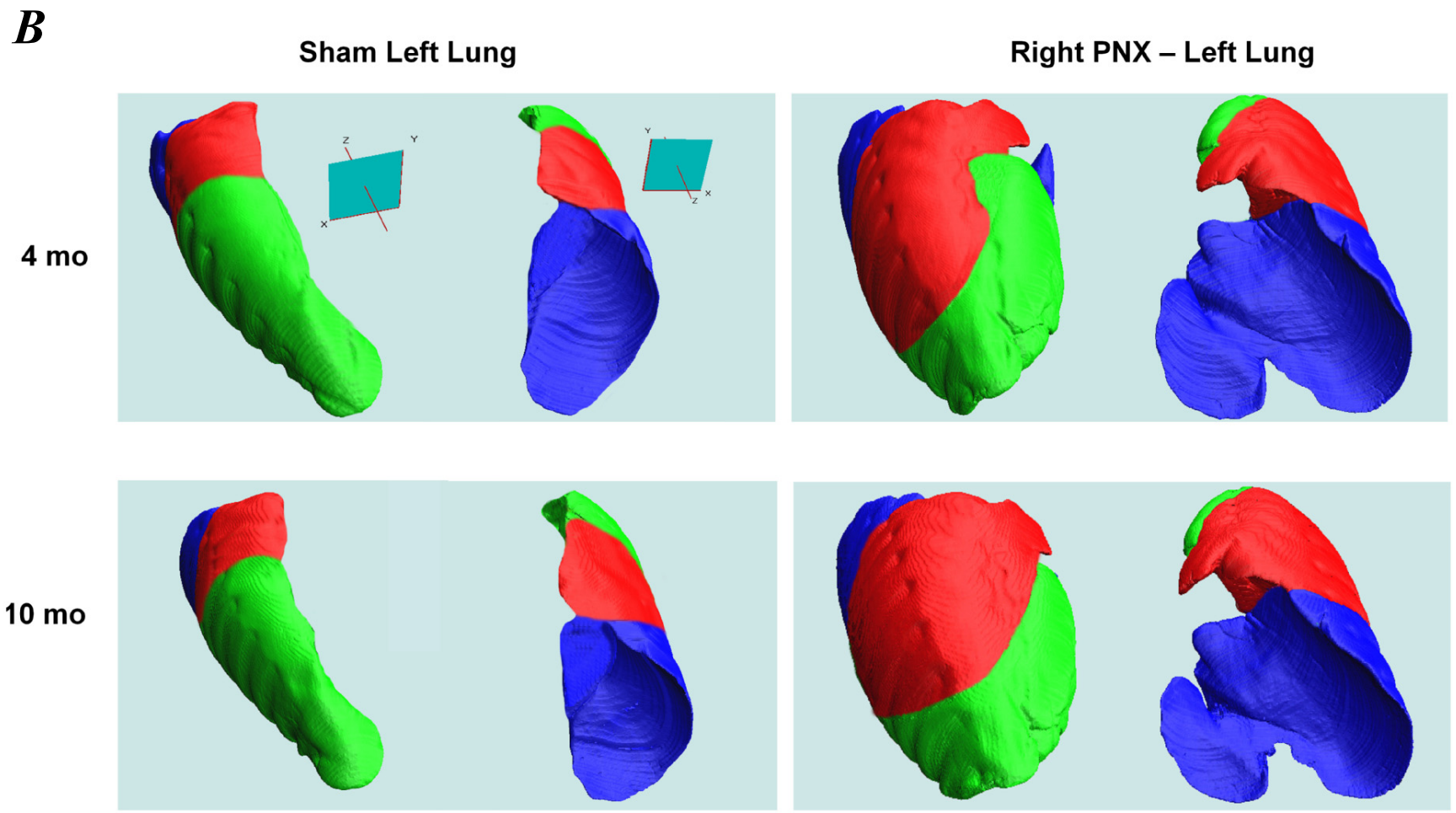

Fig. 5.1 Three-dimensional reconstruction of both lungs (*A*) and the left lung (*B*) alone in 1 control animal (SHAM) and the left lung in 1 animal after right pneumonectomy (PNX) at 4 and 10 months after surgery, each shown in 2 views oriented by their coordinate axes: dorsal view and caudal view. Green, left cranial or upper lobe (LUL); red, left middle lobe (LML); blue, left caudal or lower lobe (LLL); gray, right cranial or upper lobe (RUL); yellow, right middle lobe (RML); magenta, right caudal or lower lobe (RLL); aqua, right infra-cardiac lobe (RCL).

The distribution of lobar volume 4 and 10 mo after surgery (6.5 and 12.5 mo of age) is shown in Table 5-1. At each time point after PNX, total lung air and tissue volumes were not different from that in lungs of both sham-operated controls. In control animals, air and tissue volumes of the right upper, middle, lower, and infra-cardiac lobes consisted of ~12%, 14%, 23%, and 9%, and the left upper, middle, and lower lobes 12%, 7% and 23%, respectively, of total air or tissue volume. These values compare reasonably well with the corresponding canine lungs by Rahn and Ross (73): 17%, 9%, 25%, and 8% for the right lung; 10%, 6%, and 26% for the left lung. In PNX animals, the remaining left upper middle and lower lobes constitute ~30%, 21%, and 49% of total lung air volume, and 27%, 18%, and 55% of total lung tissue volume, respectively. Body mass-specific lobar air volume did not change between 4 and 10 mo postsurgery in either group. Body mass-specific lobar tissue volume declined between 4 and 10 mo, reaching statistical significance in all lobes of the left lung in the Sham group and in the left lower lobe of the PNX group (Fig. 5.2).

Table 5-1 Lobar tissue and air volume in the normal left lung and after right pneumonectomy before and after reaching somatic maturity

Lung	**Sham Right Lung**		**Sham Left Lung**		**Right PNX**	
Post- surgery	4 mo	10 mo	4 mo	10 mo	4 mo	10 mo
Number	6	7	6	7	5	9
Weight (kg)	22.9 ± 5.8	25.2 ± 3.1	22.9 ± 5.8	25.2 ± 3.1	22.5 ± 4.3	27.4 ± 4.6 §
Air volume (ml/kg)						
Upper Lobe	8.1 ± 1.7 ‡	10.2 ± 3.9	10.1 ± 1.7 ‡	9.9 ± 1.8 ‡	23.6 ± 2.6 *‡	23.0 ± 2.8 *‡
Middle Lobe	12.7 ± 1.2 $^{\Psi}$	12.5 ± 4.1 $^{\Psi}$	7.2 ± 1.0	6.5 ± 1.0	16.5 ± 5.8 *	17.3 ± 5.8 *
Lower Lobe	19.7 ± 2.1 $^{\dagger\ddagger\Psi}$	19.9 ± 3.8 $^{\dagger\ddagger\Psi}$	19.9 ± 2.1 †‡	19.4 ± 3.3 †‡	39.1 ± 3.5 *†‡	36.3 ± 5.3 *†‡
Cardiac Lobe	7.0 ± 0.8	7.2 ± 1.3	-	-	-	
Total L Lung	47.6 ± 3.9	49.8 ± 7.5	37.2 ± 3.7	35.9 ± 4.8	79.2 ± 5.4 *	76.5 ± 9.4 *
Tissue volume (ml/kg)						
Upper Lobe	0.8 ± 0.1 ‡	0.9 ± 0.4	1.2 ± 0.2 ‡	1.0 ± 0.2 ‡§	2.7 ± 0.7 *	2.4 ± 0.5 *‡
Middle Lobe	1.7 ± 0.1 $^{\Psi}$	1.2 ± 0.5 $^{\Psi}$	0.8 ± 0.1	0.6 ± 0.1 §	1.8 ± 0.7 *	1.6 ± 0.5 *
Lower Lobe	2.6 ± 0.3 $^{\dagger\ddagger\Psi}$	2.3 ± 0.4 $^{\dagger\ddagger\Psi}$	2.6 ± 0.3†‡	2.3 ± 0.3 †‡§	5.5 ± 1.2 *†‡	4.5 ± 0.7 *†‡§
Cardiac Lobe	0.9 ± 0.1	0.8 ± 0.1	-	-	-	-
Total L Lung	6.1 ± 0.3	5.2 ± 0.8 §	4.7 ± 0.3	3.8 ± 0.5 §	10.1 ± 2.4 *	8.5 ± 1.4 *

Mean±SD, * p≤ 0.05 vs. SHAM; † p≤ 0.05 vs. upper lobe; ‡ p≤ 0.05 vs. middle lobe; ψ p≤ 0.05 vs. cardiac lobe; § p≤ 0.05 vs. 4 months after surgery (6 months of age) by ANOVA.

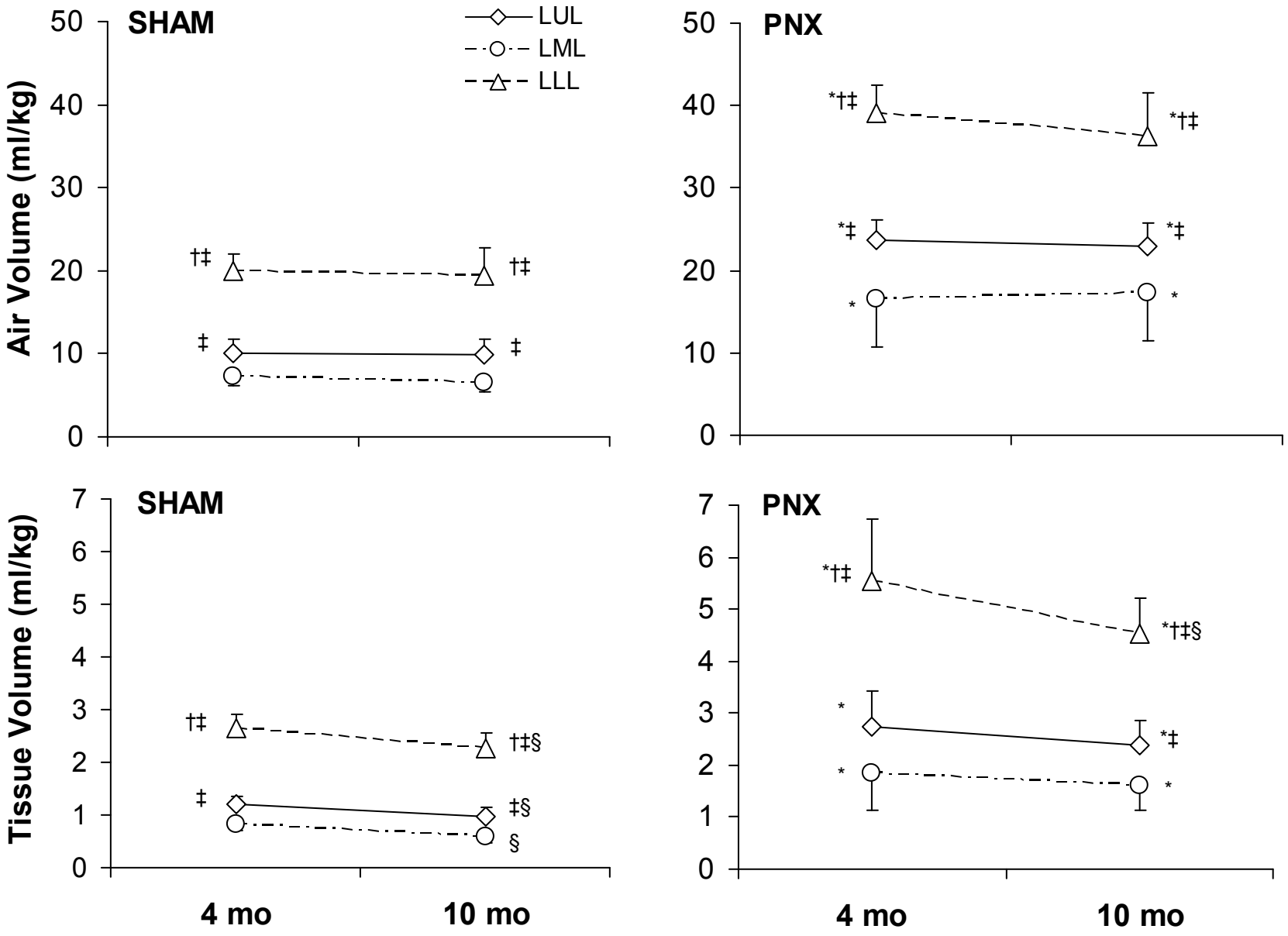
SHAM
LUL
LML
LLL
Air Volume (ml/kg)
50
40
30
20
10
0
†‡
†‡
‡
‡
PNX
*†‡
*†‡
*‡
*‡
*
*
SHAM
Tissue Volume (ml/kg)
7
6
5
4
3
2
1
0
†‡
†‡§
‡
‡§
§
PNX
*†‡
*†‡§
*
*‡
*
*
4 mo
10 mo
4 mo
10 mo

Fig. 5.2 Air and tissue volume of the left lung (per/kg body wt) 4 and 10 months after surgery (SHAM: *left*; right PNX: *right*). Mean ± SD. At each time point lobar values are significantly higher in the PNX group than the SHAM group. Compared with corresponding lobar values 4 mo after surgery, tissue volume is significantly lower at 10 months in all the lobes of SHAM control animals and in the left lower lobe of PNX animals. $P \leq 0.05$ by ANOVA: * vs. corresponding SHAM control, † vs. upper lobe and ‡ vs. middle lobe at the same time point, § vs. 4 months after surgery.

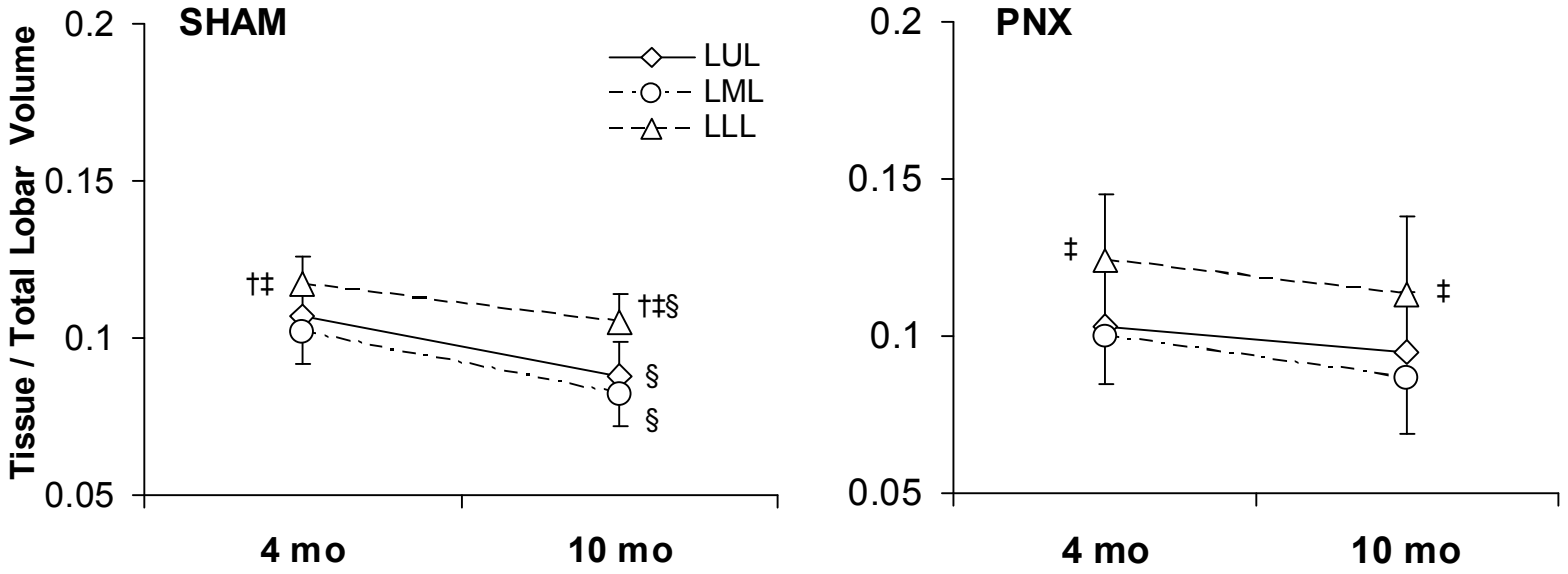

Fig. 5.3 Tissue volume fraction (ratio of lobar tissue volume to total lobar volume) was higher in the left lower lobe than other lobes of the left lung in both groups (SHAM, *top*; right PNX, *bottom*), and declined between 4 and 10 months after surgery, reaching statistical significance in all lobes of the SHAM control animals. Mean ± SD. $P \leq 0.05$ by ANOVA: † vs. upper lobe and ‡ vs. middle lobe at the same time point; § vs. 4 months after surgery.

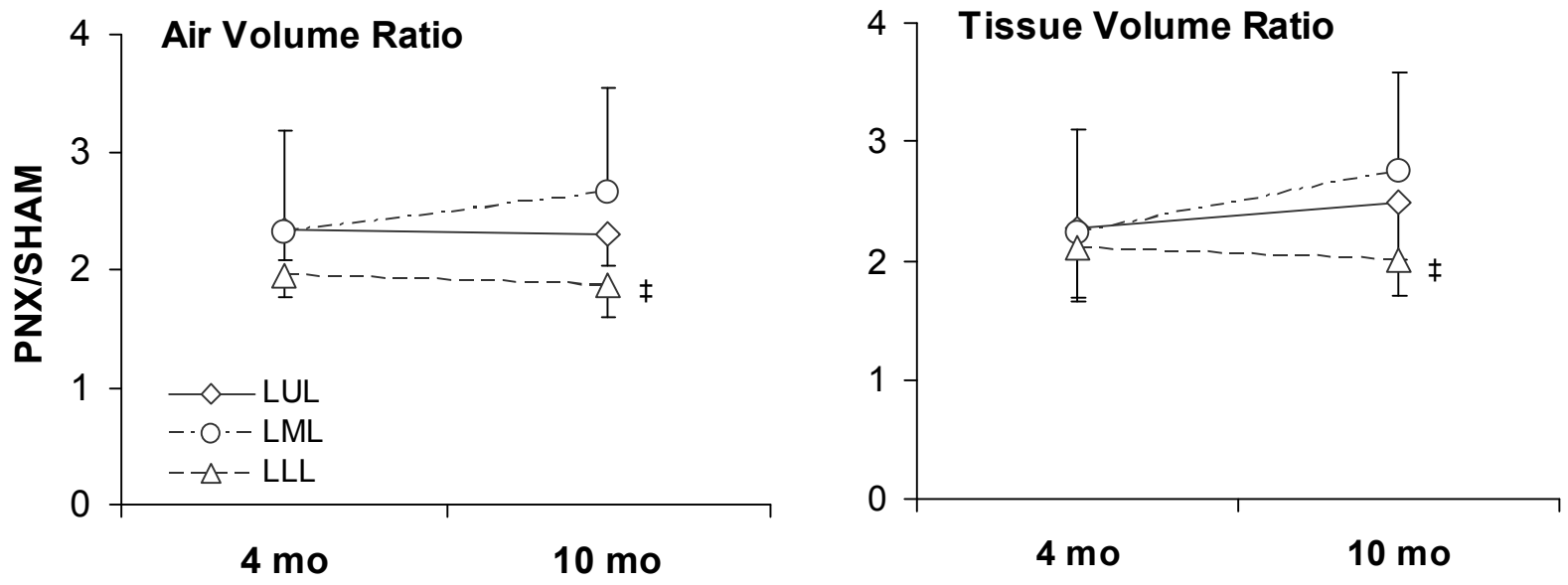

Fig. 5.4 Relative change in lobar air and tissue volume of the remaining left lung following right PNX expressed as a ratio to the mean value in corresponding lobes of SHAM control animals at 4 and 10 months after surgery (6 and 12 mo of age). Mean ± SD. All the ratios are significantly >1.0. At 10 months after PNX, the relative change in lung tissue and air volume of the remaining left lower lobe lagged significantly. ‡ $P \leq 0.05$ vs. left middle lobe by ANOVA.

Lobar tissue volume fraction (ratio of tissue volume to total volume) was significantly higher in the lower lobe than the upper or middle lobe in both experimental groups and both time points (Fig. 5.3). In both groups the ratio of tissue volume fractions at the two time points (4 mo/10 mo) increased similarly in all lobes, i.e., air volume fraction increased and tissue volume fraction declined as the animal matured (Fig. 5.3). As a result, the longitudinal change in overall tissue volume fraction of the whole left lung was similar between groups.

The relative compensatory changes in air and tissue volume of the remaining lobes after PNX was expressed as ratios to the mean value of the corresponding control lobe in sham-operated animals (Fig. 5.4). At 4 mo post-PNX, air and tissue volumes increased to a similar extent (2.0- to 2.3-fold) among all remaining lobes, that is, no significant regional differences in compensatory growth. By 10 mo after PNX, the relative volume increase in the left lower lobe (2.0- fold) had significantly lagged behind those in the upper and middle lobes (2.5- and 2.8- fold), indicating nonuniform rates of lobar compensatory growth.

Table 5- 2 Relative post-PNX compensation assessed by HRCT before or after somatic maturity.

Age at PNX (mo)	Time after surgery at HRCT (mo)	Air volume ratio PNX/SHAM *			Tissue volume ratio PNX/SHAM *		
		LUL	LML	LLL	LUL	LML	LLL
2.5	4	2.3 ± 0.3	2.3 ± 0.9	2.0 ± 0.2	2.3 ± 0.6	2.2 ± 0.9	2.1 ± 0.4
2.5	10	2.3 ± 0.3	2.7 ± 0.9	1.9 ± 0.3 ‡	2.5 ± 0.5	2.8 ± 0.8	2.0 ± 0.3 ‡
>12 #	12	2.3 ± 0.3	2.7 ± 0.8	1.9 ± 0.2 ‡	2.5 ± 0.5	2.8 ± 0.7	2.0 ± 0.3 ‡

* Average ratio (mean±SD) of value in PNX group to the mean value in corresponding SHAM group. CT tissue volume includes volume of air-free tissue and blood within acinar structures <1mm in diameter.

Data are taken from Ravikumar et al (78).

‡ $p \leq 0.05$ vs. corresponding LML by ANOVA.

5.4 Discussion

This is the first longitudinal examination of possible interactions between developmental and post- PNX signals on regional lung growth. In young dogs, growth rates among lobes were similar during maturation between 6.5 and 12.5 months of age. Air volume increased faster than tissue volume in all regions, so that tissue volume fraction, which was normally higher in the lower lobe than in upper and middle lobes, declined similarly among lobes during this interval. In actively growing animals 4 months after right PNX, lung tissue volume was higher to a similar extent (2.1- to 2.3-fold) in the remaining lobes relative to that in corresponding lobes of control animals. After reaching somatic maturity, i.e., 10 months post-PNX, the relative compensatory increase in tissue volume of the remaining left lower lobe (2.0- fold) lagged behind that of the upper and middle lobes (2.5- and 2.8- fold, respectively). Therefore, non-uniform regional parenchymal growth was absent 4 mo post-PNX but developed subsequently. At maturity (10 months post-PNX) the pattern of interlobar non-uniformity was similar to that previously reported in pneumonectomized adult dogs (78).

5.4.1 Normal Lung Development

Mechanical signals are believed to stimulate and sustain developmental as well as post-PNX lung growth (76 and 98). During maturation, the enlarging thorax, mediastinal structures, and lungs create opposing mechanical forces on lung tissue resulting in tissue strain and feedback interactions that sustain a balanced rate of cell growth among these components (34). The caudal lung region has higher vascular and interstitial conductance (3), larger capillary size and volume (24), and smaller air spaces (25) compared with

other regions and may explain its higher tissue volume fraction. In addition to expansion of air spaces and generation of new gas exchange units, the growing lung undergoes progressive remodeling with parenchymal involution, thinning of the blood-gas diffusion barrier, and increase in alveolar surfaces (18). The double alveolar-capillary morphology with its abundant septal interstitial cells and connective tissue of the immature lung is gradually replaced by the adult morphology of single capillary profiles and pruned interstitium (102). The longitudinal decline in tissue volume fraction assessed by HRCT in control animals is consistent with the sequence of parenchymal remodeling that continues for months after birth; the rate of decline was similar among lobes and unaffected by prior lung resection. Thus HRCT accurately tracks the anatomical consequences and spatial distribution of lobar expansion as well as parenchymal growth.

5.4.2 Post - PNX Compensatory Response

After PNX, the remaining lung becomes expanded and distorted. After stabilization of the initial increase in blood flow to the remaining lobes, we observed proportional changes in lobar air and tissue volumes by HRCT between 4 and 10 months post-PNX consistent with parenchymal growth. The present results extend our earlier observations using conventional thoracic CT in foxhounds raised to maturity after undergoing right PNX as puppies, where compensatory increases in lung volume were greatest in the mid-lung zones (88). In addition, the distribution of compensatory increase in air and tissue volumes at maturity in the present study is almost identical to that previously reported by us in dogs pneumonectomized as adults and studied by HRCT 12 months later (78), i.e., compensatory expansion and tissue growth was greater in the upper and middle lobes than in the lower lobe (Table 5-2).

In previous animals pneumonectomized as puppies and then raised to maturity, alveolar septal volume (blood plus tissue) measured by morphometry in the remaining lobes increased to ~2.6- to 2.9-fold of control value, associated with a corresponding increase in lung diffusing capacity; the latter was estimated by both morphometric and physiologic methods (85). In the present animals the in vivo increases estimated by HRCT ranged from 2.1- to 2.8-fold. In animals pneumonectomized as adults the corresponding compensatory volume increase assessed by morphometry and a physiological method was more modest, ~1.8-fold of control values (38 and 39). In both young and adult dogs, the fold change in alveolar septal tissue volume post-PNX obtained by morphometry was higher in the remaining left upper lung zone (upper and middle lobes combined) than in the left lower lobe (38 and 85), similar to the present findings by HRCT. In separate studies where we minimized lung expansion in post-PNX adult dogs using custom-shaped inflated silicone prosthesis to replace the right lung (98), compensatory lung expansion was also reduced to a greater extent in the mid- and lower lung zone, suggesting that this region is very sensitive to changes in intrathoracic mechanical signals.

One likely explanation for the relatively restricted compensatory response in the lower lobe post-PNX is the presence of the heart and elevated right hemidiaphragm, which offered asymmetric resistance to the expansion of the adjacent lower lobe. The heart causes greater distortion to the left than the right lung. In anesthetized dogs, weight of the heart in the left lateral decubitus position imposed a greater reduction in volume of the left lung than the corresponding reduction in volume of the right lung imposed by the right lateral decubitus position (9). In addition, the right hemidiaphragm becomes

elevated, stretched, and hypertrophied after right PNX (40), which increases the tension and decreases the compliance of the left hemidiaphragm, further impeding post-PNX expansion of the left lower lobe. Because the mediastinal ligaments are relatively thin in the dog, the lower lobe was still able to grow across the midline posterior to the heart, esophagus, and large vessels, leading to its irregular-shaped projection after PNX. Peripheral airways and blood vessels in the remaining lower lobe sometimes assume a direction 90° to 180° from the main stem bronchus and vessel. Such marked anatomical distortion raises important functional issues regarding effective distribution of ventilation and perfusion to the lower lobe as well as the contribution of regional anatomical distortion to the exponential increase in work of breathing observed during exercise post-PNX (43 and 86). We did not detect significant abnormalities in global ventilation-perfusion distributions after PNX at rest or during exercise using the multiple inert gas elimination technique (41 and 42) but have not examined regional ventilation perfusion distributions. Additional studies using functional imaging techniques will be helpful in mapping the regional correspondence between anatomical distortion and ventilation perfusion relationships.

5.4.3 Conclusion

In summary, we report that in actively growing animals, nonuniform distribution of lobar compensatory growth develops slowly between 4 and 10 months post-PNX, with the remaining left lower lobe growing at a significantly slower rate compared with the upper and middle lobes. At maturity, the pattern of lobar nonuniformity was not significantly different from that seen in animals undergoing PNX as adults. Combined with our previous report in these animals that dilatation of conducting airways also

developed slowly between 4 and 10 months after PNX (15), these results show that progressive interactions between developmental and post-PNX signals alter some aspects of lung and airway growth and remodeling, such as enhancing the magnitude of compensatory alveolar growth and exaggerating airway-parenchymal dissociation in dysanaptic growth; however, superimposing these independent signals does not alter the pattern of non uniform regional parenchymal growth.

Chapter 6 Correlation of lung growth assessed by computed tomography to that by morphometry

6.1 Introduction

Although significant effort has been made over the past decades to develop innovative CT image processing algorithms and to improve existing methods in terms of precision, reproducibility and computational efficiency, relatively little research has been undertaken to find out the validity of results obtained by these methods. My dissertation aims to bridge this gap by validating the CT derived air and tissue volumes against the existing gold standard of lung tissue volume measurement that by stereology applied on histological sections.

We used HRCT scans to assess lobar growth and expansion in 20 foxhounds. These foxhounds were subjected to either 42% (Left PNX) or 58% (Right PNX) lung resection. I chose to use animals from various cohorts subjected to either type of lung resection to validate the method across various compensatory models. Regional growth and expansion was compared against quantitative histology in animals wherein measurements by both methods were available (n=20). This comparison will be done in two steps. 1) Correlation between total air and tissue volumes measured by HRCT and morphometry methods will be analyzed. 2) Utility of HRCT in detecting regional changes of lung expansion and growth will be scrutinized. The advantages, limitations and various sources of error of both methods are discussed towards the end of this chapter.

6.2 Results

CT-derived total, tissue and air volumes were compared against the total, alveolar septal volume (tissue +capillary blood) and air volumes estimated by morphometric methods in postmortem fixed lungs. Figure 6-1 illustrates correlations between these two independent estimations for post-PNX compensation (left and right PNX together) in 20 animals in which measurements by both methods were available. These two estimates are significantly correlated in post-PNX dog lungs with a coefficient of determination (r-squared; it is the square of the correlation coefficient) of 0.89 and 0.78 and a slope of 1.46 and 1.21 for air volume and tissue volume respectively.

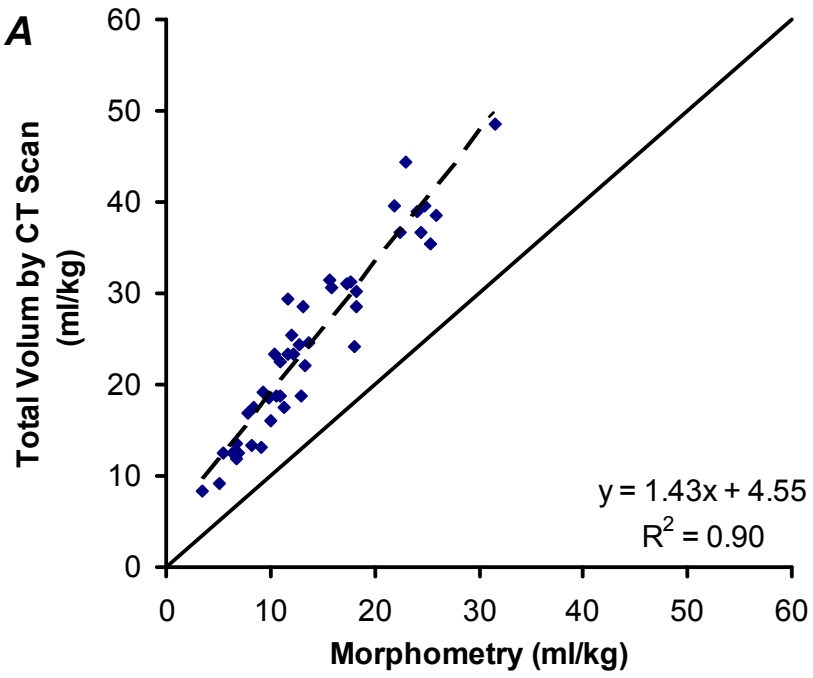

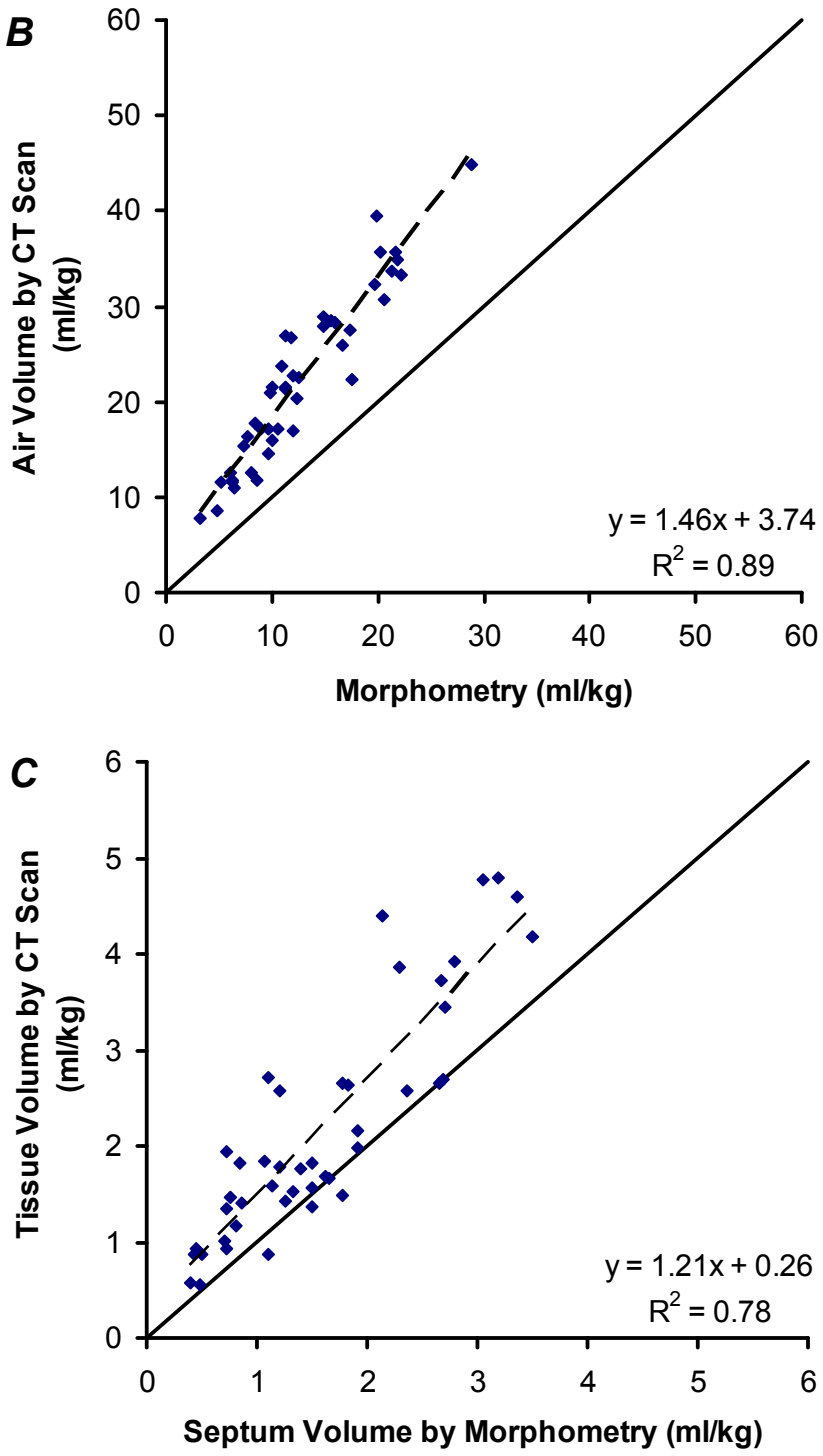

Figure 6.1 Correlation of lung volumes measured in vivo by CT scan at 20 cmH2O transpulmonary pressure and at postmortem by morphometry after tracheal instillation of fixatives at 25 cmH2O airway pressure in 20 animals in which both measurements are available. Fixed lungs were sectioned serially, and the total volume and alveolar septal volumes were estimated by point counting; differences between these two volumes were taken as air volume. Each data point represents volume of either a lobe or a stratum: upper stratum includes upper and

middle lobes; lower stratum includes the left lower lobe alone. *A*: total volume. *B*: air volume. *C*: tissue volume (by CT scan) and volume of alveolar septum (by morphometry). Solid line: identity, Dashed line: regression through data range.

The fixed lung after left PNX (42 % resection, n=11) was separated into upper and lower strata. The upper stratum consisted of the upper and middle lobes, while the lower stratum consisted of the lower and cardiac lobes of the right lung. The relative compensatory changes in air and tissue volume for each of the remaining stratums were expressed as a ratio to the mean value of the corresponding stratum in control animals. Since these studies were performed over a period of five years, the controls used for normalizing the HRCT and the morphometry data belonged to separate cohorts (n=7 for HRCT and n=6 for morphometry). Compensatory changes assessed by HRCT and morphometric methods for the left-PNX group are shown in Figure 6-2 and Table 6-1. Air and tissue volume estimates by both methods were similar, that is, no significant differences between methods.

The fixed lung after right PNX (58% resection, n=9) was divided into upper and lower strata. The upper stratum consisted of the upper and middle lobes, which were often incompletely separated. The lower stratum consisted of the just the lower lobe in the left lung. The relative compensatory changes in air and tissue volume of the remaining stratums were expressed as a ratio to the mean value of the corresponding stratum in control animals. The control animals were the same as the ones used for normalizing the left PNX data. Figure 6-3 and Table 6-2 show the compensatory changes assessed by HRCT and morphometric methods for the right PNX group. There were no significant differences in air and tissue volume estimates by both methods.

Table 6-1 Comparison of compensation after left-PNX by HRCT and Morphometry

Lung	HRCT	Morphometry
Number	11	11
Tissue volume ratio (PNX/Control)		
Upper Stratum	0.99 ± 0.22	0.98 ± 0.25
Lower Stratum	1.18 ± 0.24	1.23 ± 0.43
Total R Lung	1.10 ± 0.21	1.11 ± 0.32
Air volume ratio (PNX/Control)		
Upper Stratum	1.32 ± 0.15 *	1.34 ± 0.22 *
Lower Stratum	1.74 ± 0.14 *	1.68 ± 0.22 *
Total R Lung	1.52 ± 0.12 *	1.52 ± 0.12 *

Mean±SD, $p \leq 0.05$; * vs. Control by ANOVA.

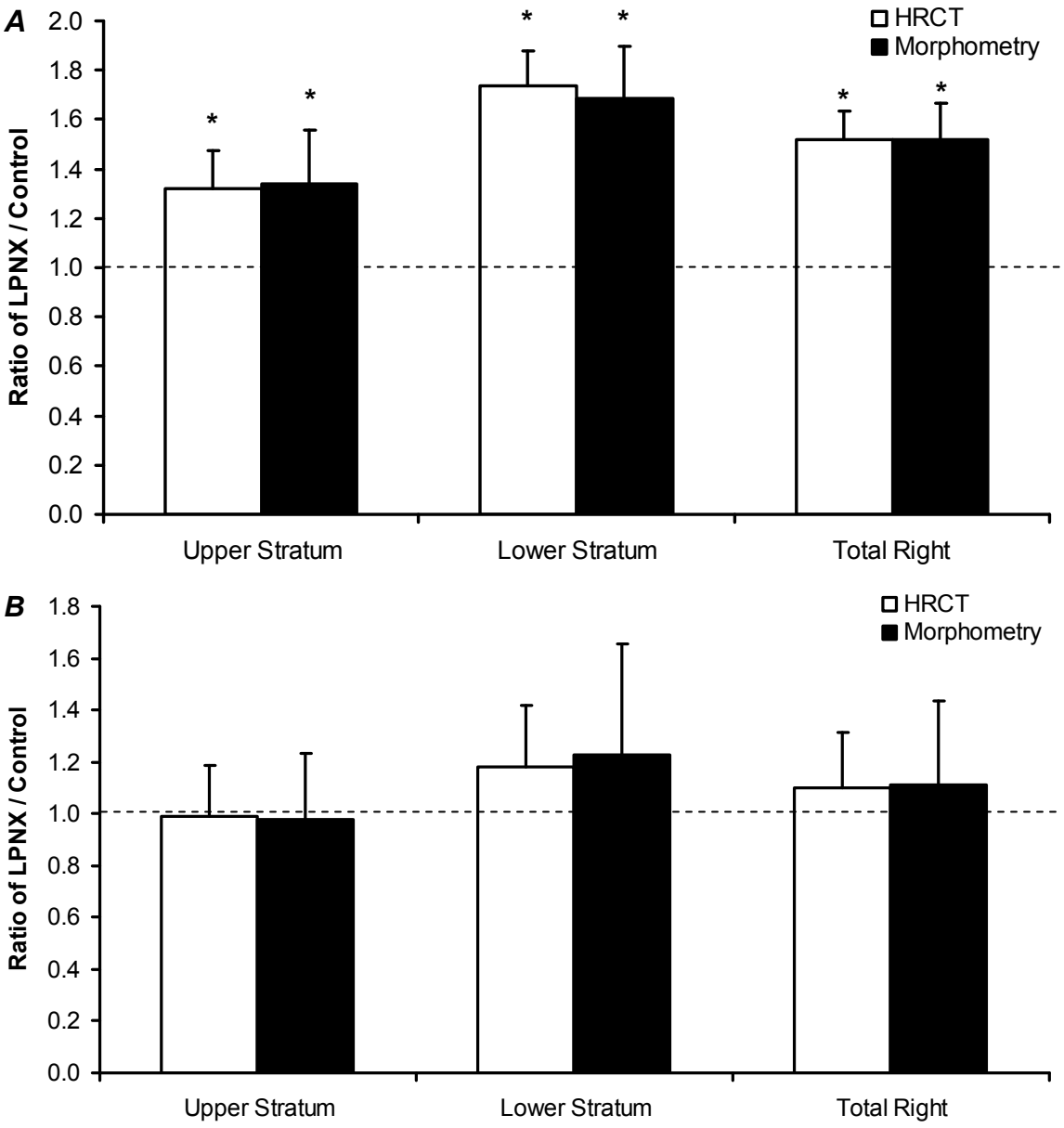

Figure 6.2 Relative change in lobar air volume (*A*) and tissue volume (*B*) in the remaining right lung after left PNX expressed as a fraction of the mean value in corresponding stratum of the control animals. Open bars refers to volume assessed by HRCT, solid bars refers to volume assessed by morphometry. Values are means ± SD. **P* ≤ 0.05 vs. 1.0 (dashed line, corresponding lobe in controls). There were no significant differences in air and tissue volume estimates by both methods.

Table 6-2 Relative compensation after right PNX assessed by HRCT and morphometry

	Air volume ratio PNX/Control			Tissue volume ratio PNX/Control		
	Left Upper stratum	Left Lower stratum	Total L lung	Left Upper stratum	Left Lower stratum	Total L lung
HRCT	2.68 ± 0.71 *	1.93 ± 0.26 *	2.06 ± 0.24 *	2.31 ± 0.39 *	2.02 ± 0.30 *	2.15 ± 0.32 *
Morphometry	2.89 ± 0.83 *	2.19 ± 0.38 *	2.12 ± 0.54 *	2.37 ± 0.25 *	2.32 ± 0.73 *	1.93 ± 0.89 *

Mean±SD, $p \leq 0.05$; * vs. Control by ANOVA.

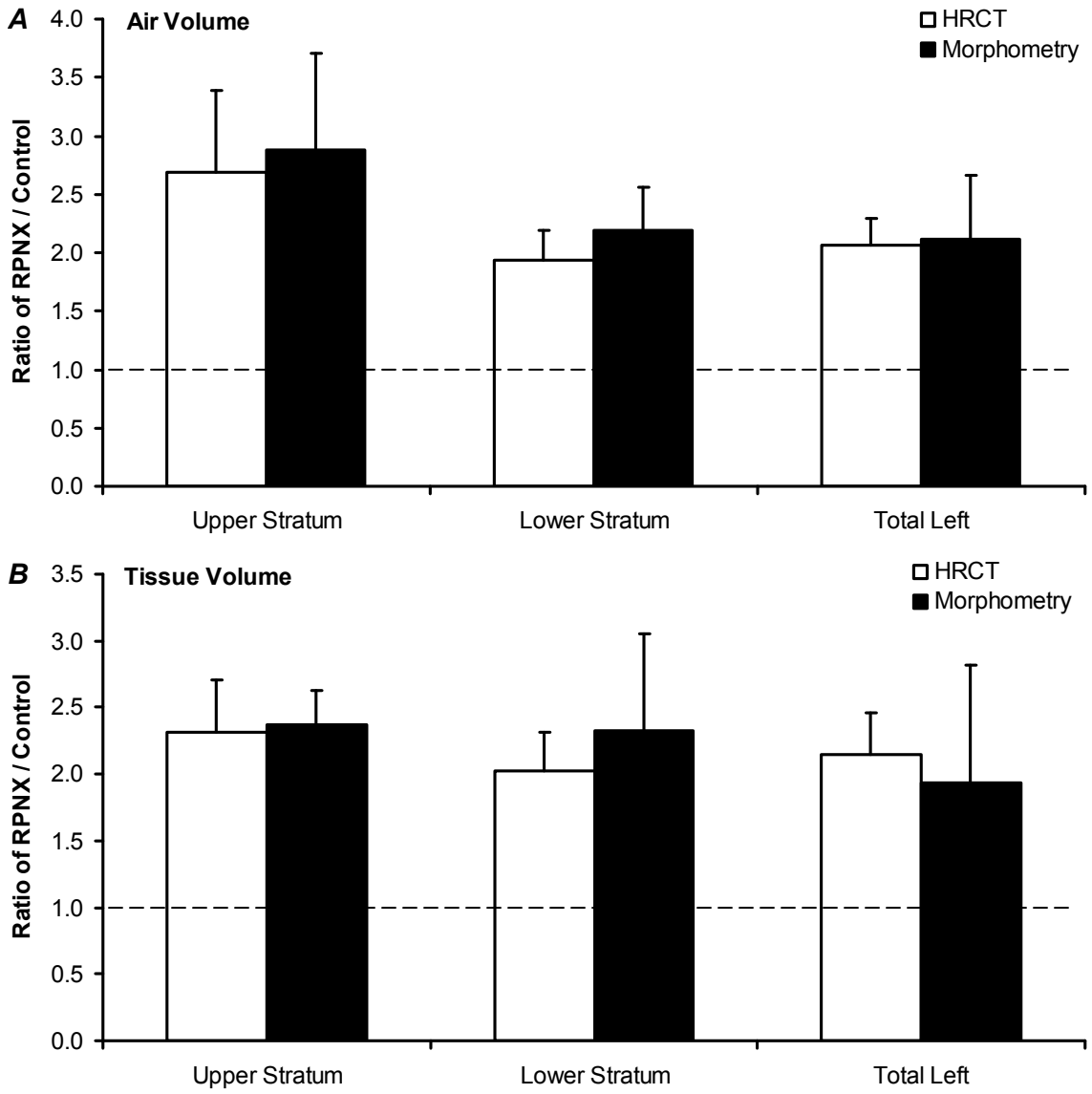

Figure 6.3 Relative change in lobar air volume (*A*) and tissue volume (*B*) in the remaining left lung after right PNX expressed as a fraction of the mean value in corresponding stratum of the control animals. Open bars refers to volume assessed by HRCT, solid bars refers to volume assessed by morphometry. Values are means ± SD. Both the upper and lower stratums expanded significantly after PNX compared to the corresponding stratum in the controls (i.e. $P \leq 0.05$ vs. 1.0 (dashed line)). There was no significant difference in air and tissue volume estimates by both methods.

6.3 Discussion

6.3.1 Summary of Findings

Although in vivo lung volume obtained by CT scan is systematically larger than that measured postmortem after tracheal instillation of fixatives at 25 cmH_2O of hydrostatic pressure (Figure 6-1), strong correlations exists between these two independent estimations of total air and tissue volumes in 20 animals in which measurements by both methods are available. HRCT was also able to detect regional compensatory changes in air and tissue volumes after left and right PNX (Figures 6-2 and 6-3) and was a good indicator of overall growth such as after right PNX or the lack of lung growth after left PNX. These data taken together lend support to the use of CT scan to track parenchyma growth in vivo.

6.3.2 Critique of the Methods

HRCT was the imaging modality of choice because of its speed, widespread availability, high-resolution anatomic visualization, and unique ability to quantify regional air and tissue volumes; it is a particularly powerful tool for the non-invasive measurement of lung mechanics in experimental models. Although CT scan does not eliminate cardiogenic motion artifacts (79), such artifacts occur in all animals and do not alter systematic comparisons among groups. Compared to other imaging modalities such as Magnetic Resonance Imaging (MRI), HRCT has certain short comings like decreased soft tissue contrast, need for a contrast agent to assess blood flow and problems associated with ionizing radiation. But MRI poses problems of its own such as inferior spatial resolution, degradation of image with respiratory motion, and the necessity of

eliminating metallic objects from the imaging environment, making the method unsuitable for studies with metallic implants.

Density gradients from thoracic CT scan have been utilized to partition changes of lung air and tissue volumes (13) in the assessment of emphysema (14), idiopathic pulmonary fibrosis (12 and 27), growth of pulmonary nodules (99), and acute respiratory distress syndrome (70, 71, 72, and 83). In patients studied by CT just before surgery for small lung tumors, the proportion of tissue to air obtained with CT in the resected lobe was similar to that obtained by morphometry (13). This technique has been used to follow parenchymal growth in children (16 and 17). Changes in volume distribution between upper and lower lobes have been reported in patients with acute lung injury (71). However, few studies have utilized this method for assessing regional lung growth in vivo.

We previously utilized CT scan to assess regional lung volume in foxhounds that had undergone right PNX as puppies and subsequently been raised to adulthood (88). We had also utilized CT scan to study the effects of preventing post-PNX lateral lung expansion in adult dogs by using space occupying inflated silicone prosthesis to replace the resected lung (100). In the presence of an inflated prosthesis, post-PNX volume expansion is preferentially blunted in the mid lung region compared with animals with a deflated prosthesis. Our previous CT studies were done with an older generation scanner at a lower resolution and without volumetric imaging and hence could not reliably resolve lobar fissures; this technical limitation has been overcome in the present study.

In these animals, we did not obtain CT scan before surgery and hence did not have a good baseline to normalize the post PNX regional compensatory changes. We used CT Scans from a cohort of control animals (sham, that underwent right thoracotomy without lung resection) to assess regional compensatory changes after left and right PNX (chapters 4 and 5). Since these studies were performed over a period of five years, the controls used for normalizing the HRCT and the morphometry data belonged to separate cohorts (n=7 for HRCT and n=6 for morphometry). Although the conclusions did not change in spite of using different cohorts to normalize the HRCT and morphometry data, it reinforces the need for better baseline measurement; ideally each animal should be used as its own control.

In our morphometric analysis, we did not separately analyze each lobe. We fixed the lung by tracheal instillation of fixatives at a constant hydrostatic pressure (37 and 38). Each lung was then divided into upper and lower strata while the airway pressure was maintained. The upper stratum consisted of the upper and middle lobes. The lower stratum consisted of either the lower lobe alone (left lung) or lower and cardiac lobes (right lung). This division was employed because the upper and middle lobes are often incompletely separated; forced separation causes loss of airway pressure and hence variability in lung volume measurement by the saline immersion method (95). After left PNX because the upper and lower stratum each contained one lobe that expanded significantly and one that did not, grouping two lobes into one stratum may obscure interlobar differences in structural adaptation even though no overall compensatory alveolar growth was evident by either CT scan or morphometry. In adult dogs after right PNX, the remaining lobes expanded more uniformly and to a greater extent than after left

PNX; hence, grouping left upper and middle lobes into the upper stratum would not bias morphometric analysis.

Since tissue volume estimated by HRCT includes not just alveolar septa but also small blood vessels and airway tissue up to ~1–2 mm in diameter, i.e., the resolution limit of the scan, CT-derived tissue volume is systematically higher than alveolar septal volume (tissue+capillary blood) measured by morphometric methods in postmortem fixed lungs. The mean CT values we used for lung tissue + blood are relatively stable (average 56 HU, range 52–59 HU). Other investigators have assumed a lung CT value of 65 HU (13, 31, and 49). If we recalculate our measurements based on their CT values, the maximum change in estimated tissue and air volumes is 1.3%.

After resection of one lung, blood flow to the remaining lung increases immediately and then stabilizes. Although we could not partition the higher tissue volume in PNX animals into tissue or blood content, this limitation does not invalidate the use of HRCT for following longitudinal parenchymal changes post- PNX for several reasons. *1*) Septal tissue and capillary blood volume increase in equal proportions during post-PNX compensation (85). *2*) After the immediate post-PNX increase in blood flow stabilizes, subsequent increases in both tissue and blood volumes contribute equally to functional compensation, i.e., to an increased lung diffusing capacity that is attributable to about equal increases in membrane diffusing capacity and pulmonary capillary blood volume (85, 87 and 88). Thus HRCT allows longitudinal follow-up of functionally relevant changes in lung parenchyma, which includes both tissue and blood.

The limitation in accurately defining lung volumes by HRCT is also due to difficulties in defining the edges or boundaries of the tissue (thresholding) which may be blurred because of motion artifact and small density differences from adjacent tissue, or partial volume effect. To contain this, we inflated the lung to a transpulmonary pressure of 20cmH_2O, (equivalent to an inflation volume of about 45 ml/kg above FRC). This helps in discerning the boundaries correctly and hence reduce partial volume effect. Also by selecting an appropriate threshold as the cutoff (details of density thresholding are explained in section 3.6); we eliminated voxels at the lung edges, including intrapulmonary vascular regions that have erroneous air content values due to partial volume effect and we minimized the inclusion of reconstruction noise.

The difference between lung volumes measured by HRCT and morphometry can be partially attributed to differences in thoracic compliance at the time of lung inflation. We used an inflation volume that was known to yield 20cmH_2O transpulmonary pressure in each animal. All animals had their static transpulmonary pressure-lung volume relationship measured in duplicate on at least one, sometimes multiple occasions prior to CT scan. Pleural pressure was measured with a balloon tipped catheter inserted into the distal 1/3 of the esophagus; mouth pressure was simultaneously measured to obtain transpulmonary pressure. In spite of these precautions, the pressure does drop during a breath hold due to stress relaxation, but the volume does not change during the course of the scan.

Both stress and strain transduce mechanical signals for tissue growth and remodeling. Our study was not designed to separate stress from strain signals. Our data suggest that post-PNX strain and lung growth are correlated. After one lung is removed

and the chest wall closed, a negative intrathoracic pressure causes the remaining lung to expand immediately, i.e., imparting three-dimensional strain. Minimizing lateral expansion of the remaining lung using a space-occupying inflatable silicone prosthesis is associated with blunted post-PNX lung expansion and tissue growth estimated by CT and morphometry as well as lower diffusing capacities for CO and O2 (54, 43, and 98). However, post-PNX regional stress/strain has not been directly measured.

6.3.3 Limitations of Morphometric Analysis

Lung volume is a basic measurement used in the calculation of all other tissue compartment volumes and surface areas from microscopic estimations of volume and surface densities (96 and 97), it is essential that the sources of variability in this measurement be understood. Because, the volume of an inflated lung comprises of mostly air (~90%), the lung should be fixed in such a way as to preserve it at a physiologically relevant state of inflation and to resist distortion by further processing for microscopy.

Lung is fixed under a standardized positive airway pressure of 25 cmH_2O, which is maintained for several days to weeks until the tissue is stiffened. Then, the lung is cut into slices and tissue blocks; at this time, any positive distending pressure that could keep soft tissue parts under tension is eliminated and the septa assumes a relaxed shape. For morphometric analysis, the optimal measurement of lung volume should be one obtained as close to the sampling and embedding steps as possible. Volume measured after sectioning by the Cavalieri method wherein the lung is in a state of relaxation, free of residual tissue elasticity is therefore preferable to that measured by saline immersion.

However, we found that the volume measured by the Cavalieri method is systematically lower (~10 to 25%) than that of the intact fixed lung under positive pressure (101). The differences probably arise from residual elastic recoil that was not completely abolished by fixation as well as folding or crumpling of fixed alveolar septa. Other investigators have also reported shrinkage in the order of ~10 to 15% in isolated dog lung fixed by perfusion with glutaraldehyde (58, 62, and 68). The use of Cavalieri volume in subsequent calculations could partially explain the higher CT derived lung volume compared to morphometry.

In addition to the variability in lung volume measurement after fixation by the immersion method, shrinkage occurs during subsequent histological processing (57). To avoid problems associated with tissue shrinkage and the use of correction factors thereafter we embedded the tissue in plastic (glycol methacrylate) (23). However, differential shrinkage might still occur during the dehydration process for embedding (66 and 94). This might also explain the lower air and tissue volume estimates by morphometry compared to HRCT.

6.3.4 Conclusion

In spite of its limitations, HRCT proves to be a powerful non-invasive technique to track parenchyma growth *in vivo*. HRCT represents the actual physiological state of the animal, is an excellent indicator of global growth in different compensatory models and is sensitive enough to detect the regional changes of lung expansion and growth as well. Suggestions to overcome some of the limitations of this technique are discussed in chapter 7.

Chapter 7 Summary and Future Directions

7.1 Summary

The key concepts are summarized below:

- Spatial distribution of compensatory growth and expansion in the remaining lobes after PNX is non-uniform which reflect non-uniform regional distribution of mechanical lung strain stemming from constraints imposed by rigid mediastinal structures such as the heart, great vessels, and ligaments.
- Distinct patterns of lobar expansion and growth emerge after left and right PNX. Regional lung expansion in the remaining lobes after left PNX is non-uniform. Regional lung growth and expansion is greater in magnitude and more uniformly distributed after right than left PNX.
- The non-uniform spatial distribution of compensatory growth is exaggerated by the interaction of developmental and post-PNX signals of lung growth in actively growing animals.
- Strong correlations exist between estimates of regional air and tissue volumes by HRCT and by detailed quantitative histology under light and electron microscopy indicative of the fact that HRCT can be used to follow parenchymal growth *in vivo*.

The systematic quantitative analysis of regional density gradients used in this study has potentially powerful applications in the assessment of regional heterogeneity in growth, disease, injury as well as local response to treatment.

7.2 Future Directions

Although the methodology has been validated, there is still room for further improvements. The possible future directions are summarized in the following sections.

- The positions of the lobar fissures are of considerable importance for image based quantitative pulmonary structural and functional analysis, and the increasingly large size of volumetric CT images makes the development of an automatic or a semiautomatic lobe segmentation method desirable. A fuzzy reasoning system can be developed to automatically detect the fissures using an anatomic atlas. This system can be used to identify additional pulmonary structures such as airways and vessels, or to report image based measurements on a regional basis.
- Tissue volume estimated by HRCT includes both tissue and blood volume within the gas exchange region, it is systematically larger than septal tissue volume estimated in the fixed lung by morphometry. This limitation can be overcome by obtaining CT scans before and after injection of a contrast material and evaluating the volume of blood and extravascular tissue separately.
- The magnitude and distribution of lobar tissue growth can be related to direct measures of regional mechanical lung strain. For instance, the distribution of regional parenchymal strain can be assessed by measuring the displacement of the radiopaque markers percutaneously implanted throughout the lung.
- Regional mechanical strain can also be assessed by registering the 3D coordinates of airway branch points. Any 4 non-coplanar branch points within

the lobe defines a tetrahedron of parenchyma. Changes in tetrahedral volume and strain in response to various interventions can be calculated. This technique will also allow direct tissue sampling which in turn will demonstrate the correlation between regional mechanical strain assessed by HRCT and structural indices and molecular pathways of compensatory lung growth.

- Lobar CT density gradients can be analyzed along the medial to lateral, posterior to anterior and cephalad to caudal directions and this information could be used in the quantification of regional disease or postural differences in the lung.
- Future research will also relate the magnitude and distribution of lobar tissue growth, to alveolar cell proliferation, to acinar, airway and vascular remodeling, and to overall lung function in the whole animal.

REFERENCES

1 Alcorn D., Adamson T.M., Lambert T.F., Maloney J.E., Ritchie B.C., and Robinson P.M. (1977) Morphological effects of chronic tracheal ligation and drainage in the fetal lamb lung. J. Anat. 123 (Pt 3): 649-660.

2 Bardocz S., Tatar-Kiss S., and Kertai P. (1986) The effect of alpha-difluoromethylornithine on ornithine decarboxylase activity in compensatory growth of mouse lung. Acta. Biochim. Biophys. Hung. 21: 59–65.

3 Beck K.C., and Rehder K. (1986) Differences in regional vascular conductances in isolated dog lungs. J. Appl. Physiol. 61: 530–538.

4 Brody, J. S. (1975) Time course of and stimuli to compensatory growth of the lung after pneumonectomy. J. Clin. Invest. 56: 897-904.

5 Buhain, W. J., and Brody J. S. (1973) Compensatory growth of the lung following pneumonectomy. J. Appl. Physiol. 35: 898-902.

6 Burkitt H.G., Young B., and Heath J.W. (1993) The Respiratory System. In: Wheater's functional histology: A text and colour Atlas. 3rd ed. Churchill Livingstone. Ch. 12, 222.

7 Burri, P. H., and Sehovic. S. (1979) The adaptive response of the rat lung after bilobectomy. Am. Rev. Respir. Dis. 119: 769-777.

8 Burri, P. H., Pfrunder, H. B., and Berger, L. C. (1982) Reactive changes in pulmonary parenchyma after bilobectomy: a scanning electron microscopic investigation. Exp. Lung Res. 4: 11-28.

9 Chang H., Lai-Fook S.J., Domino K.B., Schimmel C., Hildebrandt J., Robertson H.T., Glenny R.W., and Hlastala M.P. (2002) Spatial distribution of ventilation and perfusion in anesthetized dogs in lateral postures. J. Appl. Physiol. 92: 745–762.

10 Chevalier P.A., Rodarte J.R., and Harris L.D. (1985) Regional lung expansion at total lung capacity in intact vs. excised canine lungs. J. Appl. Physiol., 58(1): 164–172.

11 Cohn R. (1939) Factors affecting the postnatal growth of the lung. Anat. Rec. 75:195–205.

12 Coxson H.O., Hogg J.C., Mayo J.R., Behzad H., Whittall K.P., Schwartz D.A., Hartley P.G., Galvin J.R., Wilson J.S., and Hunninghake G.W. (1997) Quantification of idiopathic pulmonary fibrosis using computed tomography and histology. Am. J. Respir. Crit. Care Med. 155: 1649-1656.

13 Coxson H.O., Mayo J.R., Behzad H., Moore B.J., Verburgt L.M., Staples C.A., Pare P.D., and Hogg J.C. (1995) Measurement of lung expansion with computed tomography and comparison with quantitative histology. J. Appl. Physiol. 79: 1525–1530.

14 Coxson H.O., Rogers R.M., Whittall K.P., D'Yachkova Y., Pare P.D., Sciurba F.C., and Hogg J.C. (1999) A quantification of the lung surface area in emphysema using computed tomography. Am. J. Respir. Crit. Care Med. 159: 851–856.

15 Dane D.M., Johnson R.L, Jr., and Hsia C.C.W. (2002) Dysanaptic growth of conducting airways after pneumonectomy assessed by CT scan. J. Appl. Physiol. 93: 1235-1242.

16 De Jong P.A., Long F.R., Wong J.C., Merkus P.J., Tiddens H.A., Hogg J.C., Coxson H.O. (2006) Computed tomographic estimation of lung dimensions throughout the growth period. Eur. Respir. J. 27: 261–267.

17 De Jong P.A., Nakano Y., Lequin M.H., Merkus P.J., Tiddens H.A., Hogg J.C., Coxson H.O. (2003) Estimation of lung growth using computed tomography. Eur. Respir. J. 22: 235–238.

18 De Paepe M.E., Sardesai M.P., Johnson B.D., Lesieur-Brooks A.M., Papadakis K., Luks F.I. (1999) The role of apoptosis in normal and accelerated lung development in fetal rabbits. J. Pediatr. Surg. 34: 861–870.

19 Evans H.E. (1993) The Respiratory System. In: Miller's Anatomy of the dog. 3rd Edition. W. B. Saunders Company/Philadelphia, ch. 8, 463-493

20 Feeney D.A., Fletcher T.F., and Hardy R.M. (1991) Thorax. In: Atlas of correlative imaging anatomy of the normal dog: ultrasound and computed tomography. W. B. Saunders Company/Philadelphia, Sec. 3, 153-217.

21 Fisher J.M., and Simnett J.D. (1973) Morphogenetic and proliferative changes in the regenerating lung of the rat. Anat. Rec. 176: 389–395.

22 Gehr P., Bachofen M., and Weibel E.R.. (1978). The normal human lung: ultrastructure and morphometric estimation of diffusion capacity. Respir. Physiol. 32: 121–140.

23 Gerrits P.O., and Horobin R.W. (1996) Glycol methacrylate embedding for light microscopy: basic principles and trouble-shooting. J. Histotechnol. 19, 297–311.

24 Glazier J.B., Hughes J.M, Maloney J.E., and West J.B. (1969) Measurements of capillary dimensions and blood volume in rapidly frozen lungs. J. Appl. Physiol. 26: 65–76.

25 Glazier J.B., Hughes J.M., Maloney J.E., and West J.B. (1967) Vertical gradient of alveolar size in lungs of dogs frozen intact. J. Appl. Physiol. 23: 694–705.

26 Harding R., and Hooper S.B. (1996) Regulation of lung expansion and lung growth before birth. J. Appl. Physiol. 81(1): 209-224.

27 Hartley P.G., Galvin J.R., Hunninghake G.W., Merchant J.A., Yagla S.J., Speakman S.B., and Schwartz D.A. (1994) High-resolution CT-derived measures of lung density are valid indexes of interstitial lung disease. J. Appl. Physiol.76: 271–277.

28 Hassler F. (1892) Ueber compensatorische hypertrophie der lunge. Virchows Arch. Pathol. Anat. Physiol. 128: 527–536.

29 Hoffman E.A. (1985) Effect of body orientation on regional lung expansion: a computed tomographic approach. J. Appl. Physiol. 59(2): 468-480.

30 Hoffman E.A., and McLennan G. (1997) Assessment of the pulmonary structure function relationship and clinical outcomes measures: Quantitative volumetric CT of the lung. Acad. Radiol. 4(11): 758–776.

31 Hoffman E.A., and Ritman E.L. (1985) Effect of body orientation on regional lung expansion in dog and sloth. J. Appl. Physiol. 59: 481–491.

32 Hooper S.B., and Harding R. (1995) Fetal lung liquid: a major determinant of the growth and functional development of the fetal lung. Clin. Exp. Pharmacol. Physiol. 22(4): 235-247.

33 Hsia C.C.W. (2004) Lessons from a canine model of compensatory lung growth. Curr. Top. Dev. Biol. 64: 17-32.

34 Hsia C.C.W. (2004) Signals and mechanisms of compensatory lung growth. J. Appl. Physiol. 97: 1992–1998.

35 Hsia C.C.W., and Johnson R.L. Jr. (2006). Further examination of alveolar septal adaptation to left pneumonectomy in the adult lung. Respir. Physiol. Neurobiol. 151(2-3): 167-177.

36 Hsia C.C.W., Carlin J.I., Ramanathan M., Cassidy S.S., and Johnson R.L. Jr. (1991) Estimation of diffusion limitation after pneumonectomy from carbon monoxide diffusing capacity. Respir. Physiol. 83: 11–21.

37 Hsia C.C.W., Fryder-Doffey F., Stalder-Navarro V., Johnson R.L. Jr., and Weibel E.R. (1993) Structural changes underlying compensatory increase of diffusing capacity after left pneumonectomy in adult dogs. J. Clin. Invest. 92: 758–764. [Corrigenda. J. Clin. Invest. (1994) 93: 913].

38 Hsia C.C.W., Herazo L.F., Fryder-Doffey F., and Weibel E.R. (1994) Compensatory lung growth occurs in adult dogs after right pneumonectomy. J. Clin. Invest. 94: 405–412.

39 Hsia C.C.W., Herazo L.F., Ramanathan M. and Johnson R.L. Jr. (1994) Cardiopulmonary adaptations to pneumonectomy in dogs. IV. Membrane diffusing capacity and capillary blood volume. J. Appl. Physiol. 77: 998–1005.

40 Hsia C.C.W., Herazo L.F., Ramanathan M., Claassen H., Fryder-Doffey F., Hoppeler H., and Johnson R.L. Jr. (1994) Cardiopulmonary adaptations to pneumonectomy in dogs. III Ventilatory power requirements and muscle structure. J. Appl. Physiol. 76: 2191–2198.

41 Hsia C.C.W., Herazo L.F., Ramanathan M., Johnson R.L. Jr., and Wagner P.D. (1993) Cardiopulmonary adaptations to pneumonectomy in dogs. II. Ventilation-perfusion relationships and microvascular recruitment. J. Appl. Physiol. 74: 1299–1309.

42 Hsia C.C.W., Johnson R.L. Jr., Wu E.Y., Estrera A.S., Wagner H., and Wagner P.D. (2003) Reducing lung strain after pneumonectomy impairs diffusing capacity but not ventilation-perfusion matching. J. Appl. Physiol. 95: 1370–1378.

43 Hsia C.C.W., Takeda S.I., Wu E.Y., Glenny R.W., and Johnson R.L. Jr. (2000) Adaptation of respiratory muscle perfusion during exercise to chronically elevated ventilatory work. J. Appl. Physiol. 89: 1725–1736.

44 Hsia C.C.W., Wu E.Y., Wagner E., and Weibel E.R. (2001) Preventing mediastinal shift after pneumonectomy impairs regenerative alveolar tissue growth. Am. J. Physiol. Lung Cell Mol. Physiol. 281(5): L1279- L1287.

45 http://www.phantomlab.com/pdf/catphan500-600manual.pdf

46 Hubmayr R., Walters B., Chevalier P., Rodarte J., and Olson L. (1983) Topographical distribution of regional lung volume in anesthetized dogs. J. Appl. Physiol., 54(4): 1048–1056.

47 Hubmayr R.D., and Margulies S.S. (1996) Regional ventilation in statically and dynamically hyperinflated dogs. J. Appl. Physiol., 81(4): 1815–1821.

48 Hubmayr R.D., Rodarte J.R., Walters B.J., and Tonelli F.M. (1987) Regional ventilation during spontaneous breathing and mechanical ventilation in dogs. J. Appl. Physiol., 63(6): 2467–2475.

49 Hyde R.W., Wandtke J.C., Fahey P.J., Utell M.J., Plewes D.B., and Goske M. (1989) Lung weight in vivo measured with computed tomography and rebreathing of soluble gases. J. Appl. Physiol. 67(1): 166-173.

50 Johnson R.L. Jr., Cassidy S.S., Grover R.F., Schutte J.E., and Epstein R.H. (1985) Functional capacities of lungs and thorax in beagles after prolonged residence at 3,100 m. J. Appl. Physiol. 59: 1773-1782.

51 Kalender W.A (2000) Principles of Computed tomography In: Computed tomography: Fundamentals, System technology, Image Quality, Applications Wiley-VCH, Munich Ch.1, 17-34.

52 Kallok M.J., Chevalier P.A., and Rodarte J.R. (1979) Analysis of parenchymal deformation in excised canine lung lobes using rotationally rotationally-corrected strains. J. Biomech., 12(10): 789–791.

53 Kallok M.J., Wilson T.A., Rodarte J.R., Fook S.J.L., Chevalier P.A., and Harris L.D. (1979) Distribution of regional volumes and ventilation in excised canine lobes. J. Appl. Physiol., 47(1): 182–191.

54 Kitagawa M., Hislop A., Boyden E.A., and Reid L. (1971) Lung hypoplasia in congenital diaphragmatic hernia. A quantitative study of airway, artery, and alveolar development. Br. J. Surg. 58(5): 342-346.

55 König M.F., Lucocq J.M., and Weibel, E.R. (1993) Demonstration of pulmonary vascular perfusion by electron and light microscopy. J. Appl. Physiol. 75: 1877–1883

56 Langston C., Sachdeva P., Cowan M.J., Haines J., Crystal R.G., and Thurlbeck W.M. (1977) Alveolar multiplication in the contralateral lung after unilateral pneumonectomy in the rabbit. Am. Rev. Respir. Dis. 115: 7–13.

57 Lum, H., and Mitzner W. (1985) Effects of 10% formalin fixation on fixed lung volume and lung tissue shrinkage. A comparison of eleven laboratory species. Am. Rev. Respir. Dis. 132: 1078-1083.

58 Mazzone R.W., Kornblau S., and Durand C.M. (1980) Shrinkage of lung after chemical fixation for analysis of pulmonary structure-function relations. J. Appl. Physiol. 48: 382-385.

59 McBride J.T. (1989) Lung volumes after an increase in lung distension in pneumonectomized ferrets. J. Appl. Physiol. 67: 1418–1421

60 Michel R.P., and Cruz-Orive L.M. (1988). Application of the Cavalieri principle and vertical sections method to lung: estimation of volume and pleural surface area. J. Microsc. 150: 117–136.

61 Müller A.E., Cruz-Orive L.M., Gehr P., and Weibel E.R. (1981) Comparison of two subsampling methods for electron microscopy morphometry. J. Microsc. 123(1): 35-49.

62 Murphy B.G., and Engel L.A. (1980) Shrinkage of dog lobes during air-drying fixation. J. Appl. Physiol. 49: 536-537.

63 Nardo L., Hooper S.B., and Harding R. (1998) Stimulation of lung growth by tracheal obstruction in fetal sheep: relation to luminal pressure and lung liquid volume. Pediatr. Res. 43(2): 184-190.

64 Nobuhara K.K., Fauza D.O., DiFiore J.W., Hines M.H., Fackler J.C., Slavin R., Hirschl R., and Wilson J.M. (1998). Continuous intrapulmonary distension with perfluorocarbon accelerates neonatal (but not adult) lung growth. J. Pediatr. Surg. 33(2): 292-298.

65 Oberg K.C., and Carpenter G. (1989) EGF-induced PGE2 release is synergistically enhanced in retinoic acid treated fetal rat lung cells. Biochem. Biophys. Res. Commun. 162: 1515-1521.

66 Ochs M. (2006) A brief update on lung stereology. J. Microsc. 222(3): 188-200.

67 Okada O., Presson, R.G. Jr., Kirk K.R., Godgey P.S., Capen R.L., and Wagner W.W. (1992) Capillary perfusion patterns in single alveolar walls. J. Appl. Physiol. 72: 1838-1844.

68 Oldmixon E.H., Suzuki S., Butler J.P., and Hoppin F.G., Jr. (1985) Perfusion dehydration fixes elastin and preserves lung air-space dimensions. J. Appl. Physiol. 58: 105-113.

69 Pao Y.C., Chevalier P.A., Rodarte J.R., and Harris L.D. (1978) Finite-element analysis of the strain variations in excised lobe of canine lung. J. Biomech. 11(3): 91–100.

70 Puybasset L., Cluzel P., Chao N., Slutsky A.S., Coriat P., and Rouby J.J. (1998) A computed tomography scan assessment of regional lung volume in acute lung injury. The CT Scan ARDS Study Group. Am. J. Respir. Crit. Care Med. 158: 1644–1655.

71 Puybasset L., Cluzel P., Gusman P., Grenier P., Preteux F., and Rouby J.J. (2000) Regional distribution of gas and tissue in acute respiratory distress syndrome. I. Consequences for lung morphology. The CT Scan ARDS Study Group. Intensive Care Med. 26: 85

72 Puybasset L., Gusman P., Muller J.C., Cluzel P., Coriat P., and Rouby J.J. (2000) Regional distribution of gas and tissue in acute respiratory distress syndrome. III. Consequences for the effects of positive end-expiratory pressure. The CT Scan ARDS Study Group Adult Respiratory Distress Syndrome. Intensive Care Med. 26: 1215–1227.

73 Rahn H., and Ross B.B. (1957) Bronchial tree casts, lobe weights and anatomical dead space measurements in the dog's lung. J. Appl. Physiol. 10: 154–157.

74 Rannels D. E., and Rannels S. R. (1997) Compensatory growth. In: Crystal R.G., West J.B., Barnes P.J., and Weibel E.R., editors. The lung: scientific foundations, 2nd ed. Philadelphia: Lippincott-Raven. 1035–1046.

75 Rannels D. E., White D. M., and Watkins C. A. (1979) Rapidity of compensatory lung growth following pneumonectomy in adult rats. J. Appl. Physiol. 46: 326-333.

76 Rannels D.E. (1989) Role of physical forces in compensatory growth of the lung. Am. J. Physiol. Lung Cell Mol. Physiol. 257: L179-L189.

77 Ravikumar P., Yilmaz C., Dane D.M., Hsia C.C.W., Hurst M.D., Fehmel J.L., Thorson C.L. and Johnson, R.L. Jr. (2006) Delayed Imposition of Mechanical Lung Strain Improves Adaptive Response Following Pneumonectomy, Proc. Am. Thorac. Soc. 3: A873.

78 Ravikumar P., Yilmaz C., Dane D.M., Johnson R.L. Jr., Estrera A.S., and Hsia C.C. (2004) Regional lung growth following pneumonectomy assessed by computed tomography. J. Appl. Physiol. 97: 1567–1574 (discussion 1549).

79 Reinhardt J.M., and Hoffman E.A. (1998) Quantitative pulmonary imaging: Spatial and temporal considerations in high-resolution CT. Acad. Radiol. 5: 539–546.

80 Rodarte J.R., Chaniotakis M., and Wilson T.A. (1989) Variability of parenchymal expansion measured by computed tomography. J. Appl. Physiol., 67(1): 226–231.

81 Rodarte J.R., Hubmayr R.D., Stamenovic D., and Walters B.J. (1985) Regional lung strain in dogs during deflation from total lung capacity. J. Appl. Physiol., 58(1): 164–172.

82 Romanova, L. K. (1960) Regenerative hypertrophy of the lungs in rats after one-stage removal of the entire left lung and the diaphragmatic lobe of the right lung. Bull. Exp. Biol. Med. 50: 100-105.

83 Rouby J.J., Puybasset L., Cluzel P., Richecoeur J., Lu Q. and Grenier P. (2000) Regional distribution of gas and tissue in acute respiratory distress syndrome. II. Physiological correlations and definition of an ARDS Severity Score. CT Scan ARDS Study Group. Intensive Care Med. 26: 1046–1056.

84 Sekhon H.S., and Thurlbeck W.M. (1992) A comparative study of post-pneumonectomy compensatory lung response in growing male and female rats. J. Appl. Physiol. 73: 446-451.

85 Takeda S., Hsia C.C.W., Wagner E., Ramanathan M., Estrera A.S., and Weibel E.R. (1999) Compensatory alveolar growth normalizes gas exchange function in immature dogs after pneumonectomy. J. Appl. Physiol. 86: 1301–1310.

86 Takeda S., Ramanathan M., Estrera A.S., and Hsia C.C.W. (1999). Post-pneumonectomy alveolar growth does not normalize hemodynamic and mechanical function. J. Appl. Physiol. 87: 491-497.

87 Takeda S., Ramanathan M., Wu E.Y., Estrera A.S., Hsia C.C.W. (1996) Temporal course of gas exchange and mechanical compensation after right pneumonectomy in immature dogs. J. Appl. Physiol. 80: 1304–1312. [Published corrigenda in J. Appl. Physiol. 80: 1996].

88 Takeda S., Wu E.Y., Epstein R.H., Estrera A.S., and Hsia C.C.W. (1997) In vivo assessment of changes in air and tissue volumes after pneumonectomy. J. Appl. Physiol. 82: 1340-1348.

89 Thibeault D.W., and Haney B. (1998) Lung volume, pulmonary vasculature, and factors affecting survival in congenital diaphragmatic hernia. Pediatrics 101: 289–295.

90 Thurlbeck W.M., Galaugher W., and Mathers J. (1981) Adaptive response to pneumonectomy in puppies. Thorax. 36: 424–427.

91 Valls-i-Soler A., Alfonso L.F., Arnaiz A., Alvarez F.J., and Tovar J.A. (1996) Pulmonary surfactant dysfunction in congenital diaphragmatic hernia: experimental and clinical findings. Biol. Neonate. 69(5): 318-326.

92 Vandenburgh H.H. (1992) Mechanical forces and their second messengers in stimulating cell growth in vitro. Am. J. Physiol. 262(3 Pt 2): R350-R355.

93 Wandtke J.C., Hyde R.W., Fahey P.J., Utell M.J., Plewes D.B., Goske M.J., and Fischer H.W. (1986) Measurement of lung gas volume and regional density by computed tomography in dogs. Invest. Radiol. 21: 108-117.

94 Weibel E.R. (1963). Material and methods of preparation for morphometric studies of the lung In: Morphometry of the Human Lung. Springer-Verlag/Academic Press Inc., Berlin, ch. 4, 40-50.

95 Weibel E.R., Kistler G.S., and Scherle W.F. (1966) Practical stereological methods for morphometric cytology. J. Cell Biol. 30: 23–38.

96 Weibel, E. R. (1984) Morphometric and stereological methods in respiratory physiology, including fixation techniques. In: Techniques in the Life Sciences. Respiratory Physiology, edited by A. B. Otis. County Clare, Ireland/Elsevier, vol. P401, 1-35.

97 Weibel, E.R, and Cruz-Orive L.M. (1997) Morphometric methods. In: The Lung: Scientific Foundations (2nd ed.), edited by Crystal R.G., West J.B., Weibel E.R., and Barnes P.J. Philadelphia, PA/Lippincott-Raven, 333-344.

98 Wirtz H.R., and Dobbs L.G. (2000) The effects of mechanical forces on lung functions. Respir. Physiol .119: 1–17.

99 Wormanns D., Kohl G., Klotz E., Marheine A., Beyer F., Heindel W., and Diederich S. (2004) Volumetric measurements of pulmonary nodules at multi-row detector CT: in vivo reproducibility. Eur. Radiol. 14: 86 –92.

100 Wu E.Y., Hsia C.C.W., Estrera A.S., Epstein R.H., Ramanathan M., and Johnson R.L. Jr. (2000) Preventing mediastinal shift after pneumonectomy does not abolish physiological compensation. J. Appl. Physiol. 89(1):182-191.

101 Yan X., Polo Carbayo J.J., Weibel E.R., and Hsia C.C.W. (2003) Variation of lung volume after fixation when measured by immersion or Cavalieri method. Am. J. Physiol. Lung Cell Mol. Physiol. 284: L242–L245.

102 Zeltner T.B., and Burri P.H. (1987) The postnatal development and growth of the human lung. II. Morphology respiration. Physiology. 67: 269 –282.

103 Zhang S., Garbutt V., and McBride J.T. (1996) Strain-induced growth of the immature lung. J. Appl. Physiol. 81: 1471–1476.